Optical plane selection in a dipole trap

Dissertation
zur
Erlangung des Doktorgrades (Dr. rer. nat.)
der
Mathematisch-Naturwissenschaftlichen Fakultät
der
Rheinischen Friedrich-Wilhelms-Universität Bonn

vorgelegt von
Falk-Richard Gerhard Heinz Winkelmann
aus
Soltau, Deutschland

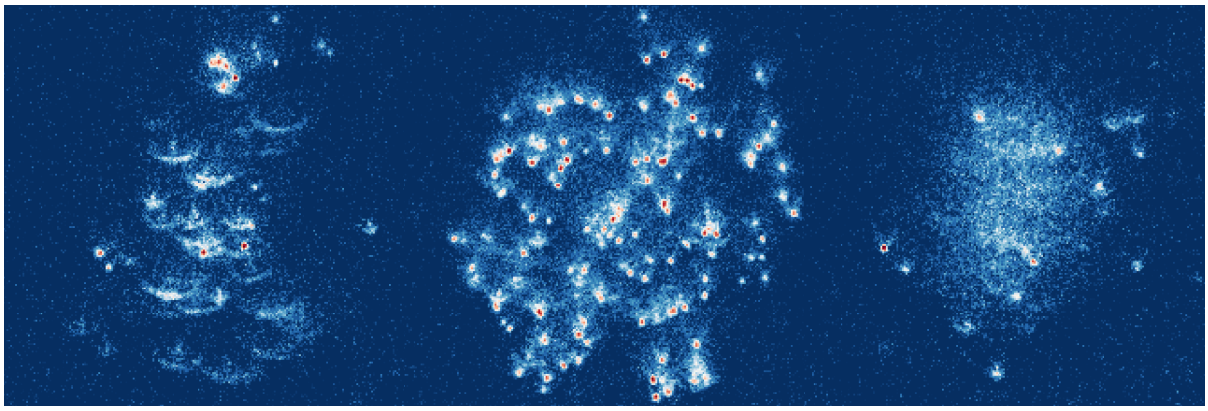

Bonn, 30.09.2021

Angefertigt mit Genehmigung der Mathematisch-Naturwissenschaftlichen Fakultät der Rheinischen Friedrich-Wilhelms-Universität Bonn

1. Gutachter:	Prof. Dr. Dieter Meschede
2. Gutachter:	Prof. Dr. Sebastian Hofferberth
Tag der Promotion:	06.12.2021
Erscheinungsjahr:	2021

Für meine Eltern und für Sandra

Abstract

Quantum technology has advanced considerably within the last decades [1, 2]. Quantum simulators are among the primary goals of this ongoing „quantum revolution“ [3]. They promise insight into many-particle phenomena that are too complex to study on classical machines [4].
In this thesis, I present my contribution to the discrete-time quantum walk simulator (DQSIM) experiment. We trap neutral cesium atom in a two dimensional state-dependent optical lattice [5], with the goal of realizing two-dimensional discrete-time quantum walks [6] and multi-particle entanglement [7].
The atoms are imaged using a high numerical objective lens [8] that allows us to resolve the spatial distribution inside the lattice. An additional retro-reflected beam provides state-independent confinement along the imaging axis. To measure multi-particle interference, we have to confine the atomic ensemble to a single layer along the imaging axis. I propose a novel way of plane selection with neutral cesium atoms in an optical dipole trap utilizing artificial magnetic fields created by a gradient of polarization. The preparation of thin volumes is demonstrated. With further careful adjustment of the experimental parameters, this technique will enable the selection of single planes.
We have to apply a magnetic guiding field to enable state-dependent transport of atoms. I designed a current stealing circuit to enable the long coherence times required for quantum simulations. The magnetic guiding field is stabilized to the level of 1 ppm. We measure a coherence time in free fall of T_2 =1.7 (1.4|2.1) ms. Vertical magnetic field gradients appear to be the limiting factor. With plane selection, coherence times of several tens of ms appear possible. This will allow for quantum walks with several hundred steps. The state-dependent potential of the DQSIM experiment can also be used to reconstruct the vibrational state of neutral atoms. I numerically investigate a novel scheme to probe the Wigner function by directly measuring the expectation value of the displaced parity operator.
Measuring the parity operator requires us to tune the lattice depth dynamically. Displacing the atoms purely in position space without transferring momentum requires fast modulation of the lattice position. I demonstrate that we can use the processing capabilities of our digital intensity and phase control to achieve this. Stable operation over a large dynamical range is realized by linearizing the system response. Feed-forward control of the lattice position in conjunction with internal model control increases the modulation bandwidth from 230 kHz to 3.3 MHz.
Precise control over the vibrational degree of freedom is a prerequisite to preparing arbitrary states of motion, such as Fock states. I demonstrate Raman sideband cooling along the vertical direction using the D1 transition of cesium. This complements the microwave mediated sideband cooling that we use to cool horizontally.
Finally, I discuss possible future experiments such as the release-retrap technique to enhance the filling factor in the center of the trap [9, 10], magnetic quantum walks [11], and direct measurement of the exchange phase of indistinguishable particles [12].

Contents

1 Introduction **1**

2 Experimental Apparatus **3**
2.1 Overview . . . 3
2.1.1 Experimental sequence . . . 4
2.1.2 The vacuum apparatus . . . 4
2.1.3 Collecting and preparing atoms . . . 5
2.2 Current stabilization at the 1ppm level . . . 8
2.2.1 Measuring magnetic fields using Ramsey interferometry . . . 9
2.2.2 Concept of stealing . . . 11
2.2.3 Characterizing the performance . . . 13
2.2.4 Discussion and conclusion . . . 16
2.3 Laser configuration and the optical dipole potential . . . 16
2.3.1 A three dimensional dipole trap . . . 18
2.3.2 Laser system . . . 19
2.4 Digital intensity control at the shot noise level . . . 20
2.4.1 Polarization synthesizer . . . 21
2.4.2 Digital intensity control at the shot noise level . . . 22
2.4.3 Linearization of system response and feed forward control . . . 24
2.4.4 Summary and Outlook . . . 25
2.5 Resolved Raman sideband cooling . . . 27
2.5.1 Coherent two-photon transitions . . . 28
2.5.2 Adressing motional sidebands . . . 29

3 Plane selection with an optical polarization gradient **35**
3.1 Concept . . . 36
3.2 Optical setup and alignment . . . 39
3.2.1 Optical system design . . . 39
3.2.2 Alignment . . . 42
3.3 Measuring atom distributions and light shifts in three dimensions . . . 46
3.4 Volume selection . . . 47
3.5 Feasibility of plane selection . . . 49
3.5.1 Stability . . . 49
3.5.2 Spin relaxation time T_1 . . . 50
3.5.3 Robust adressing pulses . . . 51
3.5.4 Comparison with other techniques . . . 52
3.6 Outlook . . . 54

4 Measuring the Wigner function **57**
4.1 The Wigner function as an observable . . . 58
4.2 Measuring the Wigner function at the origin . . . 59
4.3 State Reconstruction . . . 63
4.4 Conclusion . . . 67

5 Conclusion and outlook **69**

Bibliography **73**

A Computation for the Polarization Gradient **85**

B Electronics **87**
B.1 Amplified difference photodiode . . . 87
B.2 Current Stealing Circuit . . . 87

C Wavefront control at the level of $\lambda/78$ **91**

CHAPTER 1

Introduction

Since its establishment during the first half of the twentieth century quantum mechanics has revolutionized our worldview. At first astounding findings such as the Einstein-Podolski-Rosen paradox were only accessible through what is called a „Gedankenexperiment“. Studying quantum mechanical effects on the level of individual particles was deemed impossible. In 1952 Erwin Schrödinger said that „in the first place it is fair to state that we are not experimenting with single particles, any more than we can raise Ichthyosauria in the zoo“[13].

This changed during the second half of the last century. The invention of lasers [14, 15], novel vacuum pumps [16, 17] and cooling technology made it possible to trap single ions in Paul traps [18], study the behavior of individual microwave photons inside resonators [19, 20] and to trap neutral atoms in dipole traps [21].

These experiments triggered the advent of quantum technology, which entails the development and production of devices that can not be described using classical physics. These new technologies have since found applications in various fields such as communication and cryptography [22, 23], simulation and computation [4, 24, 25], metrology and sensing [26, 27]. The last decades have seen rapid progress and new bold visions [1, 2] like using quantum mechanics for simulating systems far too complex for classical computation methods. These quantum simulators are among the primary goals of this ongoing „quantum revolution“ [3].

Neutral atoms in optical dipole traps offer a platform to perform quantum simulations and quantum computation [4, 24]. One can exploit the analogy between atoms confined in a single layer of a three dimensional optical lattice and impurities confined within a boundary inside a solid state crystal. Moreover these systems allow the experimentalists to study particles that are exposed to artificial electrical [28] and magnetic fields [11] and study interference of identical particles [7, 29, 30].
These challenging experiments require atoms to be confined to a single layer of an optical lattice and that both their vibrational state in the optical trap and their internal state are well controlled.

The discrete time quantum simulator (DQSIM) experiment is designed to provide such an environment [6]. We trap cesium atoms in a two-dimensional state-dependent polarization-synthesized lattice that is situated below a high-NA objective lens (NA = 0.92) [8], which is used to detect the position of the atoms. Depending on their internal state, the atoms are trapped within one of two superimposed lattices that we can independently control and displace [31].

The DQSIM experiment is an ideal platform to investigate discrete time quantum walks in two dimensions, which can be used as a tool for quantum computation [32] and to measure artificial magnetic fields with a flux unobtainable by conventional means [11].

This Thesis is organized as follows. First, I will introduce the experimental apparatus with an emphasis on improvements I implemented during my time in Bonn. These include a current stabilization circuit, to provide a stable magnetic guiding field, improving the digital intensity stabilization to reach the shot-noise-level. Extending the dynamic range of the intensity feedback and implementing multiplicative intensity feed forward. Moreover I implemented resolved Raman sideband cooling utilizing the D1-line of cesium.

Chapter 3 introduces a novel technique for preparing thin slices out of a thick three dimensional atomic cloud. It uses light to induce a periodic vertical pattern of differential light shifts that allows to spectroscopically resolve the vertical distribution of the atomic cloud. I will first introduce the concept in section 3.1, and both the optical setup and its alignment in section 3.2. In section 3.3, I demonstrate how we can perform a tomography of the atomic cloud. The periodic modulation of the artificial magnetic field makes the reconstruction of the vertical distribution of atoms ambiguous. However, this ambiguity can be lifted by scanning not only the resonance frequency, but also the vertical position of the light field. In section 3.4, I demonstrate volume selection, where the thickness of the atomic cloud is reduced from more than 20 μm to less than 3 μm. This new method is then compared with the established technique of using Zeeman shifts for plane selection. As an outlook I present how we can optically resolve individual planes using the low depth of focus of DOF=200 nm of the high numerical aperture objective lens (NA=0.92).

The final chapter 4 deals with the to the reconstruction of vibrational states. There I propose a scheme to directly measure the Wigner function of trapped atoms in a state dependent potential. It employs Ramsey interferometry to measure the differential trapping frequency between both spin states. This can be used to implement the (displaced) parity operator whose expectation value is the Wigner function [33]. I conclude this thesis with a brief summary and an outlook for future experiments in section 5.

CHAPTER 2

Experimental Apparatus

In this chapter, I describe the discrete-time quantum simulator (DQSIM) machine. The experiment is built around a home-built twelve-sided vacuum chamber that offers excellent optical access. A two-dimensional state-dependent optical dipole trap is located below a high NA objective lens used to image the atom position.

I start with an overview of the experimental apparatus is given in section 2.1. I describe how neutral cesium atoms are loaded from a dilute background gas into a magneto-optical trap. We subsequently transfer them into a two-dimensional state-dependent optical trap which is described in section 2.3. We have to apply a magnetic guiding field to enable state-dependent transport of atoms. I designed a current stealing circuit to enable the long coherence times required for quantum simulations, which will be described in section 2.2. In section 2.4 I describe the polarization synthesizer that we employ to perform state-dependent transport operations and to control the lattice depth. We use digital control to realize nine feedback loops required to stabilize the phase and intensity of the five horizontal lattice beams.

The processing capabilities of our digital intensity and phase control allows us to linearize the system response, which increases the dynamic range of the intensity feedback. Feed-forward control of the lattice position in conjunction with internal model control increases the modulation bandwidth from 230 kHz to 3.3 MHz.

I conclude this chapter in section 2.5, where I demonstrate Raman sideband cooling along the vertical direction using the D1 transition of cesium. This complements the microwave mediated sideband cooling that we use to cool horizontally.

2.1 Overview

Quantum simulation requires us to trap and prepare atoms in a well-controlled environment. To accomplish this, we load them from a background vapor into a trapping potential and subsequently control their internal electronic and external vibrational state. In this section, I will describe the experiment at hand and give an overview of the techniques used.
A more detailed description of the setup can be found in the thesis of my predecessor Stephan Brakhane [5]. A detailed description of improvements made during the last years can be found in the thesis of my colleague Gautam Ramola [31]. The goal of the following text is to outline a framework for the remaining chapters and to present technical additions I included.

2.1.1 Experimental sequence

The experiments described in this thesis are stochastic. We repeatedly load atoms from a background vapor into an optical trap. The state of the atoms are prepared, and the position-dependent survival probability is measured using fluorescence images. Each experimental cycle consists of the following steps: First, we load atoms from a dilute background gas into a magneto-optical trap (MOT). The MOT is initially loaded 1 mm below the surface of a high-NA objective lens. The optical dipole trap is located 150 µm away from the objective surface. After transferring the atomic ensemble into the dipole trap, we use fluorescence imaging to detect the spatial distribution of atoms. Then the illumination parameters are changed to cool the atoms further, and the trap is lowered adiabatically to reduce the scattering rate from lattice photons. We employ resolved-sideband cooling to prepare about 80% of the atoms in the motional ground state and optical pumping to prepare them in the outermost mF-level $|\uparrow\rangle = |F = 4, mF = 4\rangle$ of the ground state. Once the process of optical pumping ends, we perform the (coherent) manipulation of the atoms. The quantities in questions are mapped onto the internal state of the atoms, which is subsequently determined by a destructive projection measurement. Afterwards, a push-out beam can be activated to remove all atoms remaining in $|\uparrow\rangle$-state.

2.1.2 The vacuum apparatus

Optical dipole traps have become a standard tool to study individual, neutral particles. They have typical depths corresponding to a temperature of a few mK or less. Their depth is limited by the finite power that is available from coherent laser sources and by heating due to dipole force fluctuations caused in deep traps [34].
These experiments are performed at room temperature, where cesium atoms have an average speed of nearly $200\,\mathrm{m\,s^{-1}}$. The time that atoms remain trapped in an optical dipole potential is limited heating processes such as position jitter of the lattice and by collisional losses with the background vapour that is at room temperature [35]. In section 2.1.3 I describe how we can actively cool the atoms and thereby negate gradual heating processes.

This increases the lifetime of the atoms to 10 s, which corresponds to the limit imposed by collisions with the background vapour. We use vacuum pressures of 3×10^{-10} mbar. Lower vacuum pressures are obtainable but at the cost of fewer atoms that are trapped in each cycle of the experiment. This trade-off can be overcome with a vacuum system with multiple chambers and differential pressures between the sections [36]. Our approach, however, does not require additional beams to transport atoms between sections of the vacuum chamber.

The experiment features a home build and patented vacuum chamber [38]. The dodecagonal shape of the vacuum chamber allows simultaneous optical access from twelve directions horizontally. It is made from leaded glass with very low birefringence[1]. The stress-induced birefringence is further reduced by the long distance between the position of the atoms and the weld ring connecting it to the remaining vacuum apparatus. This is beneficial because stress-induced birefringence is spatially inhomogeneous and would thus limit our ability to control the polarization state of light. The birefringence has been optically measured to be smaller than 10^{-7} for each window under vacuum pressure[38]. This result has been confirmed for two windows interferometrically using atoms as a meter [31]. My colleague Gautam Ramola used Ramsey interferometry to detect the vectorial differential light shift experienced by the atoms. This technique is more precise than spectroscopic methods employed in an earlier work from our group [39]. I will discuss the origin of the vectorial light shift in section 2.3.

[1] Schott SF57

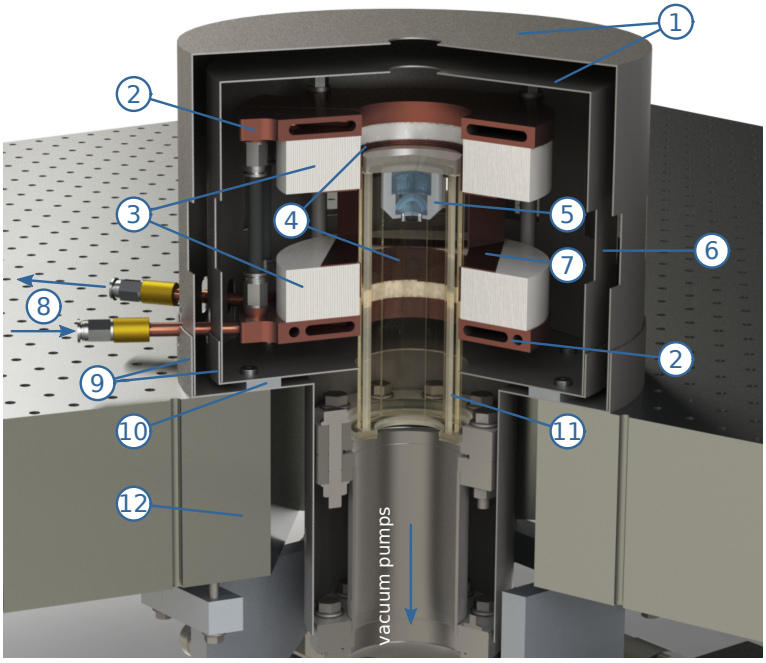

1 magnetic shielding
2 cooling plates
3 gradient coils
4 vertical compensation coils
5 imaging objective
6 rectangular openings
7 horizontal compensation coils
8 cooling water connections
9 overlap region
10 aluminium spacer
11 UHV glass cell
12 breadboard

Figure 2.1: Rendered image of the vacuum system, the magnetic coils and the mu-metal shielding. This image was taken from [37].

Figure 2.1 shows a rendered image of the vacuum system and the surrounding system of coils. These coils provide the magnetic bias- and quadrupole fields necessary to trap and transport atoms.

2.1.3 Collecting and preparing atoms

The average kinetic energy of thermal atoms from the background vapor is too high to load directly into the optical dipole trap. Instead, we use a magneto-optical trap (MOT) to collect and cool atoms. MOTs rely on velocity and position-dependent radiation pressure and were first realized in 1987 to cool sodium atoms [40]. The underlying process is called Doppler cooling and was proposed in 1975 [41] and realized in 1978 [42]. A schematic of the one dimensional model is shown in figure 2.2(a).

Doppler cooling and magneto optical trap The process of Doppler cooling can be explained using two-level atoms. The ground state $|g\rangle$ is stable and coupled to one excited state $|e\rangle$ with a life-time of $\tau = 1/\Gamma$ and an energy $\hbar\omega_0$. If a monochromatic laser beam with frequency ω and intensity I illuminates this atom, it will absorb and spontaneously re-emit photons. The scattering rate has a Lorentzian profile [43]

$$R_s = \frac{s_0 \Gamma/2}{1 \; + \; s_0 \; + \; (2(\delta + \omega_D)/\Gamma)^2} \tag{2.1}$$

It depends on the detuning $\delta = \omega - \omega_0$ of the laser from the atomic resonance and the saturation parameter $s_0 = I/I_{sat}$, which is its Intensity I relative to the saturation intensity I_{sat} of the transition. Atoms that move with velocity v relative to the laser beam experience a Doppler shift of $\omega_D = -\mathbf{k} \cdot \mathbf{v}$, where $\mathbf{k}$ is the wave vector. The scattering rate is velocity dependent, giving rise to velocity dependent radiation pressure. The absorbed photons transfer a net momentum along the beam direction but the

spontaneous scattering is isotropic.

Two counter-propagating laser beams that are slightly red detuned from the atomic resonance form a one-dimensional optical molasses. They can be used to cool atoms by exerting a viscous force (See figure 2.2(a)). If the atom moves towards one of the beams, the Doppler effect will shift it into resonance, thus increasing the scattering rate. Simultaneously the other beam is red-shifted out of resonance which reduces the radiation pressure it exerts. The resulting net force is proportional to the velocity resembling a viscous drag, hence the name optical molasses.

This scheme can be extended to three dimensions using three pairs of mutually orthogonal pairs of counter-propagating beams. This configuration creates viscous friction for atoms moving along any direction and was first realized in 1985 [44]. The atomic ensemble can reach temperatures below the "Doppler limit" $T_D = \hbar\Gamma/2k_B$, where k_B denotes the Boltzmann constant [45]. The Doppler limit arises when one considers a two-level atom undergoing constant cycles of absorption and spontaneous emission. The atom undergoes a random walk in momentum space leading to a finite root-means square velocity $\langle v \rangle$. In this model, the Doppler temperature is reached if heating and cooling rates are in equilibrium. We use the D2-line of cesium to provide cooling. Its natural linewidth is $\Gamma = 2\pi\, 5.2\,\mathrm{MHz}$ resulting in a Doppler temperature of $125\,\mu\mathrm{K}$. Subsequently, theoretical models were developed that explain sub-Doppler cooling with the multi-level structure of the atom [46–48]. One technique to cool below the Doppler limit is Sisyphus cooling, which we employ to cool atoms in the dipole trap while taking fluorescence images. Selection rules and the laser's polarization gives rise to state and position-dependent AC stark shifts and scattering rates. The recoil of photons limits the cooling process to $k_B T/2 = \hbar\omega_r$, where $\omega_r = \hbar k^2/2m$ denotes the recoil frequency [49].

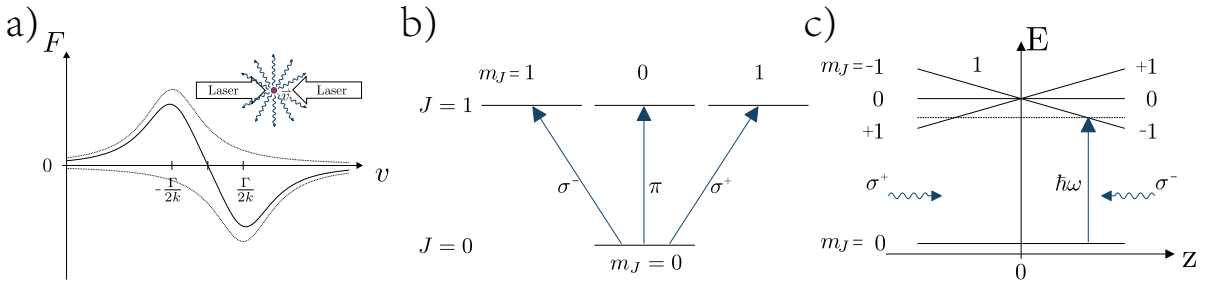

Figure 2.2: One dimensional schematic of a magneto optical trap. (a) The relative radiation pressure as function of the velocity. The Doppler effect gives rise to a velocity dependent shift in resonance frequency. The inset indicates the configuration. Two internal states are assumed and the counter propagating laser beams are red detuned by $\Gamma/2$ from the transition. The radiation pressure from both beams follows a Lorentzian line shape around the velocities where the Doppler effect compensates the detuning (grey dotted lines).(b) A simplified level scheme. The selection rule $\Delta m_J \in \{-1, 0, 1\}$ makes the absorption polarization dependent. (c) Position dependent restoring force. A magnetic quadrupole field gives rise to a position dependent Zeeman shift. This leads to a small region within which photons are preferentially absorbed from the beam pointing towards the origin.

The magneto optical trap The purely viscous force exerted by an optical molasse does not prevent the slow diffusion of particles. A position-dependent force is needed to trap atoms in a small spatial region. A quadrupole field in combination with circularly polarized beams can be used to modulate the atomic absorption spatially. Let us consider a simplified one-dimensional model where a degenerate $J = 1$ manifold is coupled to a single ground state $J = 0$. A magnetic field gradient lifts the degeneracy

of the excited states and the selection rule $\Delta m_J \in \{-1, 0, 1\}$ makes the absorption polarization-dependent, as shown in figure 2.2(b). Suppose the beams are red detuned relative to the atomic transition and have orthogonal, circular polarization, then the magnetic field gradient shifts the atomic resonance in and out of resonance as shown in figure 2.2(c). An atom that sits at the right side in figure 2.2(c), will absorb more photons from the σ^--beam and vice versa. This results in a restoring force that pushes the atom towards the center of the magnetic field.

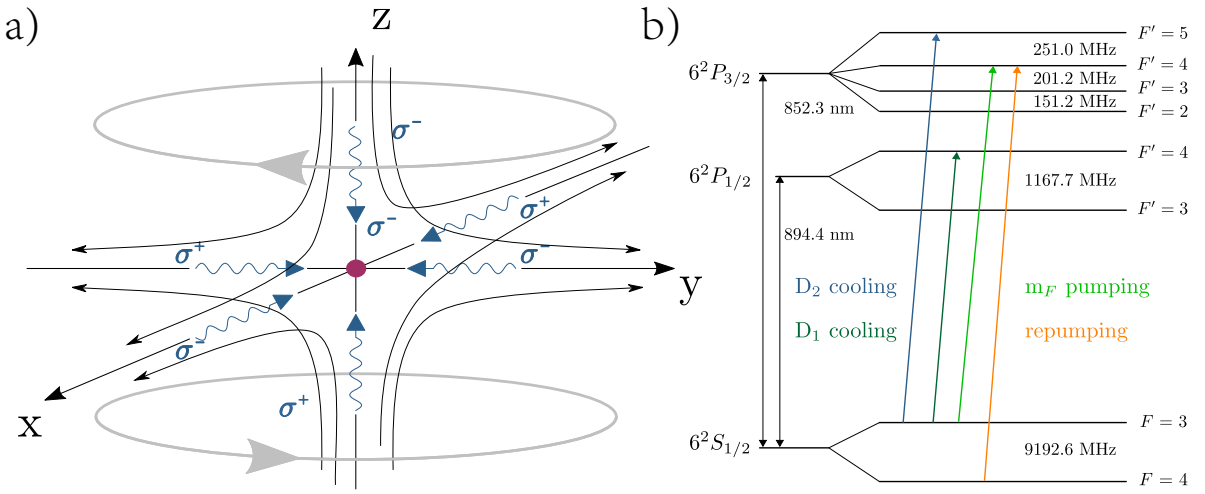

Figure 2.3: Three dimensional model of the MOT and optical transitions. (a) The grey circles indicate the current generating the quadrupole field. (b) The transitions used for cooling, imaging and state preparation.

This scheme can be extended to three dimensions by using three pairs of counter-propagating beam that intersect at the center of of quadrupole field, as shown in figure 2.3.

I helped enlargen MOT's size to increase the loading into the dipole trap from a few tens of atoms to a few thousand. The details can be found in the work of my coworker Gautam Ramola [31]. It is experimentally challenging to load the MOT 150 µm below an optical surface with a radius of 6 mm. Our solution is to load the MOT about 1 mm below the surface of the objective lens. We subsequently transport the MOT to the position of the lattice beams by moving the center of the quadrupole field using homogeneous bias fields.

State preparation and detection We use fluorescence imaging to detect the horizontal position of the atoms in the dipole trap. Our high-NA objective lens is the first of two lenses in a 4-f configuration to image the atoms onto an EMCCD-camera[2]. We use light resonant to the closed transition $F = 4 \rightarrow F' = 5$ the D_2-line. Optical filters block light from the vertical dipole trap at 1 064 nm and D_1-cooler light at 895 nm. The latter cools the atoms along the vertical direction. A more detailed description of the imaging system and its current state can be found in [31].

The light driving the imaging transition is provided by three pairs of counter propagating beams with linear, mutually perpendicular polarization. They provide polarization gradient cooling, which is a type of sub-Doppler cooling [48]. We have two sets of parameters for intensity and the detuning. While acquiring images the parameters are chosen to maximize the scattering rate while maintaining long

[2] Andor iXon Ultra 897

life-times. After the image acquisition, we optimize for cooling efficiency and reach a ground state population of about 30% per direction. The optimization is done by measuring and minimizing the losses from evaporation. The ground state population is measured by resolved sideband cooling, which will be discussed in section 2.5.

2.2 Current stabilization at the 1ppm level

Long coherence times are needed to perform quantum simulations, and multi-step quantum walks with high fidelity [8]. In this section, I will introduce Ramsey interferometry as a tool to measure magnetic fields and the coherence time of our system. The central part of this section is dedicated to a home-build current stabilization circuit that combines a high feedback bandwidth of 100 kHz with low drift of 0.5 ppm. The high feedback bandwidth allows using a relatively noisy current source with ripple noise in the order of 1 mV_{pp}. The residual fluctuations of the magnetic guiding field are negligible in comparison to other sources of decoherence. I conclude with a comparison with other methods of stabilizing the current.

We apply a magnetic guiding field to lift the degeneracy of the mF-sublevels. Adjacent mF-sublevels are split 1.33 MHz apart, allowing us to resolve them using microwave radiation. The Hamiltonian that describes the interaction between the internal state of the atom can be reduced to an effective two-level system.

Spin dynamics in an effective two level system Microwave radiation can be used to couple the two outermost hyperfine levels of the ground state. Qubits are objects that can be described as effective two level system under the influence of an electromagnetic field.

In this work we use the semi classical Rabi model to describe the dynamical behavior [50]. The internal state of the atom is quantized and the external field is treated classically. Pure states can be described using a single wave function of the form

$$|\Psi\rangle = c_e|\uparrow\rangle + c_g|\downarrow\rangle. \tag{2.2}$$

Spontaneous emission and scattering e.g. lattice photons transform the initially pure state into a statistical mixture, that can be described using density matrices ρ [50]. It holds

$$\rho = \begin{pmatrix} \rho_{ee} & \rho_{eg} \\ \rho_{ge} & \rho_{gg} \end{pmatrix} = \begin{pmatrix} |c_e|^2 & c_e c_g^* \\ c_e^* c_g & |c_g|^2 \end{pmatrix} \tag{2.3}$$

The dynamics of a two-level system can be depicted geometrically using the Bloch sphere [51]. The state of the system is represented as a Bloch vector $\vec{R}$ that is defined as

$$\vec{R} = \begin{pmatrix} \mathrm{Re}\left(\rho_{ge}\right) \\ \mathrm{Im}\left(\rho_{ge}\right) \\ \rho_{ee} - \rho_{gg} \end{pmatrix} \tag{2.4}$$

The time evolution is described by the optical Bloch equation

$$\mathrm{d_t}\tilde{\mathrm{R}} = \tilde{\Omega} \times \tilde{\mathrm{R}} \tag{2.5}$$

where the Bloch vector precesses around the torque-vector $\vec{\Omega}$

$$\vec{\Omega} = \begin{pmatrix} \mathrm{Re}\left(\mathcal{H}'_{ge}\right) \\ \mathrm{Im}\left(\mathcal{H}'_{ge}\right) \\ \hbar\delta \end{pmatrix} \tag{2.6}$$

In the experiment at hand we measure the behavior of atom ensembles that are exposed to random fluctuations of the environment.

2.2.1 Measuring magnetic fields using Ramsey interferometry

Ramsey interferometry was invented by Norman Ramsey to study resonances of molecular beams [52] but since became a widespread tool to study spin coherence of qubit systems, such as superconducting qubits [53], neutral atoms [54] and trapped ions [55].

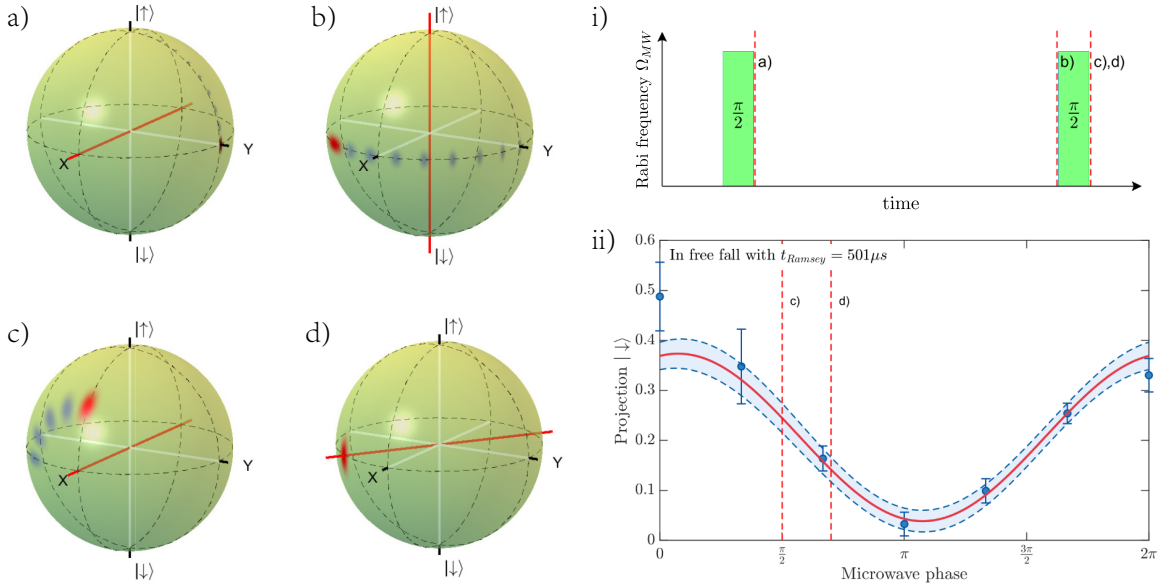

Figure 2.4: Representation of a Ramsey sequence on a Bloch sphere. (a) An initial $\pi/2$ pulse rotates the internal spin to the equator. (b) The spin then freely precesses along the equator and around the north pole. (c),(d) A second $\pi/2$ pulse rotates the spins around an arbitrary axis on the equator. (ii) Ramsey fringe. A set of projective measurements is called a Ramsey fringe and its contrast is measures of the variance of the phases that the ensemble of atoms acquires. External noise as well as experimental imperfections lead to a non vanishing spread of the ensemble of spins as indicated by the shading. As a consequence the contrast of the measured Ramsey signal is reduced. The red lines in (i) indicate the time of the depictions in (a)-(d) and the red lines in (ii) represent the phase corresponding to the rotation axes in (c) and (d).

A Ramsey interferometer consists of two $\pi/2$ pulses that are separated by a hold time during which the particle collects a phase relative to the external field. The phase of the second pulse is scanned and the state of the particle is projected on either of the spin-species, as shown in figure 2.4.
The system is initially prepared in $|\uparrow\rangle$ which corresponds to the north pole of the Bloch sphere. The first $\pi/2$ pulse rotates the spin to the equator, creating an equal superposition of both spin states. The spinor moves along the equator as the atom acquires a phase relative to the local oscillator of the driving field. A second $\pi/2$ pulse rotates the Bloch vector around an arbitrary axis on the equator that depends on the phase ϕ_{MW} of the microwave field during.

The Ramsey signal can be expressed using a simple sinusoidal model [54]

$$P_{|\uparrow\rangle} = \frac{S}{2}\left[1 + C(\tau)\cos\left(\phi_{MW} + \Phi(\tau)\right)\right] \tag{2.7}$$

where S is the (survival) probability of an atom remaining in the trap if no projection measurement is performed, ϕ_{MW} the phase of the second $\pi/2$-pulse and $\Delta\Phi$ is the average phase collected by the ensemble of atoms. The average phase

$$\Delta\Phi(\tau) := \int_0^\tau \Delta\delta(t)\mathrm{d}t \tag{2.8}$$

depends on the detuning $\delta(t) = 2\pi\ (\nu_{MW} - \nu_{\Delta E})$ between the microwave frequency ν_{MW} and the atomic resonance frequency $\Delta\nu = (E_\uparrow - E_\downarrow)/h$. Ramsey interferometry can therefore be used to measure Zeeman shifts and hence the magnetic field strength as shown in figure 2.5(b). The atoms are released from the trap to avoid differential light shifts induced by the lattice. The magnetic field is not uniform, but exhibits a gradient of 42 mG cm^{-1}. We assume, that the coils generating the guiding fields are shifted by a few milli meter. Ramsey interferometry can also be used to measure the variance of the detuning [54], because the contrast depends exponentially on variance of the collected phase

$$C(\tau) = exp(-\Delta\Phi^2(\tau)/2). \tag{2.9}$$

The coherence time is larger, when the analysis is restricted to a small region as shown in figure 2.5(c). Here I use the 1/2-time of the contrast to define the define the inhomogeneous or reversible dephasing time T_2^*. The homogeneous or irreversible dephasing time $T_2^{'}$ can be measured using Hahn's spin-echo sequence [54]. This measurement extends the Ramsey sequence by an additional π-pulse that reverses the spin-dynamics in the middle of the Ramsey interrogation time [56]. It measures the Allan variance of the phase acquired by the atomic ensemble [54].

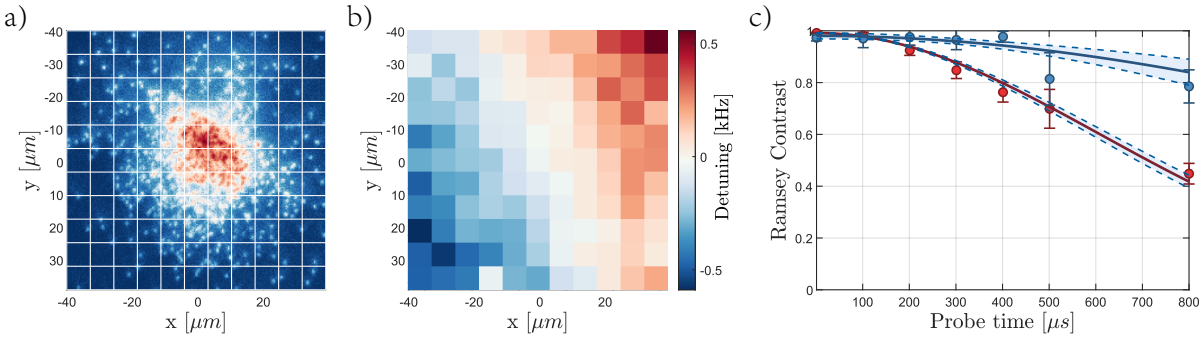

Figure 2.5: Magnetic field gradient in free fall and coherence time. (a) Average initial atom density. The rms width of the atom cloud is 12 µm. Spatial information can be obtained by analyzing the image section wise. (b) Magnetic field gradient. For each macropixel the average detuning is inferred from the phase acquired after τ =800 µs. The gradient of $\nabla\delta$ =10.4 Hz µm^{-1}, or $|\nabla\vec{B}|$ =42 mG cm^{-1} is aligned along the quantization axis. (c) T_2-time analysis. The spin-dephasing time across the entire atom cloud is limited by the magnetic field gradient to T_2 = 710 (690|735) µs. If we restrict our analysis to the central section, the coherence improves to T_2 = 1.7 (1.4|2.1) ms.

A phenomenological model of decoherence has been provided by Alberti et al. [57]. The total variance of the phase is given by the sum of variances from each individual source. One of them are uniform

fluctuations of the magnetic field. If we neglect all ambient magnetic fields[3], we can assume the magnetic field to be proportional to the current of the guiding field and compute the variance of the collected phase from the magnetic field noise power spectral density S_B

$$\Delta\Phi^2(\tau) = \frac{\tau^2\mu_B^2}{\hbar^2}\left[m_F(\uparrow)g_F(\uparrow) - m_F(\downarrow)g_F(\uparrow)\right]^2 \int_0^\infty d\omega\ sinc^2\left(\frac{\omega\tau}{2}\right) S_B(\omega) \tag{2.10}$$

In this formula we have to implicitly assume a low-frequency cutoff at times equal to a typical experiment. From equation 2.10 it follows, that the variance of the phase increases linearly with the probe time τ in the case of white noise, that has a constant power spectral density S_w. If the noise is dominated by low frequency drifts, then the variance will grow quadratically

$$\Delta\Phi^2(\tau) = \begin{cases} 2\pi^2 S_w \tau & S_\nu(f) = S_w \\ 4\pi^2\sigma_\nu^2\tau^2 & S_\nu(f) \approx 0, f > 0.1\tau \end{cases} \tag{2.11}$$

The spectrum can be split into two sections. Low frequencies correspond to slow drifts of the average field. They are also called to shot-to-shot fluctuations and cause the detuning to change between different iterations of the experiment. Magnetic field noise at high frequencies will cause the spinors to undergo a random walk during each individual iteration. A current source is needed that has both a high absolute stability leading to a low drift and low high frequency noise.

2.2.2 Concept of stealing

The magnetic field is generated by the compensation coils used to shift the magneto-optical trap. They have an inductance of 2 µH and are driven with 2 A to generate a field of 3.27 G. The resonance frequency between the two outermost mF-states changes by 9.31 MHz. Using equation 2.11, we can estimate the coherence time. Typical commercial available power supplies have relative stabilities between 250 ppm[4] and 25 ppm[5], which corresponds to spin-dephasing times between 800 µs and 8 ms.

In the following, I will describe the current stabilization circuit, a schematic of which is shown in fig. 2.6. We use a low-cost linear power supply[6] as a tunable current source that provides an excess current of about 10%. The current stability is improved with the second stage of stabilization. The idea is to deliver an excess of current from the power supply and a variable resistor to bypass the excess current. Additional components such as isolation coils and bypass capacitors are needed to achieve a high feedback bandwidth.

An N-channel MOSFET[7] is used as a shunt, which is installed in parallel to the coils and bypasses a variable amount of the current. The current is measured using a Kelvin probe[8] and an instrumentation amplifier[9]. A high stable, low noise voltage reference[10] is used to derive an internal set point, and a PI-controller is used to provide feedback. It is possible to modulate the set point externally using a differential input to compensate fluctuations of the ambient magnetic field [58]. More details and a schematic drawing of the circuit board can be found in appendix B.

[3] This is reasonable because the μ-metal shielding suppresses ambient magnetic fields by a factor of >2000 [31]
[4] Keysight, M3633A
[5] High Finesse, BCS series
[6] Elektro Automatik EA-PS-3020B
[7] IRF540
[8] Isabellenhütte: AZ-H2-R100-F1-K2-0.1-TK3
[9] INA128
[10] Analog Devices: AD587

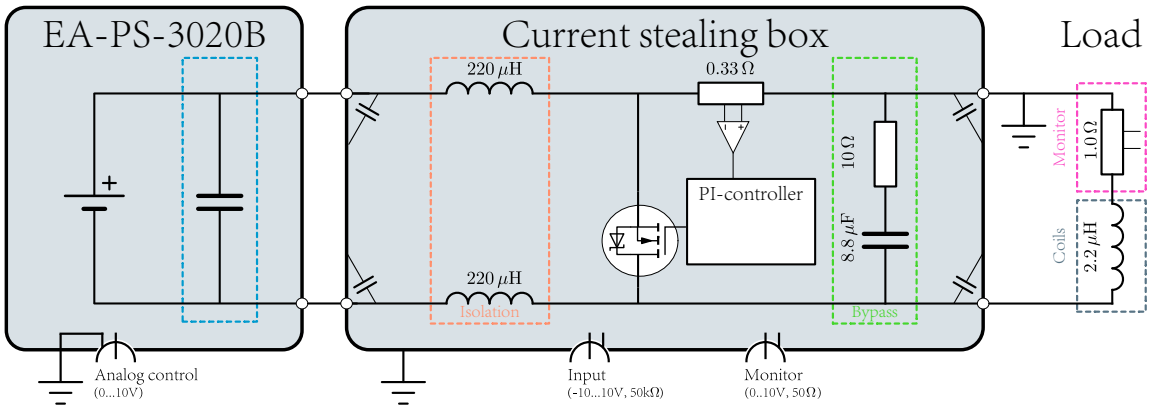

Figure 2.6: Schematic drawing of the current stabilization. A low noise linear power supply is used as current source (Elektro Automatik EA-PS-3020B), driving the pair of coils (2.2 µH. The relative stability is limited to 1 000 ppm by self heating causing it to drift during the first 30 min. A second stage of stabilization is required to reach a relative stability of 1 ppm. High current inductors (orange box) are used to provide impedance that isolate the second stage from the internal feedback of the current source. Linear power supplies typically use large capacitors (blue box) to reduce voltage noise. A Kelvin probe is used as shunt resistor to measure the current and a MOSFET (IRF 540) is used as variable resistor to provide feedback. An RC-low pass filter (green box) is installed to act as a lead-lag-filter to the feedback loop. It provides a path for fast modulation of the current and flattens the system response seen by the PI-controller. Another Kelvin probe (purple box) is used to monitor the current through the coils (gray box). The current stealing box also provides a differential input to (add) an external voltage reference and a differential output to monitor either the shunt current or the error signal.

The isolation coils and the bypass capacitors shown in figure 2.6 are necessary to achieve high feedback bandwidth. The suppression of a specific noise component can be estimated using the gain-bandwidth-product (GBW)[59]. In a linear PI controller the GBW equals the frequency f_{bw} at which the gain drops to unity and the suppression at frequency $f < f_{BW}$ is given by $S = f/f_{bw}$. It is possible to use a double integrator to increase the gain at low frequencies. This however introduces an additional phase delay of 90° and renders the circuit unstable if it is not compensated or the bandwidth is reduced.

Linear power supplies typically have large capacitors at the output to reduce ripple noise [59]. This decreases the output impedance of the current source as the frequency increases. Without the isolation coils a fast modulation of the shunt resistance would load and unload the output capacitor instead of changing the current through the Kelvin probe. One approach is to measure the transfer function I_{Inloop}/I_{Bypass} and compensate the non-ideal frequency response with filter stages in the feedback loop [60]. Instead of this I installed isolation coils between the power supply and the shunt to increase the output impedance for high frequencies. The isolation coils have to meet four criteria. Their inductance must be larger than the inductance of the coil providing the magnetic field. Their current rating must be sufficiently large, their lowest self-resonance must be well above the feedback bandwidth and they must have closed core. A closed core is important to prevent leakage flux but more importantly to prevent the coils from picking up external magnetic fields (e.g. at 50 Hz and harmonics).

For Currents below 10 A coils with closed ferrite cores and commercially available [11]. They are compact (30mm*25mm*21mm) and offer impedances of hundreds of µH and self-resonance frequencies above 1 MHz. A typical application that requires currents beyond 10 A is plane selection. If we were to

[11] WE-HCF SMT-Hochstrominduktivität "74437529203221" 220 µH, f_{res} =2.8 MHz, I_{sat} =5.3 A, Material: MnZn

stabilize the quadrupole field in our setup, we would drive currents up to 30 A through an inductive load of 12 mH and a self-resonance frequency of 60 kHz [5]. Coils with iron-powder cores and rated currents up to 50 A and 50 mH are commercially available [12]. The material has a larger saturation flux but limits the bandwidth of the coils to ca. 100 kHz.

The system response is further linearized by installing a bypass-capacitor parallel to the coil. This reduces the impedance of the load attached downstream of the Kelvin probe, thereby preventing the impedance of the coils to cause a phase-delay of the current through the Kelvin probe. The bypass capacitor acts as a lead-lag filter as shown in figure 2.7(a). Resistors have to be installed to dampen resonances between the compensation coil and the bypass capacitor and between the power supply and the load.
The feedback bandwidth slightly exceeds 100 kHz. The feedback loop can be faster, but the MOSFET is a highly non-linear device, which means the the gain of the system changes with the amount of current that is bypassed. It is therefore necessary to make a compromise between feedback bandwidth and dynamic range. A typical current ramp is shown in figure 2.7(b). The desired current is reached within 3.5 ms instead of 10 ms (note the onset of stealing at 3.3 ms). Without the current stealing the current fluctuates by over 10 kHz, as shown in the see top plot of figure 2.7(b)). This makes further stabilization necessary.

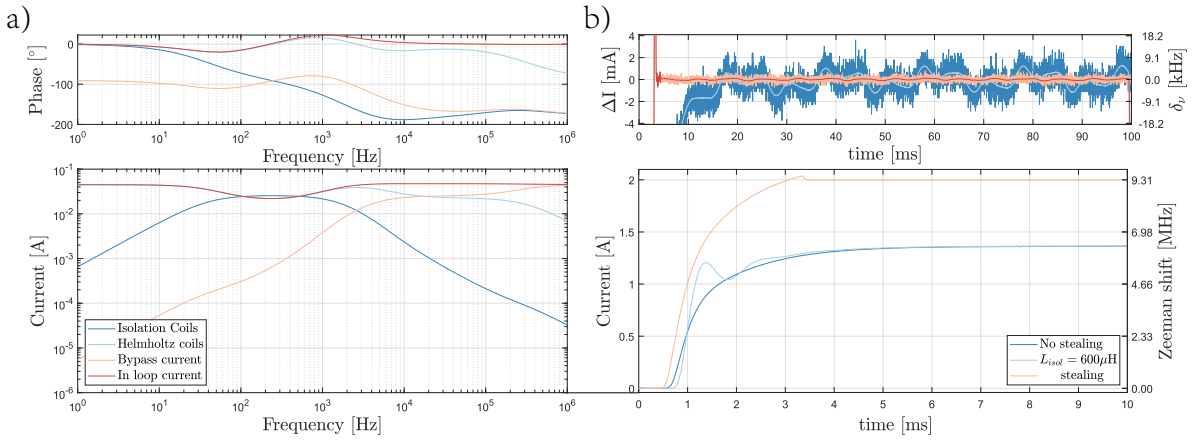

Figure 2.7: (a) Frequency response. The shunt MOSFET is replaced by an equivalent voltage source with finite output resistance. The frequency is response is of the in-loop current is nearly flat, which is a requirement for stable, high bandwidth current feedback. (b) Step response of the current through the coils of the guiding field. The settling time is only 3.5 ms and without stealing it is nearly 10 ms. Resistors have to be installed to ensure stable operation. If the load is (mostly) inductive, the current oscillates (light blue curve). Without stealing the current fluctuates by 2 mA (peak-to-peak), which corresponds to 10 kHz. The fluctuations of the current is are smaller than the measurement noise.

2.2.3 Characterizing the performance

The performance of the stabilization circuit was measured electronically using a Kelvin probe and spectroscopically by means of Ramsey interferometry.

The current noise through the coils was measured using a temperature stabilized Kelvin probe with

[12] Hammond heavy current chassis mount "195J30" 10 mH, f_{res} =2.8 MHz, I_{sat} =30 A, Material: MnZn

1 Ω resistance[13]. The performance of the stabilization at frequencies between 10 Hz and 1 MHz was measured using a spectrum analyzer[14] and a preamplifier [15]. Great care has to be taken to remove background noise from the measurement. Ground loops are removed by making a differential voltage measurement as well as grounding both measurement devices via the case of the current stabilization box. Ferrite chokes were installed between the Kelvin probe and the preamplifier to block noise at high frequencies to cause voltage offsets at the input stage. The lower frequency components of the noise were computed from time traces recorded with a digital multimeter [16] that offers a precision up to 7.5 digits. The results are summarized in figure 2.8.

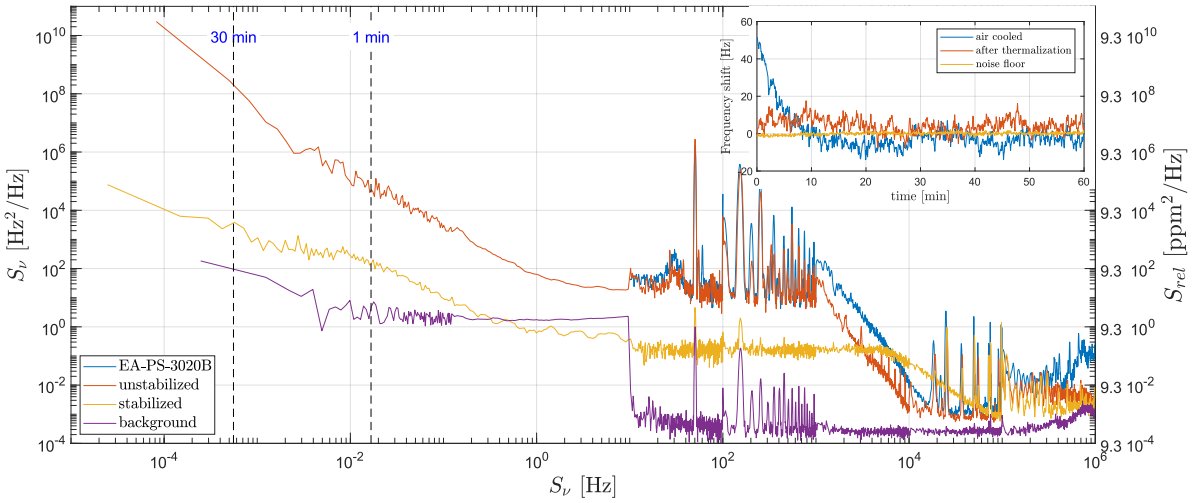

Figure 2.8: Frequency noise with and without current stealing. The current was measured using a 1 Ω Kelvin probe and the axis has been rescaled to show the equivalent noise of the qubit transition frequency. The spectral components below 10 Hz are computed from time traces. The noise at higher frequencies were measured using a spectrum analyzer. The inset shows the drift of the resonance frequency before and after thermalization. The measurement noise is subtracted from the PSD between 0.25 Hz and 10 Hz.

The current stealing box acts as a low pass-filter when turned off and the broad band white noise falls off above 1 kHz. The ripple noise at 50 Hz and its harmoncis and the the low-frequency drift of the current remain unaffected.
The current stabilization suppresses the ripple noise by nearly three orders of magnitude, because the feedback bandwidth is larger than 50 kHz. The broadband noise between 10 Hz and 1 kHz is limited by the input referred voltage noise of the differential amplifier. It corresponds to 10 nV $\sqrt{\text{Hz}}^{-1}$ at the input of the instrumentation amplifier which is in very good agreement with its datasheet. A second stabilization circuit of this type was built for our one-dimensional lattice experiment [58]. The resistance of its Kelvin probe is three times larger and the level of the broad band noise is three times smaller.

Equation 2.10 can be used to predict the coherence time from the power spectral density of the frequency noise. The spectrum is split into three parts. Slow frequency drifts that can be described by $1/f^\alpha$ noise, broad band white noise that extends up to the corner frequency of the low pass filter and ripple noise.

[13] Isabellenhütte: AZ-H2-1R00-F1-K2-0.1-TK3
[14] HP3589A
[15] Stanford Research SR560
[16] Keysight34470A

Without current stabilization the broad band, white noise has a PSD of S_w=30 Hz^2 Hz^{-1} which limits the coherence time to 2.4 ms. The decoherence is however dominated by the low frequency components that can be described with $S_{1/f} = 30/f^2$ Hz^2 Hz^{-1}. The coherence time drops to 700 µs for a measurement that takes 30 min and 470 µs after 5 hours. The experiment is synchronized to the AC power line hence to the ripple noise at 50 Hz and harmonics. Without synchronization the coherence time drops to 65 µs.

With active current stealing the ripple noise (nearly) vanishes in the white noise, that limits the coherence time to 290 ms. This is in the same order as the spin-relaxation time of 330 ms. If the resistance of the Kelvin probe is increased to 330 Ω then coherence time could extend to nearly 1 ms. The coherence time is however limited by the low-frequency components $S_{1/f} = 1/f^{1.1}$, which limits the coherence time to 50 ms after 30 min, 44 ms after 5 h and settling to 36 ms after 50 h.

The noise model above assumes the noise to be stationary. The current stealing box will however heat up at the beginning of an experimental sequence as shown in the inset of figure 2.8. In this case we can use equations 2.9 and 2.11 to compute the coherence time directly

$$T_2^* = \sqrt{\frac{log(2)}{2\pi^2\sigma_f^2}} = 21\,\text{ms}. \tag{2.12}$$

The temperature stability of the system is limited by the instrumentation amplifier to 25 ppm. The stability of the circuit can hence be improved by thermally isolating the instrumentation amplifier from the MOSFET and the Kelvin probe. The rms fluctuations of the relative current noise drop to 0.45 ppm after thermalization.

I measured the average detuning as a function of the hold time after the line-trigger (see figure 2.9. The rms modulation of the resonance frequency is σ_ν =19 Hz, which corresponds to a T_2- time of 9.4 ms. The accumulated current noise between 40 Hz and 160 Hz leads to a Zeeman shift of 7.6 Hz. A similar measurement has been carried out with atoms in our one-dimensional lattice (see figure 2.9(a)) [61]. The rms detuning is $\sigma_{\nu,1d}$ =1.9 kHz, which means that the experiment at hand is nearly a hundred times more stable. Now I will summarize the results and compare the stabilization circuit with alternative designs.

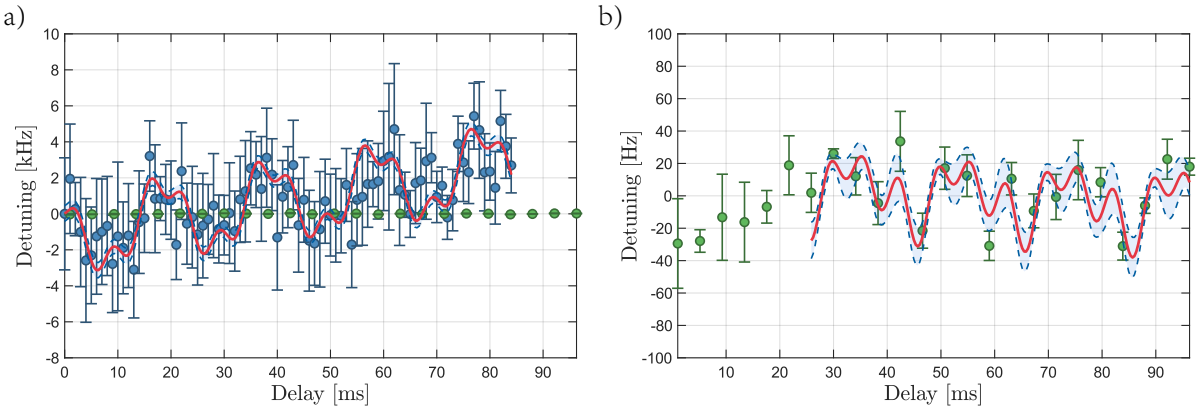

Figure 2.9: Resonance frequency vs hold time. (a) Comparison between an experiment with(green points) and one without (blue points) mu-metal shielding. The rms modulation of the detuning is decreased by two orders of magnitudes. (b) Rescaled frequency axis, to show the residual fluctuations. The red curves are a non-linear fit, assuming a linear drift and ripple noise. The blue data points in (a) is taken from [61].

2.2.4 Discussion and conclusion

Stable magnetic fields can also be realized by employing flux gate sensors for active stabilization [60] or with permanent magnets [62]. Ruster et al [62] report inhomogeneous coherence times of (350 ± 60) ms using $^{40}Ca^{+}$-ions and permanent magnets. This is – to my knowledge – the world record for qubits that are sensitive to magnetic fields. It is however, technically challenging to install a sufficient number of permanent magnets to achieve flat magnetic fields. Merkel et al [60] report on an active stabilization scheme using a fluxgate sensor and a shunt to stabilize currents up to 60 A and magnetic fields of 146 G to the level of 0.29 ppm. This corresponds to residual magnetic field fluctuations of 43 μG. Fluxgate sensors are well suited to stabilize currents up to several hundred amperes because they are galvanically isolated from the current that needs to be stabilized. Also, their self-heating is independent of the current. Fluxgate sensors detect magnetic fields using periodically driven coils [63, 64]. A typical value is 3 kHz[60]. This means that it is not only necessary to apply notch-filters that work at their switch frequency (typically around 17 kHz) but also that the feedback bandwidth is limited due to the phase-delay introduced by these filters. This limits the ability of the feedback loop to suppress noise at the mains frequency and its harmonics.

In this section, I have presented a state-of-the-art current stabilization circuit with relative stability of 0.6 ppm. The corresponding fluctuations of the magnetic field are 2 μG, leading to a shift in the atomic resonance frequency of 5.6 Hz. This limits the spin dephasing time to values beyond 30 ms, which is much longer, than our measured coherence time (in free fall) of 1.7 (1.4|2.1) ms.

This coherence time is the longest that we have achieved in our group with magnetic field sensitive states. It is also on par with coherence times reported by Merkel et. al [60]. I expect a further increase in coherence time The dephasing might be caused by vertical magnetic field gradients, since we are probing an atomic cloud that extends up to 20 μm vertically. The inhomogeneous dephasing time should be measured again after performing plane selection.

So far we have discussed the coherence time of atoms in free fall. In the optical lattice the coherence time is reduced to ca 1 ms, due to differential light shifts [31]. The lattice potential and its stabilization will be discussed in the following section.

2.3 Laser configuration and the optical dipole potential

Far detuned optical dipole traps are a powerful tool to trap and study neutral atoms [4]. The dipole force is much weaker than the radiative pressure exerted by a magneto-optical trap. This enables long coherence times in dipole traps because they do not rely on the incoherent scattering of photons. In the following, I will discuss the origin of the dipole force holding the atoms inside the nodes of the light field. Then I will discuss the geometry and properties of our state-dependent optical lattice. I conclude with an overview of the laser sources providing the light.

Dipole Force The theory of AC-Stark shifts can be applied to a two level atom driven by an off-resonant laser field.

A semi-classical approach that employs the Lorentz model provides an intuitive picture to understand the origin of the dipole force that arises from the interaction between an atom and a driving laser field. This approach is explained, e.g. in [65], and it correctly describes the case where the light is linearly polarized, and relevant atomic levels are not resolved. One finds that atoms in the ground state are attracted towards the maxima of the intensity in the red-detuned case and repelled in the blue detuned case. The light is red-detuned if the laser frequency ω is smaller than the transition frequency ω_0 and

blue-detuned if it is larger. Both the potential depth U and the scattering rate R_s are proportional to the intensity I

$$\begin{aligned} U_{\text{dip}} &= \frac{3\pi c^2}{2\omega_0^3} \frac{\Gamma}{\Delta} I \\ R_{\text{s}} &= \frac{3\pi c^2}{2\hbar\omega_0^3} \left(\frac{\Gamma}{\Delta}\right)^2 I \end{aligned} \tag{2.13}$$

Here Γ denotes the decay rate of the excited state into the ground state. We observe that the number of scattering rate per unit potential is inversely proportional to the detuning $\Delta = \omega_0 - \omega$.

The semi-classical approach can be extended to account for multilevel atoms by taking the sum over the independently computed contributions of each transition, but only in the case of linear polarization and in the limit of large detunings. The experiment at hand is, however, designed with the goal of trapping and transporting the atoms spin dependently [5, 6]. Several theoretical approaches exist to explain the interaction between multilevel atoms, and light fields of arbitrary polarization [66–68]. One such is second-order perturbation theory that can be used to compute AC-stark shifts quantum mechanically [65, 68]. This gives rise to the dressed state picture, and in this approach, the eigenenergies are shifted due to the external driving field hence the name "light shifts". This gives rise to a conservative potential U that is proportional to the intensity I. A systematic treatment and references to alternative (ab initio) approaches of computing the dynamical polarizability can be found in [68]. Following [65] we derive

$$U = -\frac{\pi c^2 I}{2} \sum_{j,k\in\{1,2\}} \frac{\Gamma_{Dj}}{\omega_{Dj}^3} \frac{j + (\text{-}1)^j \mathcal{P} g_F m_F}{\omega_{Dj} + (\text{-}1)^k \omega}. \tag{2.14}$$

Here g_F is the Landé factor, ω_{D_j} and Γ_{D_j} denote the transition frequencies and natural line widths of either D-line. The rotating wave approximation can be performed by omitting the index $k = 2$. The factor P depends on the polarization of the light

$$\mathcal{P} = \begin{cases} 0 & \pi \\ 1 & \sigma^+ \\ \text{-}1 & \sigma^- \end{cases} \tag{2.15}$$

The contributions of higher excited states beyond the D-line are omitted because their relative contribution is several orders of magnitude smaller for the wavelengths that are used to form our vertical dipole trap (λ =1 064 nm) and our horizontal dipole trap λ =866 nm.

We distinguish the scalar light shift, which is the spin-independent contribution in equation 2.14, and the vectorial light shift that depends on the polarization of the light field. If the light field has a wavelength between the D_1 and the D_2 line of cesium, strong vectorial light shifts are present. The dipole force becomes highly sensitive to the internal state and the polarization. We can exploit this by choosing a wavelength where the higher of our qubit states ($|\uparrow\rangle = |F = 4, mF = 4\rangle$) becomes insensitive to the σ^--component of the light field. If we apply the rotating wave approximation to equation 2.14 we get

$$\begin{pmatrix} U_\uparrow \\ U_\downarrow \end{pmatrix} = c_0 \left[b_0 \begin{pmatrix} 0 & 0 & 9\cdot 10^{-5} \\ 1 & -0.7 & 0.15 \end{pmatrix} + \begin{pmatrix} 1 & 0 & 1/2 \\ 1/8 & 7/8 & 1/2 \end{pmatrix} \right] \begin{pmatrix} I_{\sigma^+} \\ I_{\sigma^-} \\ I_\pi \end{pmatrix} \tag{2.16}$$

with $c_0 = -k_B \times 2.717\text{p}K/(W/m^2)$ and $b_0 = -0.0013$. It should be mentioned that we get a slightly different magic wavelength of $\lambda_{magic} = 866.1nm$ if we do not perform the rotating wave approximation. The light shift changes by circa 1.3%. This is in contrast to dipole traps at 1 064 nm where the rotating

wave approximation introduces errors in the order of 10% [69].

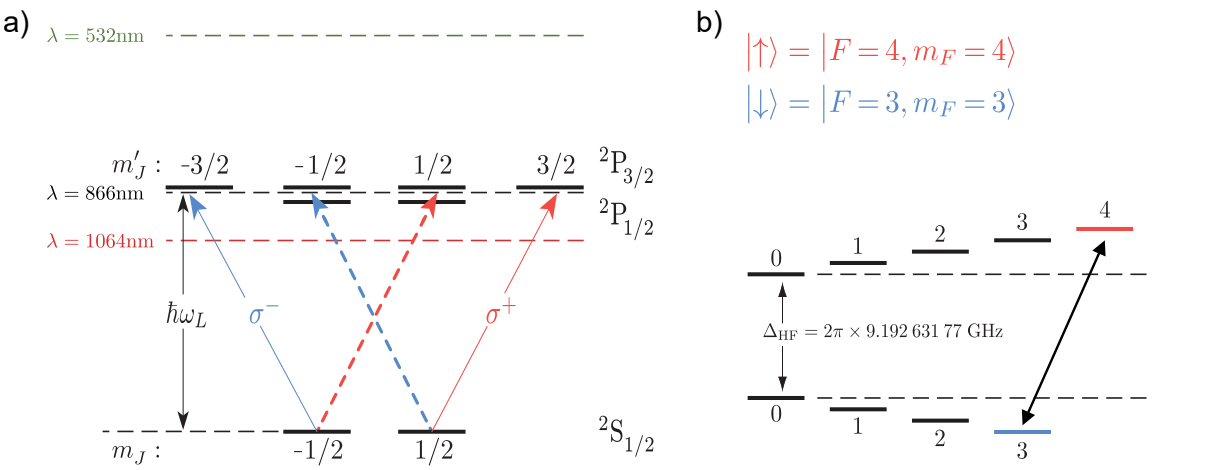

Figure 2.10: (a) Fine structure the lowest electronic states of cesium. The colored arrows represent transitions of circularly polarized light at the frequency $\approx \omega_L$. If this frequency is set within the D line doublet, then the the potential contributions from the $m_j = \pm 1/2$ magnetic sublevels of the two excited states (almost) cancel each other out. (b) A magnetic field lifts the degeneracy of the Zeeman sublevels to the point that they can be addressed individually. We choose the outermost, or maximally stretched sublevels as the two states of the two level system $|\uparrow\rangle = |F = 4, m_F = 4\rangle$ and $|\downarrow\rangle = |F = 3, m_F = 3\rangle$.

Differential light shifts The external field can change the resonance condition between to atomic states by introducing a differential light shift $\delta_\nu = U_\uparrow - U_\downarrow$. It depends on the average light shift U

$$\delta = (\eta_s + \eta_\nu \epsilon)\ U/h. \tag{2.17}$$

and the polarization of the light field described the ellipticity $\epsilon = (I_{\sigma^+} - I_{\sigma^-}) / (I_{\sigma^+} + I_{\sigma^-})$. Here h denotes the Planck constant. We can again distinguish between the scalar and the vectorial component of the differential light shift. The former is polarization-independent and accounted for by the constant η_s [54], the latter is proportional to the ellipticity ϵ and has been modelled by [39]. We have recently demonstrated that the vectorial light shift can be used to measure the depth of a dipole potential [70]. The differential light shift caused by the vector polarizability of the ground state in conjunction with the ellipticity of the polarization of the light field can be interpreted as a fictitious magnetic field [68].

2.3.1 A three dimensional dipole trap

In the following I will describe the beam configuration of our dipole trap. I will also outline how the vectorial light shift gives rise to a state dependent trapping potential for our qubit system. More details can be found in the theses of my colleagues [5, 31].

The vertical dipole trap We confine our atoms in a bichromatic dipole trap. Vertically the atoms are trapped in a standing wave formed by a beam with λ_V =1 064 nm. The lower surface of the objective lens serves as the mirror of a cat-eye configuration, where the beam is focused to a waist of w =50 µm.

The objective lens that we use to take fluorescence images of the atoms is glued inside the vacuum chamber. It has a working distance of 150 µm [8].

The surface of this objective lens defines the coordinate system used to describe the experiment. Throughout this thesis "horizontal" will mean parallel to its surface, "vertical" perpendicular to it and the origin is a point close to the center of the front focal plane of the objective. It has a coating that has a very large angle of total reflectance at 852 nm making a high numerical aperture of 0.92 possible [8]. Its surface also acts as a mirror for light at 1064nm that is used to create a one dimensional dipole trap along the vertical direction.

The large reflectivity is necessary to avoid damage to the surface because the beam has up to 4 W and is in a cat-eye-configuration with a focal waist of 50 µm. The light is provided by a Mephisto MOPA laser system that is capable of delivering up to 25 W of laser power. We use a fibre to improve the mode quality and to increase the pointing stability.

We observed a shift in the VDT position during the experimental sequence. I installed an optical isolation stage with a polarizing beam splitter and two waveplates that prevent the back-reflected light from heating the fibre's facet in the out coupler.

In a future upgrade of the experimental setup I propose to include mirror mounts that use piezo-driven set screws [17] to enable automatic reoptimization of the fiber coupling. An abundance of light is available from the laser. This allows us to add another beam at 1 064 nm forming a second, larger vertical dipole trap. We could use one as a dimple to ensure a tight initial loading of the atom cloud and to prevent vertical hopping. The second can provide homogeneous conditions for resolved sideband-cooling and coherent manipulation.

The horizontal trap Horizontally the atoms are trapped in a spin dependent, simple cubic optical lattice with a lattice constant of $\lambda/\sqrt{2}$=nm. The lattice is formed by three beams aligned in a T configuration as shown in figure 2.11. This setup was designed as platform to realize two dimensional quantum walks [6] and studied in more detail in the work of Stephan Brakhane [37].

The wavelength is chosen to be 859.9 nm. At this "magic" wavelength atoms that are being prepared in $|\uparrow\rangle = |F = 4, m_F = 4\rangle$ are sensitive only to the σ^+-component of the light (See section 2.3). The potential seen by atoms in $|\downarrow\rangle = |F = 3, m_F = 3\rangle$ is given by $U_\downarrow = c_0\,(7/8\,U_{\sigma^-} + 7/8\,U_{\sigma^+})$.

By controlling both the phase and the intensity of both polarization states of the two counter propagating beams we have recently realized state dependent transport and atom interferometry [31]. The polarization synthesizer and my contribution to its digital control will be described in section 2.4.

2.3.2 Laser system

We use three types of lasers to generate the light needed to trap and manipulate the cesium atoms. All lasers except the one driving our vertical dipole trap are located on a separate optical table. The light is transferred using polarization maintaining optical fibers [18].

The light needed to create our state dependent trapping potential is provided by a titanium sapphire (TiSa) laser [19]. Since its invention in 1986 [71, 72] TiSa lasers have all but replaced Dye laser as work horses for optics laboratories. We use it as tunable continuous wave laser delivering up to 6 W and it consists of an epinoumous crystal located in a ring resonator that is pumped with up to 25 W of light with 512 nm from a diode-pumped solid state (DPSS) laser (Coherent: Millennia eV25). The TiSa crystal has a very broad gain bandwidth and is able to operate between 650 nm and 1 100 nm. We operate it at 866 nm where the

[17] Pico N570 from Physik Instrumente
[18] Thorlabs, PM780-HP
[19] Sirah Matisse CS

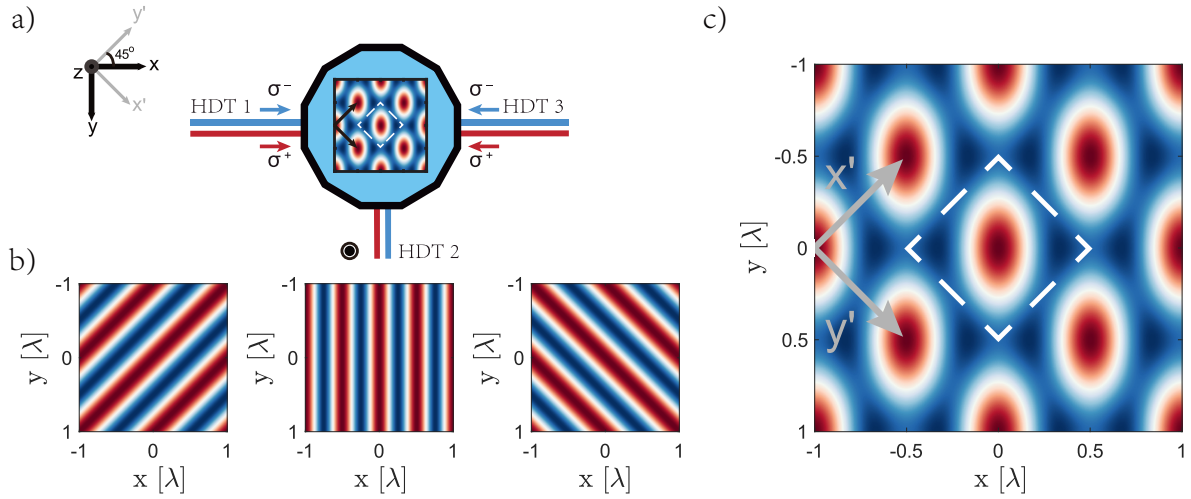

Figure 2.11: The two dimensional horizontal lattice (a) Configuration of beams. Three beams aligned in a T configuration form a two dimensional simple cubic lattice of elliptic intensity maxima. The white square indicates the Wigner–Seitz cell. (b) Standing wave pattern generated by two beams each. From left to right one beam is turned off in ascending order. The pattern between the orthogonal beams are aligned with the dashed basis vectors. This illustrates why controlling the phase of the counter propagating beams enables two dimensional transport. This is made state dependent by controlling the orthogonal circular components individually using the polarization synthesizer. (c) Three beam interference pattern.

output power is still within 10% of its peak at 780 nm. The laser is locked to a temperature stabilized reference cavity providing it with excellent stability. Its spectral properties have been studied in a master thesis [73]. The devices at hand are designed with fully digital feedback, which allows us to remotely control, reoptimize and monitor the laser performance. The output intensity is actively stabilized using a Pockels cell in combination with a Glan-laser polarizer and the light is split into three arms that form the horizontal dipole trap.

The light used to drive the cooling transition of the MOT is provided by a second TiSa-Laser that is locked to a spectroscopy setup.

The light driving the repumper transition and the state preparation is provided by diode lasers in a external feedback configuration. Interference filters are used as wavelength selective elements. The design was invented by Baillard et. al. [74] and our realization is described in [61]. The reliability is further increased by a custom electronic board that enables current feedback and features an LC-low pass filter and diodes for surge protection [5]. The design proved to be very reliable. During my time in Bonn not a single laser diode had to be replaced.

I built diode lasers operating at 895 nm to drive Raman transitions through the D_1-line of cesium. Their performance is very similar to the aforementioned lasers operating at 852 nm. I attribute this to the comparable quality of both the laser diodes and the interference filters. More details on these lasers are given in section 2.5.

2.4 Digital intensity control at the shot noise level

We trap neutral cesium atoms in a spin-dependent optical lattice. Coherent manipulation of atoms is possible when both the motional and the internal degree of freedom are well controlled. On the one

hand, the lattice potential must exhibit low fluctuations in-depth and position to prevent heating and dephasing of the atoms. On the other hand, experiments like measuring the Wigner function, which I will describe 4 require us to change both the position and the depth of the lattice potential dynamically. Sudden displacements of the position can be realized using additive feedforward control. Changing the lattice depth by more than one order of magnitude requires us to compensate for the non-linearity of the acousto-optical modulators, that we use to control the beams.
Using digital electronics to stabilize and control the intensity and phase of laser beams offers possibilities such as feedforward control, linearization of the system response, freezing and restarting (sample- and hold). The main drawbacks are the reduced feedback bandwidth, which is limited by the dead time of the input stage and the input noise that limits the signal to noise (SNR) and thus the noise floor of the stabilization circuit.
In the following, I will describe the polarization synthesizer that generates arbitrary states of polarization. Then I will describe the custom amplified different photodiodes that are used to realize intensity control at the shot-noise limit. The last part of this section is dedicated to the improvements I made to the digital control software and their impact on applications, such as measuring the Wigner function.

2.4.1 Polarization synthesizer

The state-dependent lattice is formed by a pair of counter-propagating beams crossed perpendicularly by a third beam. The quantization axis of the system is aligned with the optical axis of the counter-propagating beams. This means that their circular polarization components act as σ^+ and σ^- components on the atoms. We generate arbitrary states of polarization using two polarization synthesizers. They allow independent control over the amplitude and the phase of both polarization components. We can thus synthesize any point on the Poincaré sphere [75]. The beam is split into two orthogonally polarized component that can be individually controlled using an acousto-optical modulator in single pass configuration as shown in figure 2.12. The beams are recombined using wollaston prism, and their spatial modes are filtered using an optical fiber. Custom non-polarizing pickup-plates (Altechna) are used to collect the light needed for intensity and phase feedback. The two polarization components are split using wollaston prism. Two pairs of waveplates are used to match the polarization of the beam to the axes of the two wollaston prism to reduce the cross-talk between the feedback loops. A third one makes the beam circular again.

The polarization synthesizer was first demonstrated in our group's one-dimensional lattice experiment and successfully used to perform 20-step quantum walks [29] and state-dependent transport at the quantum speed limit [76]. A detailed analysis of its properties can be found in [61, 75]. In our two-dimensional setup, we have twice the number of feedback loops and the spatial overlap between the counter-propagating beams as an additional source of cross-talk. We reach extinction ratios (between the locks) below 10^{-5} and up to 10^{-6}, by means of careful alignment, stable temperatures and switching from double- to single-pass operations of the AOMs. A detailed description can be found in the thesis of Gautam Ramola [31].
Using AOMs in single-pass configuration causes temperature-induced pointing instabilities. We installed an upstream analog, intensity feedback with a Pockels cell and a Glan-laser polarizer [77]. It is located between the laser and the optics distributing the light to the three arms of the lattice as shown in figure 2.12 and allows us to run the AOMs at nearly constant Rf-power corresponding to about 90% of their peak efficiency.

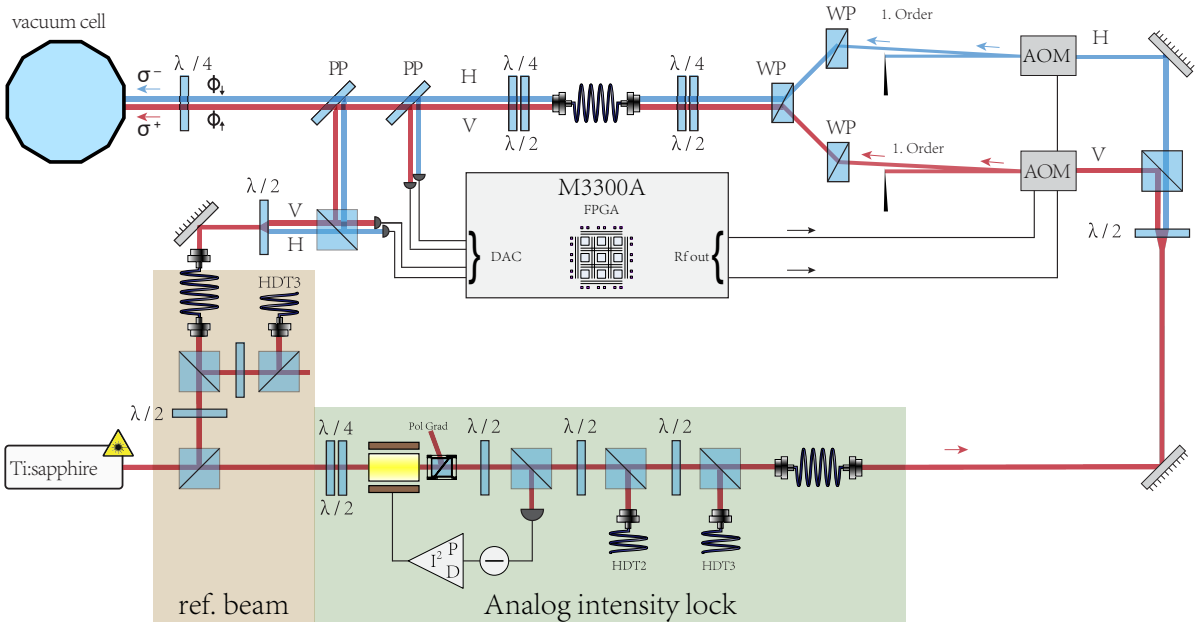

Figure 2.12: Intensity and phase control of one lattice beam. The beam is split into two orthogonal linear polarization components that are controlled individually using acousto-optical modulators (AOMs) and subsequently recombined. A fiber is used for spatial mode filtering, and digital feedback controls both their phase (relative to a reference beam) and their amplitude. This way, we can synthesize any polarization state on the Poincaré sphere. The drawing also shows how we pick up two reference beams of equal optical length to enable phase feedback. We use the AOMs in single-pass configuration to avoid crosstalk between the counter-propagating beams. To avoid thermal pointing instability, we aim to use the AOMs at nearly constant efficiency, hence applied Rf power. This is achieved by an analog intensity lock that controls the intensity send towards the three horizontal lattice beams. Light from the secondary port of the analog lock is reused to create the optical polarization gradient (see chapter 3). The beat signal in the phase lock loop is at 80 MHz. I omitted to show the combination of (limiting) amplifiers and mixers used to convert the signal to 10 MHz. More details of the analog lock and the phase-feedback can be found in [31].

2.4.2 Digital intensity control at the shot noise level

Five intensity and four phase feedback loops are used to control the optical lattice's depth and position.

We employ three arbitrary waveform generator (AWG) and digitizer combinations [20], that have eight analog input channels with a sampling rate of 100 MSa s^{-1} and four Rf-output channels with 500 MSa s^{-1}. PXIe connections that provide a common bus between modules and two I/O ports for triggers enable further integration. Each module contains a 16bit field programmable gate array (FPGA)[21] clocked at 100 MSa. The proprietary firmware of the module programs one section on the FPGA chip. This section contains, among other things, four dual-channel AWGs. The remaining area is freely programmable. Our master student Maximilian Werninghaus implemented and characterized intensity and phase-feedback control for the lattice [78].

The input noise of the M3300A modules reduces the effective number of bits (ENOB) of the digitizer from the nominal 16bit to 10.4bit, which corresponds to ≈1350 levels, a signal to noise ratio of $SNR = P_S/P_\epsilon 1.5 \cdot 2^{2ENOB} = 2.8 \cdot 10^6$ and a relative intensity noise of $RIN = 1/\sqrt{SNR} = 0.6 \times 10^{-3}$

[20] Keysight M3300A
[21] Xilinx, Kintex-7 410T

Intensity noise heats the atoms. The corresponding heating rate is, however smaller than 1×10^{-2} quanta s^{-1} and thus negligible [31]. Intensity noise causes fluctuations of the polarization ellipticity $\epsilon = (I_R - I_L)/(I_R + I_L)$ because both circular components are stabilized independently. This leads to a time-varying differential light shift that causes dephasing [57]. The variance of the ellipticity σ_ϵ^2 can be computed using

$$\sigma_\epsilon^2 = \frac{R_R^2 + R_L^2}{4} \tag{2.18}$$

where $R_{R/L}$ is the relative intensity noise of the right-/left handed circular polarization [75]. Using $\delta = (\eta_s + \eta_\nu \epsilon)\ U/h$ (see equation 2.17) we can therefore estimate the phase variance

$$\Delta\Phi^2(\tau) = \frac{\tau^2 \eta_\nu'^2 U_0^2}{\hbar^2} \int_0^\infty d\omega\ sinc^2\left(\frac{\omega\tau}{2}\right) S_\epsilon(\omega) \tag{2.19}$$

The equation 2.19 corresponds to equation 23 in [57], except for a factor of 2 that accounts for using twice the number of polarization synthesized beams. I measured the input noise of the M3300A digitizer using an internal data acquisition channel. In figure 2.13(a) we see the drift of the bias voltage and figure 2.13(b) shows the spectral The results are shown in The input noise limits the coherence time to 2 ms if the measurement duration exceeds 30 min. The coherence time can be improved by using a fast, low-noise difference amplifier that subtracts a reference voltage and amplifies the error signal before digitization. This is challenging because low noise, high bandwidth and large amplification are required.

Amplified difference photodiode We have developed a fast, low-noise, amplified difference photodiode, which comprises two stages of amplification [79]. I improved the original design from Muhib Omar [79] by adding the monitoring output for the first stage, improving the resistance to EMI and characterizing the input for the external reference voltage[22]
A simple large area photo diode is used[23], that offers twice the responsivity of the PDA10EC[24] that we used before. The bias voltage is changed from 0 V to −9 V to increase the dynamic range. It is derived from a high stable voltage reference [25] to ensure long term stability. The first stage of amplification contains a transimpendance amplifier[26] with a gain of 14 kV A^{-1} and a bandwidth of 3.6 MHz. The second stage comprises a difference amplifier with a gain of 20. A jumper is used to choose between an internal reference voltage that is generated using a (low-pass filtered) potentiometer and an external reference that is connected using a unity gain, differential amplifier[27]. The modulation bandwidth of the external input is 1.1 MHz and the modulation bandwidth of both stages combined 950 MHz. More details on the electronic setup can be found in appendix B.

I have characterized the voltage noise of three different arbitrary waveform generators and the internal reference voltage. The result is shown in 2.13. The 33522B from Keysight is slower (30 MHz but more stable than the AFG31202 (100 MHz). The low-frequency drift of the 33522B is 20 times smaller than the drift of the bias voltage of the digitizer of the M3300A module, and the upper bound to the coherence time improves from 2 ms to 40 ms. We can even reach the shot-noise limit if the optical power impinging on the photodiode is at least 1 mW[28].

[22] Mr. Kalb from our electronics workshop designed the updated PCB layout.
[23] Vishay, BPW34 S(λ = 852nm) = 0.6 A W^{-1}
[24] Thorlabs, PDA10EC S=(λ) = 852nm = 0.3 A W^{-1}
[25] Analog Devices, AD587
[26] Analog Devices, AD8065
[27] Analog Devices, AMP03
[28] Intensity noise is fundamentally limited by the quantized nature of photons, which gives rise to shot-noise. The arrival in a

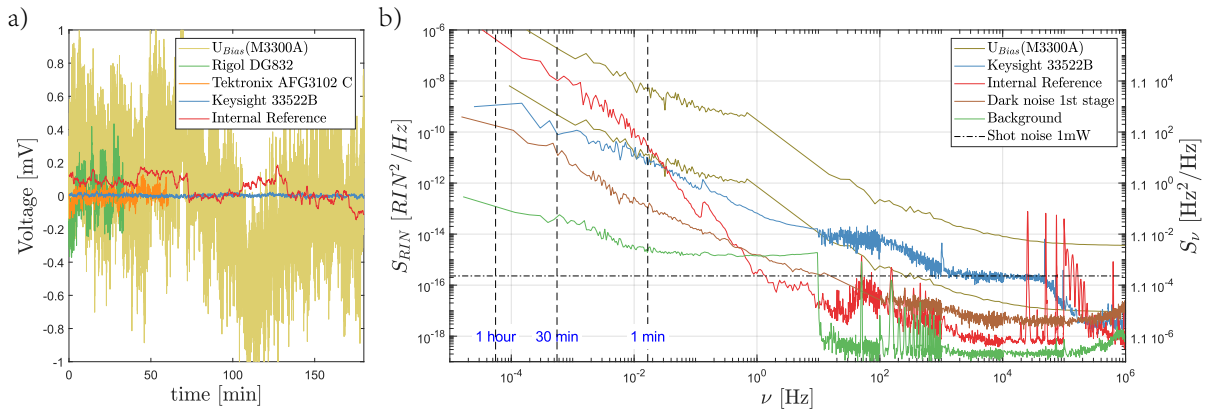

Figure 2.13: Voltage noise of the reference voltage. a) Drift of reference voltage. b) Relative intensity noise (RIN) power spectral density and the corresponding frequency noise PSD. The input noise of the M3300A (U_{Bias}) is shown with and without an amplification of 20. Without amplification the coherence time is limited to 2 ms. The other components are so stable that the this limit improves 20-fold, after amplification.

2.4.3 Linearization of system response and feed forward control

So far, we have focused on the limitations of digital control and ways to overcome them. Now I will showcase the versatility of the FPGAs parallel computing power with features we have implemented in our laboratory.

Linearization of the system response We plan to measure the Wigner function of trapped atoms, which requires us to change the depth of the lattice during the interrogation time of a Ramsey interferometer (See chapter 4). This requires stable operation of the intensity feedback over a sufficiently large dynamic range.

The polarization synthesizer uses AOMs to control both the intensity and the phase of the lattice beams. The diffraction efficiency depends non-linearly on the Amplitude of the applied rf signal. Since the gain of the feedback is proportional to the gradient of the efficiency curve, we can reduce the total gain until the system is stable, even at the steepest point of the intended operating range. Alternatively, we can linearize the system response with lookup tables (LUTs). The response curve is measured and inverted. The inverse function can be interpolated piecewise, and the coefficients are stored in memory. This set of data is called a lookup table. The FPGA applies the inverse function to the output of the digital PI controller.
I have linearized the system response as shown in figure 2.14(a). The dynamical range of the intensity lock now covers more than one order of magnitude from 2 mW to 20 mW per lattice arm, which is sufficient to measure the Wigner function.

Additive feed forward control Measuring the Wigner function also requires sudden displacements of the lattice position.

stream of light of individual photons is uncorrelated and can be modelled as a Poissonian process. This is in contrast to a current comprised of electrons. The repulsive Coulomb interaction leads to correlation and allows to measure currents below the shot-noise limit. Squeezed states of light are an exception [80], which can exhibit amplitude (hence intensity) noise below the standard quantum limit at the expense of greater phase uncertainty. Various techniques to generate squeezed states of light exists. For example driving laser diodes with sub-shot-noise currents [81] or intracavity frequency doubling [82].

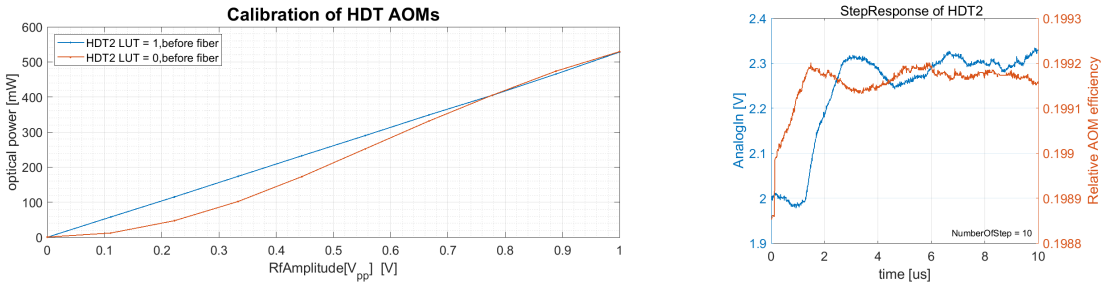

Figure 2.14: What we see is on the left is that the linearization of the AOM response works. On the right, we see a step response recorded using the internal data acquisition of the M3300A. This can be used to tune the feedback parameters automatically. Recording the traces of both the input and the output is helpful for debugging.

The bandwidth of the digital phase lock loops that control the lattice position is, however, limited to 230 kHz [78]. Feedforward control, however, makes it possible to change the position within 300 ns as shown in figure 2.15. This which corresponds to a modulation bandwidth of 3.3 MHz. The limitation is the speed of sound in the AOM-crystals and the finite size of the beams. This is beyond the bandwidth of analog PI^{2}D-controllers[29] that reach typical bandwidths of 800 kHz [75] and up to 1.2 MHz [78].

The numerical simulation in chapter 4 predicts that changing the position within 300 ns is sufficiently fast to avoid transferring momentum to the atoms.

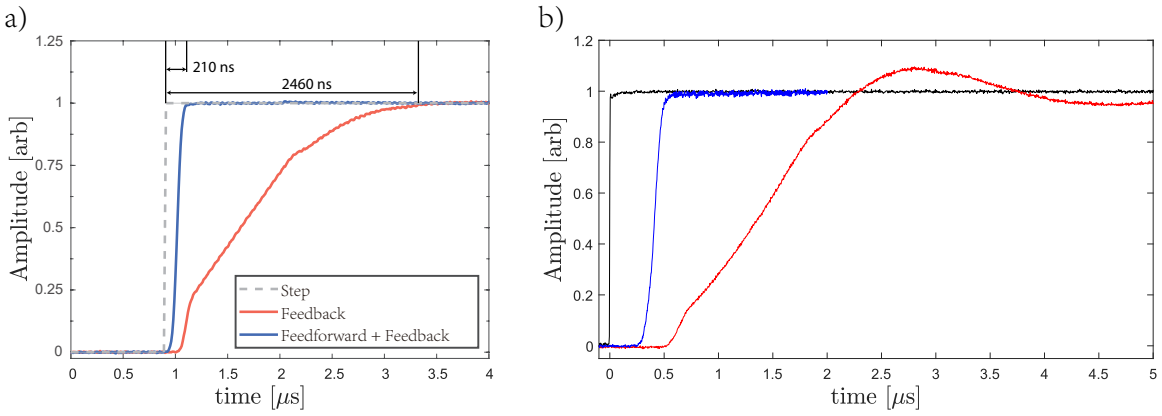

Figure 2.15: Step responses with and without additive feedforward control. Using feedforward control in conjunction with internal model control the modulation bandwidth can be increased from 230 kHz to above 3 MHz. The figures are adapted from [77, 78].

We can employ internal model control to combine feedforward and feedback control [83]. The goal is to use feedforward to rapidly modulate the system's state and feedback to compensate for external disturbances. The feedback will however compensate the action of the feedforward control unless the setpoint is changed accordingly after an appropriate time delay.

2.4.4 Summary and Outlook

Digital hardware allows the integration of multiple feedback loops in a compact device. Nevertheless, it is slower and noisier than state-of-the-art analog controllers. Here I have shown that we can overcome

[29] VescentPhotonics,D2-125

these two drawbacks. The input noise can be compensated with sufficient amplification. The modulation bandwidth can be increased using feed-forward control.

We are only beginning to unlock the full range of processing capabilities of the FPGA. The M3300A module also features internal data acquisition channels and two I/O channels for triggering. The recording of intensity step responses that I implemented may serve as an example. The setpoint of the intensity feedback is changed based on a registry entry. This triggers two of the data acquisition channels, and we record both the voltage input and the PID output as shown in figure 2.14(b). We can thus (auto) tune the feedback without additional hardware.

2.5 Resolved Raman sideband cooling

Cooling atoms into the vibrational ground state of the dipole lattice is desirable because it increases the coherence of the ensemble. Hot atoms experience smaller differential light shifts than cold ones, which leads to spin-dephasing in thermal ensembles [54]. Additionally, cooling is a requirement for the preparation of indistinguishable particles and arbitrary states of motion.
One technique to cool atoms into, or close to their motional ground state, is to create a Mott-insulator from a BEC [84]. While high filling factors and ground state occupations exceeding 99% can be achieved [85], this technique is neither feasible for small numbers of atoms nor does it preserve the atom position. The latter is necessary because we have to re-cool atoms after performing plane selection (See section 3). We use resolved sideband cooling, which is applicable even for a small number of particles and has been shown to achieve ground state occupations up to 99.9% for single ions in Paul traps [12]. In the following, I will describe both microwave and Raman sideband cooling with an emphasis on the latter. The efficiency of microwave sideband cooling in the DQSIM experiment was recently presented in the thesis of Gautam Ramola [31].

Raman laser system

For this experiment, I decided to use light close to the D1-line of cesium to drive Raman transitions. In this case we can use dichroic beam splitters to integrate the Raman beams into the existing setup and avoid losses. I built two external cavity diode lasers (ECDL) that employ interference filters to tune the wavelength. The design was first presented in [74] and refined by Carsten Robens [8].

The diodes are Fabry-Perot laser diodes with anti-reflection coating [30]. An interference filter acts as a narrow optical band-pass filter. The interference filters[31] have a peak transmittance of 98% and a width of 0.6 nm. This is thin enough to ensure single-mode operation, and the peak transmittance is large enough to avoid excessive losses. The filters have an out of band rejection of more than 100 nm to either side of the central wavelength spanning from 780 nm to 1030 nm. This ensures that laser modes at the peak of the diodes gain curve at 920 nm are sufficiently suppressed. The lasers deliver up to 60 mW of power, exceeding the specification by 20%. Their fiber coupling efficiency reaches 40% and 60% respectively. The performance is very similar to previously built lasers that run at the cesium D2-line of 852 nm.

Coherent two-photon transitions require a stable phase- and frequency relation between the two light fields. We achieve this with an optical phase lock loop (OPLL), built around a phase-frequency discriminator (PFD) with a capture range of 100 MHz. The design was originally proposed by Prevedelli et. al. [86], and has been in use in our group for over ten years [87]. The feedback bandwidth was measured by observing the in-loop beat signal. The servo bumps are separated by 1.7 MHz and have a height of −100 dBc. The feedback is remarkably stable and needs to be re locked only once every few weeks. The intensity of both lasers is controlled using AOMs in double-pass configuration. Mechanical shutters are used to provide complete extinction.

The beat signal is recorded using a fast photodiode[32]. A bias tee separates the DC and the AC components of the signal. The DC-current is monitored to tune the power of both beams and optimize the overlap of their polarization. After the narrow-band, low-noise amplifier[33], I installed a power

[30] EYP-RWE-0920-0401 0-1500-SOT02-0000
[31] Moglabs UNB894
[32] Albisopto, PQW10A-L
[33] Kuhna electronics, MKU LNA 922A

splitter to monitor the beat signal. The dynamic range of our spectrum analyzer[34] is large enough to measure side modes that are separated by an integer multiple of the free spectral range of the laser (ca. 1.1 GHz). This allows us to detect the onset of instabilities and to tune the laser current and temperature accordingly. The signal is amplified and down-converted using a mixer and a local oscillator running at 9.3 GHz. The dynamic range is therefore nearly 100 MHz. I installed an rf-isolator[35] to shield the phase locked dielectric resonator oscillator[36] from interference that would otherwise cause mode-jumps. The phase-frequency discriminator compares the down-converted beat signal with an rf-signal from an arbitrary waveform generator[37].

2.5.1 Coherent two-photon transitions

So far, we have modelled the atoms as a two-level system whose internal state can be manipulated using microwave radiation. The presence of a third (excited) state enables us to use Raman transitions as well. Two laser beams that are called Stokes- and Pump laser are overlapped. They have a common one-photon detuning $\Delta = \omega_0 - \omega_L$ from the transition to the excited state. Typically detunings are several tens of GHz up to hundreds of GHz. A compromise is to be made between a low scattering rate and sufficient interaction strength. If the beat-frequency between the fields is brought into resonance with the two-level transition, then the qubit states are coupled through a virtual level, and Raman-Rabi-oscillations are possible.

If the population of the virtual level is low, one can perform adiabatic elimination and arrives at an effective two-level system [88]. The effective Rabi frequency Ω_{eff} is given as

$$\Omega_{eff} = \frac{\bar{\Omega}_1 \bar{\Omega}_2}{2\bar{\Delta}} \tag{2.20}$$

where $\Delta_{1,2}$ are the one-photon detunings of the two lasersand $\bar{\Delta} = 1/2(\Delta_1 + \Delta_2)$ denotes the average one-photon detuning and $\bar{\Omega}_{1,2} = (\Omega_{1,2} + \Delta_{1,2})^{-0.5}$ are the generalized Rabi frequencies.

Beam configuration Until now, we have treated the manifold of excited states as a single level. This is appropriate since the one-photon detuning of Δ =200 GHz is much larger than the hyperfine splitting of the excited state $6^2P_{1/2}$. This however neglects interference between the different trajectories. The transition amplitudes through the virtual levels can be computed using the Clebsch-Gordon coefficients, and the Wigner-6-j symbols [89].

The linearity of the problem allows us to capture the coupling to all these virtual levels and the interference between the possible path in a scalar number $\chi = \chi(m_F, p_1, p_2)$ that depends on the mF-level of the $|\downarrow\rangle$ state and the two respective polarization $p_{1/2}$. This allows us to compute the Raman Rabi frequency Ω_R from the effective Rabi frequency Ω_{eff}

$$\Omega_R = \Omega_{eff}\chi(M). \tag{2.21}$$

In our case only two combinations of polarization, namely (π, σ^-) or (π, σ^+), can driven. And the selection rules limit the number of trajectories to two for both.

[34] Agilent, N9010A EXA Signal Analyzer
[35] MTC, I13
[36] Resotech, PLDRO-9200-50
[37] Moglabs, XRF421

$$\chi = \begin{cases} \sqrt{-\frac{35}{288}} & , (\sigma^+, \pi) \\ \sqrt{-\frac{42}{288}} & , (\pi, \sigma^-) \end{cases} \tag{2.22}$$

Since the coupling strengths differ by less than 10% we are free to choose either. The Raman stokes laser is aligned horizontally and propagates perpendicular to the quantization axis. It is linearly polarized in the horizontal plane (x,y); hence it induces π-transitions only. The Raman pump laser is overlapped with the vertical dipole trap. Its polarization is linear and parallel to the quantization axis. This can be decomposed into equal components of σ_+ and σ^--light. If we were to increase the one-photon detuning of the vertical Raman beam by $2\,\Delta_{HFS}$, we would drive (σ^+, π)-transitions. The repumping beam that is needed to close the cooling cycle propagates along the quantization axis.

2.5.2 Adressing motional sidebands

Coherently coupling of vibrational states

So far, we have neglected the motional degree of freedom of the atoms. We use optical traps in the tight-binding regime, where tunnelling between adjacent lattice sites can be neglected. The atomic wavefunction can be described using maximally localized Wannier states [90] that form a set of orthogonal eigenstates $\langle n|n'\rangle = 0$.

Coherent transitions between vibrational levels are possible if the orthogonality is broken by applying a shift either in momentum or real space [91]. The former is realized by the momentum transfer that occurs when a Raman photon is coherently scattered from one beam into the other. The latter is achieved by displacing the two state-dependent trapping potentials relative to each other. The coupling strength between the states n and n' is proportional to their overlap [92]

$$I_n^{n'} = \langle \uparrow, n | T_{\Delta z\,+\,\Delta k} | \downarrow, n' \rangle. \tag{2.23}$$

The overlap integral $I_n^{n'}$ is also called Franck-Condon factor, which is often used in molecular physics [93].

In the harmonic approximation a unified treatment is possible, using the general complex Lamb-Dicke Parameter [92, 94]

$$\eta := \eta_k + \mathrm{i}\eta_\mathrm{x} = \frac{\hbar \mathrm{k}_\mathrm{opt}}{2\mathrm{p}_0} + \mathrm{i}\frac{\Delta \mathrm{x}}{2\mathrm{x}_0} \tag{2.24}$$

where $x_0 = \sqrt{\hbar/2m_{Cs}\omega}$ and $p_0 = \sqrt{\hbar m_{Cs}\omega/2}$ are the spatial and momentum uncertainty of the wavefunction. In the Lamb-Dicke regime with $\eta \ll 1$, the Franck-Condon factors can be approximated as

$$I_n^{n'} = \delta_{n,n'} + \eta\left(\sqrt{n'}\delta_{n',n+1} - \sqrt{n}\delta_{n',n-1}\right) \tag{2.25}$$

where δ denotes the delta distribution. This means that the coupling to the heating transition is always stronger than the coupling to the cooling transition, hence the need to resolve them individually.

We can tune the spatial Lamb-Dicke parameter by changing the horizontal displacement between the state-dependent potentials using our polarization synthesizers. We can optimize the overlap between arbitrary vibrational levels. This has been studied for both the one-dimensional case [91] and recently in our two-dimensional lattice [31].

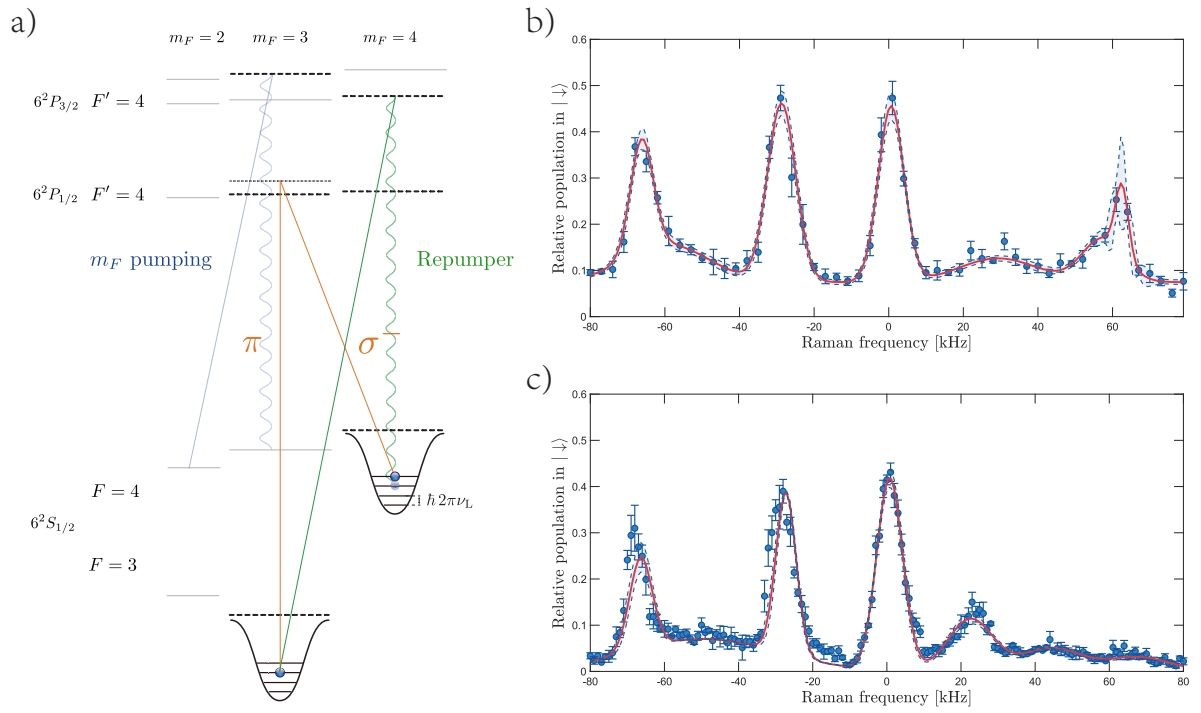

Figure 2.16: Resolved Raman sideband cooling. (a) Level scheme of the of the cooling cycle.
(b) Raman spectrum with atoms that are cooled vertically with molasses only. The Peak in the center corresponds to the carrier transition. The peaks at ±30 kHz correspond to the heating and the cooling sideband along the horizontal Raman beam. The peaks at ±75 kHz correspond to vertical sideband transitions. The ratio between their height indicates that ca. 30% of the atoms are cooled along the vertical direction.
(c) Raman spectrum with vertical sideband cooling. The ratio between the heating and the cooling sideband indicate a ground state population of 90% along the vertical direction.

Resolved sideband cooling We perform resolved sideband cooling by continuously driving coherent transitions between $|\uparrow, n\rangle$ and $|\downarrow, n-1\rangle$. Simultaneously we shine repumping light that is resonant to the $F = 3 \rightarrow F' = 4$ transition. The incoherent process of absorbing and scattering closes the cooling cycle as depicted in figure 2.16(a). In the absence of heating, all atoms will eventually condense in $|F = 4, n = 0\rangle$, which is the dark state of the cooling process. We iteratively cool the atoms along all three dimensions to reach the three-dimensional ground state. In the first iteration, we cool for 10 ms along each direction to reach equilibrium. Then we cool along each direction again for 0.5 ms to 2 ms. This is long enough to perform one to two cooling cycles but short enough to prevent heating along the transverse directions.

We employ microwave radiation to cool horizontally because of its spatial homogeneity, the tunable Lamb-Dicke parameter, and the electrical components' reliability.

We measure the population of the vibrational ground state using resolved sideband spectroscopy as shown in figure 2.16. A π-pulse is used to transfer atoms from $|\uparrow\rangle$ to $|\downarrow\rangle$ and a resonant pushout beam is used to eject atoms remaining in $|\uparrow\rangle$. The Raman spectra contain seven peaks. The red-detuned peaks correspond to heating transitions or sidebands that increase the motional quantum number. The central peak is called the carrier and it corresponds to transitions ($|\uparrow, n\rangle \rightarrow |\downarrow, n\rangle$) that preserve the vibrational level. The blue detuned peaks stem from transitions that lower the motional energy. Our beam configuration allows us to couple vibrational states vertically and along the horizontal axis with the

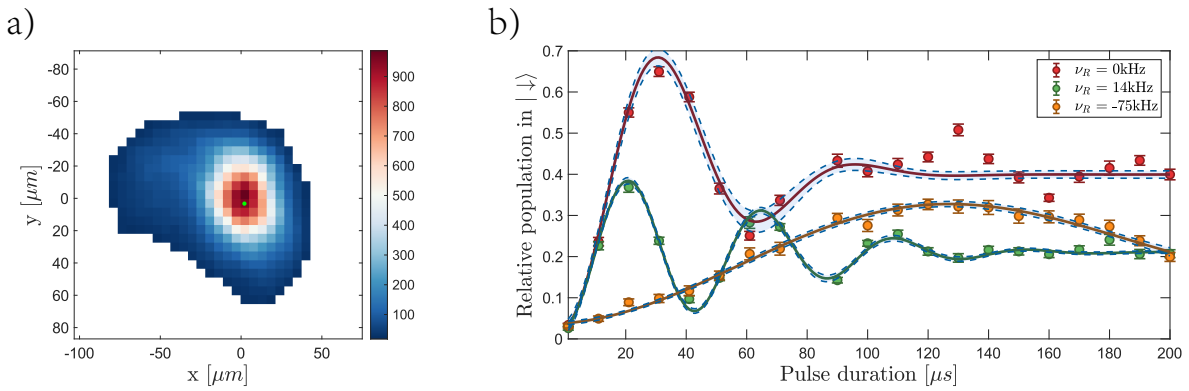

Figure 2.17: Raman Rabi oscillations are driven for different two photon detunings. a) Total number of atoms captured in each macro pixel. b) Raman Rabi oscillations at the carrier ($\nu_R = 0$ kHz), at the half width of the carrier ($\nu_R = 14$ kHz) and at the first vertical heating sideband ($\nu_R = -75$ kHz). The green dot in a) indicates the position of the oscillations shown in b).

smaller trapping frequency. We raise the vertical trapping frequency to 75 kHz to separate the first-order vertical sideband from the first two sidebands along x, which are located at ±30 kHz and ±60 kHz. In figure 2.16(b) and (c) we see a spectra before and after cooling vertically. The ground state population can be inferred from the asymmetry between the heating and cooling sidebands because atoms that are cooled into the ground state can not be cooled further. We can determine the mean excitation number $\overline{n}$ from the relative height of the cooling and heating sideband [55, 95]

$$\overline{n} = \frac{h_{hsb}}{h_{csb} - h_{hsb}}. \tag{2.26}$$

This assumes the atoms to be in thermal equilibrium and the line shape of both sidebands to be equal. If the latter is not the case, one would have to compare the area under both peaks. This, however, is difficult for us because we do not spectrally separate all transitions. This method of thermometry is insensitive to the Rabi-frequency of the carrier, and the pulse duration [55].

The ground state population n_0 can be computed from the average excitation number $\overline{n}$, using

$$n_0 = \frac{1}{1 + \overline{n}}. \tag{2.27}$$

We cool more than 95% of atoms into the ground state along both horizontal directions [31]. We can cool above 90% percent of the atoms into the vertical ground state.

We can use rate-equations to estimate the achievable ground state population. A detailed study of heating mechanism in our type of optical lattice can be found the Thesis of Carsten Robens [61]. The mean vibrational occupation number $\overline{n}$ is given as

$$\overline{n} = \frac{H_{total}}{C_{total} = H_{total}} \tag{2.28}$$

where H_{total} denotes the total heating rate and C_{total} the total cooling rate.

The intensity-noise induced heating rate is in the order of 10×10^{-6} quanta s^{-1}, which is negligible. I have verified, that we raise the trapping frequency from 30 kHz to 75 kHz adiabatically. I did not observe a significant increase in temperature even after 100 cycles of raising and lowering vertical trapping frequency between these levels.

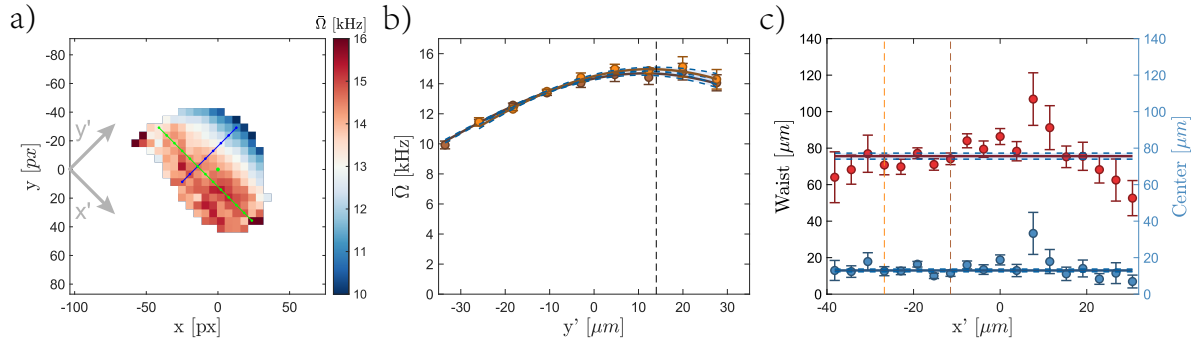

Figure 2.18: Mapping out the horizontal Raman beam. (a) We can infer the profile of the horizontal Raman beams from the distribution of the Raman-Rabi frequencies because the vertical Raman beam has a waist of 820 µm and its intensity is nearly constant across the field of view. (b) Rabi Frequency along y'. The Rabi frequency along y', which is perpendicular to the propagation direction x' is proportional to the electrical field of the horizontal Raman beam. The average waist is (75.6 ± 1.6) µm as shown in (c). The two vertical lines in c) denote the traces shown in b).

I assume that the cooling efficiency is limited by the spatial inhomogeneity of both the repumping and the Raman beams. We observe strong dephasing when driving carrier transitions, as shown in see figure 2.17. Both the Raman-Rabi frequency and the dephasing time can be extracted using a non-linear fit-model

$$P_{|\uparrow\rangle}(\tau) = \text{Off} + \frac{\text{Amp}}{2}\left[1 - \cos\left(\omega_R \tau + \varphi\right) \exp\left(-\left(\frac{\tau}{\tau_{1/2}}\right)^2 \log 2\right)\right]. \tag{2.29}$$

The model assumes the decay of the oscillation to have a Gaussian envelope. This is accurate if the Rabi frequencies have a Gaussian distribution [96]. I verified that number of visible oscillations is independent of the Raman Rabi frequency[38], which excludes external perturbations as the main source of dephasing. Also, we see partial revivals of the oscillation, which indicates that we are observing a beat signal between a finite number of frequency components with incommensurate frequencies. I assume that some fraction of the vertical Raman beam is retro-reflected from the surface of the objective lens, thus creating a vertical intensity modulation with low contrast. The vertical Raman beam and the vertical dipole trap form a superlattice with a period of $d_s = \lambda_{VDT}/(\lambda_{VDT} - \lambda_{D1})\, d_{VDT} = 1064/(1064 - 894)\, d_{VDT} = 6.3\, d_{VDT}$ =3.34 µm. Here d_{VDT} = 532 nm denotes the spacing of the vertical dipole trap.

The stability of both the phase-feedback and of the intensity is comparable to the laser system that has been used to perform Ramsey spectroscopy in our one-dimensional lattice experiment [97]. In that experiment, it takes six oscillation periods for the contrast to drop by 50%.

Cooling 90% of the atoms vertically into the ground state is enough to continue with plane selection. A detailed analysis of the heating mechanisms should be done using thinner atom ensembles. If necessary, we can avoid reflections from the objective by reversing the direction of the vertical Raman beam. This is possible but challenging given the already dense setup above the vacuum chamber.

Mapping out the Raman beam

Our high numerical aperture objective allows us to resolve the distribution of atoms spatially. We can use this to measure the shape of the Raman beams.

[38] At least if the Rabi frequency is not too slow.

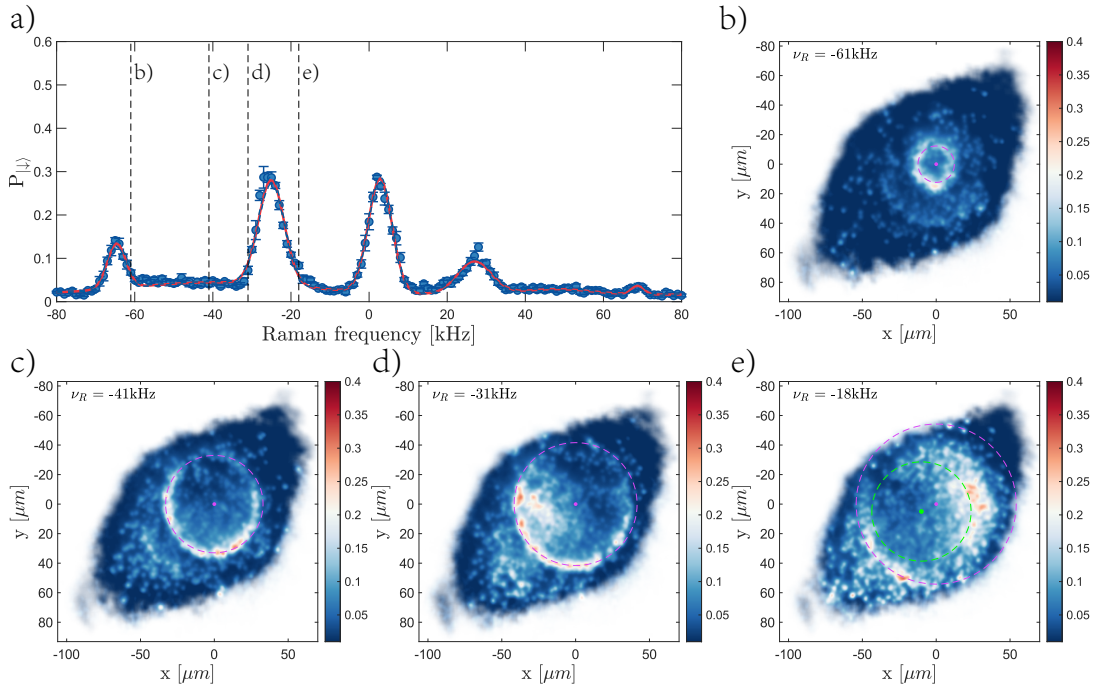

Figure 2.19: Raman spectroscopy can be used to measure the spatial distribution of vertical trapping frequencies. (a) Raman spectrum, the red detuned peak at −65 kHz correspond to the first vertical heating sideband and the peak at −25 kHz to the first heating sideband along x. (b)-(e) The position of the isolines (red dashed circles) are computed assuming a waist of 50 µm and a common origin, and they fit well.

When driving Rabi oscillations, measure the generalized Raman-Rabi frequency $\bar{\Omega}$, which depends on the Rabi frequency on resonance Ω and the detuning δ

$$\bar{\Omega} = \sqrt{\Omega^2 + \delta^2}. \tag{2.30}$$

Probing two points in the spectrum, e.g. the peak and the side-lobe of the carrier, allows us to remove local variations of the resonance frequency. I chose the red-detuned side lobe of the carrier at ≈14 kHz, to avoid driving (heating) sideband transitions.

The fluorescence images are split into a grid of macro pixels as shown in figure 2.17(a). The analysis is restricted to macro pixels where a sufficient number of atoms is loaded. We perform a non-linear fit according to the aforementioned damped-cosine model.

The distribution of Raman rabi frequencies is shown in figure 2.18(a). It is (nearly) constant along the propagation direction, and its transverse shape follows a Gaussian beam profile width a waist of 75 µm (see figure 2.18(b)). The vertical Raman beam has a beam waist of 820 µm, so it is nearly constant over the field of view. Not only can we measure the profile of the horizontal Raman beam, but we can also measure and correct its displacement of 10 µm from the center of the vertical dipole trap.

Measuring the shape of the vertical dipole trap Finally, we can assess the spatial variation of the vertical dipole trap by spatially resolving the position of the sideband. Figure 2.19 shows survival probability for different two-photon detunings. We can localize and adjust the position of the vertical dipole trap with a single shot.

While it is possible to map out the potential landscape of the vertical dipole trap, this approach

is superseded by the more accurate and elegant method of Ramsey imaging that we have recently demonstrated [70].

Discussion and outlook I have demonstrated that we can utilize light close to the D_1-line of cesium to drive Raman transitions and to perform resolved sideband cooling to achieve a vertical ground state population of 90%. The cooling efficiency is limited by spatial inhomogeneity; hence we can expect further improvements when cooling thin ensembles of atoms. Following the discussion in [61] to estimate the heating and cooling rates, it should be possible to cool up to 99% of the atoms vertically into the ground state. In addition, I have shown how we can use Rabi-Oscillation and sideband spectroscopy to map and align both the horizontal Raman beam and the vertical dipole trap.

CHAPTER 3

Plane selection with an optical polarization gradient

Quantum simulators require indistinguishable particles that can interfere with each other [4]. Preparing atoms in only one layer orthogonal to the imaging axis is a common challenge for experiments that study the behavior of two dimensional ensembles [61, 98–107]. Several techniques have been developed to realize narrow position distributions along the imaging axis . A common technique is to create a position dependent Zeeman shift by applying a magnetic field gradient. It is then possible to spectroscopically address thin volumes around the isosurfaces of the magnetic field. This scheme has been realized for most alkali elements such as ^{133}Cs [98], ^{87}Rb [99, 100] , ^{40}K [101, 102] and ^{6}Li [103]. In alternative schemes the atoms are confined in antinodes of repulsive potentials [61, 104], loaded into accordion lattices with variable lattice spacing [105, 106] or they employ repulsive evanescent fields [107].

I will describe a novel way to prepare ^{133}Cs atoms in a single vertical layer of our three dimensional dipole trap. Reducing the vertical extend of the atomic cloud improves the efficiency of resolved sideband cooling and coherence times since the remaining atoms will be exposed to a more homogeneous environment. This will also allow us to utilize the full numerical aperture (NA = 0.92) of our imaging system. The corresponding depth of focus is 0.2 µm. Currently we are imaging thick atomic ensembles and use a reduced numerical aperture of 0.3 to achieve a depth of focus of 4.5 µm.

The experiment at hand was originally designed to employ a gradient of Zeeman shifts for plane selection [5]. This is however no longer possible, since there is an unstable short circuit in the gradient coils. In the following I will describe an alternative and novel technique that employs a gradient of polarization to induce position dependent AC Stark shifts. This method is much faster and less heat is dissipated.

This chapter is split in three parts. First I will present the concept in section 3.1 and the optical alignmenent in section 3.2. The second part covers the experimental results. I show how microwave spectroscopy is used to measure the vertical distribution of atoms in section 3.3 and a proof of concept measurement showing volume selection is presented in 3.4. The last part entails a discussion whether the system is stable enough to achieve single plane resolution in 3.5. I also discuss how the finite dephasing time T_2 limits the spectral resolution of addressing pulses and what gradient is needed to address single planes. This chapter concludes with an outlook on vertical resolved sideband cooling with microwave radiation and resolving the vertical position of atoms optically in section 3.6.

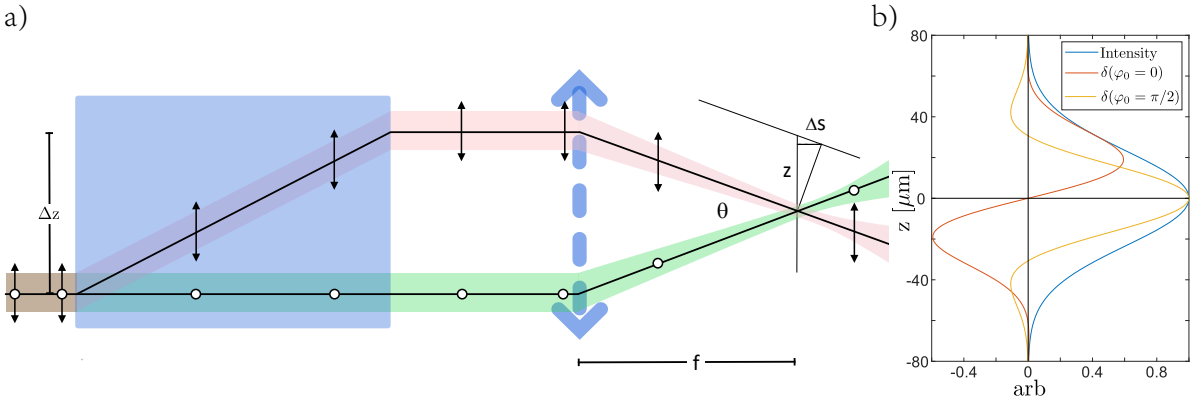

Figure 3.1: Sketch of the beam. In (a) we see how the parallel beams that are vertically and horizontally polarized are recombined using a lens. Even though the beams do not visibly interfere, the differential phase between the beams gives rise to sinusoidal modulation of the ellipticity along the vertical direction. In (b) we see the light shift δ. The polarization gradient in the center (z=0) depends on the total phase difference ϕ_0 between both beams. It is steepest if ϕ_0 is an integer multiple of π.

3.1 Concept

We generate a position dependent AC stark shift by shining two beams with orthogonal linear polarization onto the atom cloud. The beam configuration resembles Young's double slit experiment, where two beams interfere under a small angle, creating an interference pattern orthogonal to the direction of propagation and parallel to the axis of the vertical dipole trap. The vertical dipole trap is formed by a beam that is retro reflected from the surface of the objective lens. The position dependent AC stark shift modulates the atomic resonance frequency along the vertical direction. Plane selection can be achieved with a π-pulse that flips the spins in the target plane. Afterwards all other atoms are removed.

A calcite displacer[1] is used to create two copropagating linearly polarized beams which are focussed using lens with f =200 mm as shown in figure 3.1. Calcite is an ideal material because it combines high polarization purity and low wavefront distortion. Linear polarization of light can be decomposed into two orthogonal circular components. Therefore the light field can be described as the sum of two interference patterns of circularly polarized light that are equal, except for their opposite sign.
The beam configuration also resembles the well-known lin-perp-lin configuration used in polarization gradient cooling [46] and differs only by the relative angle between the beams. The ellipticity of the resulting light field is modulated sinusoidally along the vertical axis which is perpendicular to the optical axis of the beams.

The external field changes the resonance condition between the atomic states $|\uparrow\rangle$ and $|\downarrow\rangle$ causing a differential light shift $\delta_\nu = (U_\uparrow - U_\downarrow)/h$. It depends on the average light shift U

$$\delta = (\eta_s + \eta_\nu \epsilon)\ U/(2\pi\hbar). \tag{3.1}$$

and the polarization of the light field described by the ellipticity $\epsilon = (I_{\sigma^+} - I_{\sigma^-})\ /\ (I_{\sigma^+} + I_{\sigma^-})$. Here $\hbar$ denotes the reduced Planck constant. We can distinguish between the scalar and the vectorial component of the differential light shift. The former is polarization independent and accounted for by the constant η_s [54], the latter is proportional to the constant η_ν and to the ellipticity ϵ. It has been modeled by Steffen et.

[1] Thorlabs BD27

al. [39].

So far we have assumed the beams to be parallel to the quantization axis in which case we can equate the helicity of the polarization with the angular momentum transferred by the photons. The angular momenta are computed in the coordinate system defined by the quantization axis. For non-vanishing angles between the optical axis of the beams and the quantization axis the ellipticity ϵ has to be computed in the coordinate system of the latter, for equation 3.1 to remain valid. In the DQSIM experiment we align the magnetic guiding field that fixes the quantization axis along the counter-propagating beams of the horizontal optical lattice. For the polarization gradient beams I chose to use the adjacent vacuum window that is at an angle of Θ =30°. The horizontally polarized beam therefore can no longer be decomposed into a σ^+- and a σ^--component but contains π-polarized light as well. This reduces the vectorial component of the differential light shift by $1 - \cos(30°)^2$ =25%. This is small enough to justify not rotating the quantization axis [2].

In the following I compute and discuss an explicit expression for the differential light shift. For simplicity we assume a wavelength of 866 nm and ignore the scalar component of the differential light which is three orders of magnitude smaller than the vectorial one. This wavelength induces a strong vectorial differential light shift because it lies between the two transitions that form the D-line doublet of cesium. The vectorial light shift at 866 nm reads

$$\begin{pmatrix} U_\uparrow \\ U_\downarrow \end{pmatrix} = c_0 \begin{pmatrix} 1 & 0 & 1/2 \\ 1/8 & 7/8 & 1/2 \end{pmatrix} \begin{pmatrix} I_{\sigma^+} \\ I_{\sigma^-} \\ I_\pi \end{pmatrix} \quad \text{with} \quad c_0 = -k_B \times 2.717\text{pK}/(W/m^2) \tag{3.2}$$

The differential light shift $\delta = \frac{1}{h}(U_\uparrow - U_\downarrow)$ depends on the differential phase φ between both beams and on the angle Θ to the quantization axis

$$\delta = \frac{7c_0}{8h}(I_{\sigma^+} - I_{\sigma^-}) = \frac{1}{2} c\epsilon_0 E_H E_V . \sin(\varphi)\cos(\Theta) \tag{3.3}$$

The differential phase φ can be calculated using geometric optics. It depends linearly on the vertical position z

$$\varphi = \varphi_0 + 2\pi\frac{\Delta z}{f} z \approx \varphi_0 + 2\pi\frac{z}{61\mu m}. \tag{3.4}$$

where Δz denotes the displacement caused by the calcite and f is the focal length of the collimating lens. The two beams form an imbalanced Mach-Zehnder interferometer. The global phase φ_0 depends on the wavelength of the laser and on the angle α under which the beam enters the calcite displacer. This can be exploited to tune it to 0 or π. In this case the atoms at the center of the focal plane will experience no differential light shift and their resonance frequency remains unshifted as can be seen in figure 3.1. The adjacent zero-crossings are at ±31 µm which corresponds to a vertical capture range of nearly ±30 lattice sites.

Isosurfaces and capture range To achieve plane selection, the isosurfaces of differential light shift need to be flat across the field of view, which covers a circle with a radius of approximately 50 µm.

Using microwave spectroscopy we address surfaces of constant light shift or isosurfaces. The finite Rabi frequency of the addressing pulse leads to power broadening of the spectral response which translates

[2] When rotating the quantization axis, the settling time of the magnetic field must be small in comparison to the spin-relaxation time T_1. In our case the T_1-time is about 200 ms and 2.5% of the atoms would decay from $|\uparrow\rangle$ to $|\downarrow\rangle$ during the settling time of about 10 ms.

into addressing a (thin) volume around the isosurface. This volume is further broadened by instabilities of the light field that can arise e.g. from drifts of the laser frequency or pointing instabilities.

Fourier optics allows us to compute the light field taking into account clipping, beam imbalance and the rotation relative to the quantization axis. Even though Fourier optics is a scalar theory we can use it to study polarization effects by propagating both linear components individually.

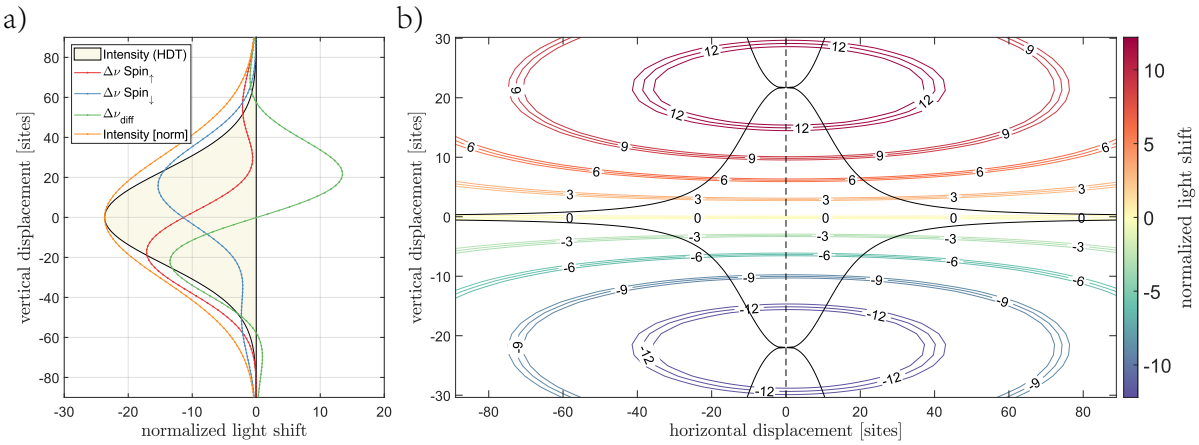

Figure 3.2: The light shifts in the focal plane of the beams forming the polarization gradient are computed. The light shifts are normalized to the light shift between the planes in the center. The vertical and horizontal displacements are given in units of the horizontal and vertical lattice constants which are $1064/2$ nm and $866/\sqrt{2}$ nm respectively. (a) The light shifts along the vertical axis in focal plane (see the black dashed line in (b)). The envelope of the beams (orange) and of the horizontal dipole trap (HDT) are shown. The red and the blue solid line show the light shifts seen by the two spin states. Together they give rise to a nearly linear gradient of differential light shifts in the center of the trap (green solid line). (b) The distribution of differential light shifts in the focal plane. The isosurface of vanishing light shifts is perfectly flat. Each isoline is accompanied by two lines that are displaced by ±20% of a site in the center. The solid black lines indicate the horizontal capture range. They mark the position, where the detuning has changed by 20% of the splitting at the origin. The dashed black line indicates the position of the vertical dipole trap.

Figure 3.2(b) shows the light field in the focal plane. The isosurface of vanishing light shifts is flat which leads to an infinite horizontal capture range. This is in contrast to the isosurfaces of Zeeman shifts created by a quadrupole field which are always elliptical [98].

The beam profile is made elliptic in order to reduce the curvature of the other isosurfaces. The ratio of 1:3 is chosen as a compromise between homogeneity and power efficiency. An optical power of 100 mW is needed to realize a gradient of detuning of 49 kHz site^{-1}. This corresponds to an artificial magnetic field gradient of 376 G cm^{-1}. For comparison I note that our gradient coils are designed to generate a magnetic field gradient of 300 mG cm^{-1} when driven with 32 A and generating 1.2 kW of heat [5].

The isolines in figure 3.2(b) are plotted in triples indicating a deviation of ±20% of a lattice site in the center. We can infer the horizontal capture range of e.g. the isolines for ±3 vertical sites to be 35 horizontal sites or 21 µm, which is larger than the horizontal extend of the atom cloud.
The change of the light field along the propagation direction is not shown. The two beams are elliptical and the Rayleigh length corresponding the fast axis is 4.1 mm, which means that we can consider their fields to be nearly constant within 100 µm before and behind the focal plane. The dominating effect will be a symmetric splitting of their centers of the beams. The waist of the combined light field will increase at a rate of 0.7 µm per 100 µm, hence, we expect the gradient to become slightly shallower.

3.2 Optical setup and alignment

Now I will describe how the polarization gradient setup is designed and how to align both the cage system and the beams relative to the atoms.

I have chosen to use light at the same wavelength of 866 nm as the state dependent lattice, because we can „recycle“ light from our lattice beams. This is possible because all coherent manipulations are performed within an optical potential that is ten times shallower than the trap depth used to image the atoms.
The remaining light is available from the secondary port of the calcite polarizer behind the Pockels cell in the intensity feedback loop (see figure 2.12). This is more than 1.5 W. A fraction of this is sent through an AOM in double pass configuration that is used for intensity control. The interference pattern between the polarization gradient beams and the dipole trap oscillates with 80 MHz, which is beyond the response time of the atoms.
Currently optical powers up to 100 mW are available, which corresponds to a gradient of 49 kHz site^{-1}. This can be increased to more than 500 mW by sending more light through the AOM. The Pockels cell, the AOM setup and the experimental table are connected using polarization maintaining optical fibers.

3.2.1 Optical system design

The optical setup on the experimental table is sketched in figure 3.3. The optical elements are mounted in a cage system to ensure stability.

The cage system The optical components are mounted in a rigid cage system atop a motorized five axis stage[3]. The distance between the fiber tip and the atom cloud is ca. 400 mm. It is therefore critical to make the beam as stable as possible, since the aim is to select atoms that are located within a fraction of a lattice constant of 512 nm.
A polarizer [4] is used to purify the polarization and a pick-up plate[5] to monitor the intensity. A $\lambda/2$ plate is used to rotate the polarization to 45°. A cylindrical telescope (f_1 = 75mm, f_2 = 25mm) shrinks the beam horizontally. A calcite polarizer[6] splits the beam into two orthogonal components, that are seperated by 2.8 mm and finally a lens[7] focuses them onto the atom cloud. The focusing lens is mounted on an x-y translation stage[8] to align it to the center of the two co-propagating beams leaving the displacer.

To minimize clipping the center or optical axis of the two co-propagating beams must coincide with the center of the calcite displacer. The beam must enter the calcite half its displacement below its center, which is achieved with a custom adapter for the kinematic holder of the fiber coupler[9].

[3] Newport, Picomoter 8742
[4] Codixx colorPol IR 1100 BC4
[5] Altechna, custom with a reflectivity of 6% for both s- and p
[6] Thorlabs BD27
[7] Thorlabs AC254-200-B, f = 200mm
[8] Thorlabs CXY1
[9] One has to consider the displacement from the pick-up plate as well. The pick-up plate reflects the beam upwards, in order to displace the transmitted beam downwards. The two sides of the pick-up plate form a wedge, that is rotated in such a way that the transmitted beam is diffracted upwards. The cylindrical telescope shrinks the beam horizontally to make it insensitive to vertical misalignment.

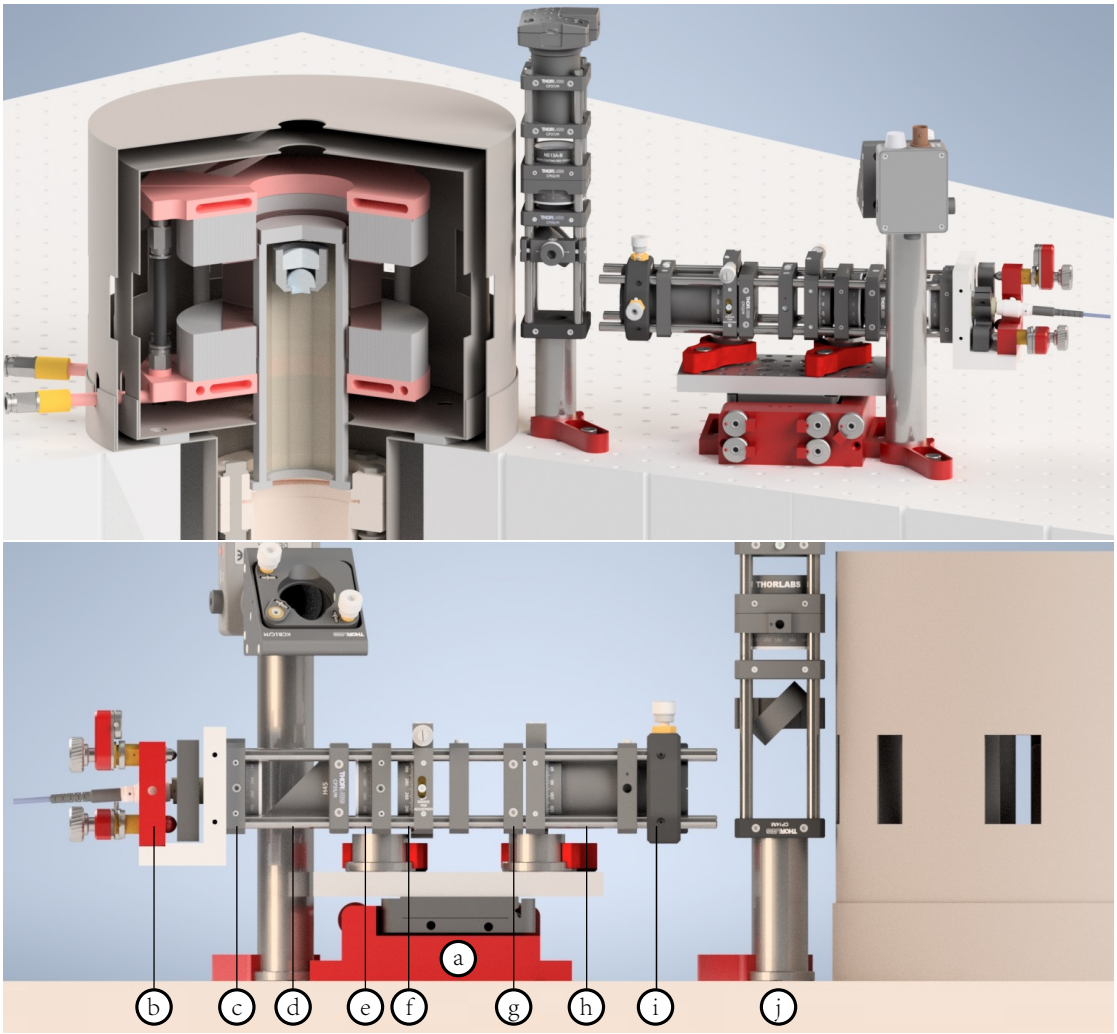

Figure 3.3: Sketch of the cage system. The beam forming optics are mounted in a rigid cage system atop a motorized five axis stage (a). The fiber couple is mounted on a motorized kinematic mount (b), which is attached to the cage system via a custom cage plate. A polarizer (c) is used to filter the polarization. The optical power is monitored using a pick-up plate (d). A waveplate is used to adjust the balance of the vertical and the horizontal polarization component. The beam is made elliptical with a cylindrical telescope (f,g) before it is split apart with a calcite displacer (h). The displacer is mounted in a high precision rotation mount to align it with the surface of the table. The lens (i) focusing the beams is mounted on an x-y-translation mount. Finally a moving mirror is mounted in a vertical cage system (j) between the focusing lens and the μ-metal shielding, that allows us to inspect the beam profile in the focal plane. The vertical cage system (j) also contains an analyzer to visualize the gradient of ellipticity.

Clipping Clipping of the beams takes place at the calcite displacer and the edge of the objective lens. This causes diffraction at the edge which can cause ripple on the isosurfaces [10]. Plane selection is only

[10] The beams forming the horizontal dipole trap are clipped at the edge of the objective lens as well. We have observed an increase in coherence times in the lattice after optimizing the beam alignment. The diffraction at the edge makes the local potential sensitive to vertical beam pointing instabilities. Without clipping the local potential would only be sensitive in second order to vibrations. More on this in can be found in Gautam Ramola's thesis [31]. The lattice beams have a vertical waist of 25 µm in the focus. ($z_R = 2.3mm$ and $w(z = 6mm) = 71\mu m$. The clipping is less severe because these beams are not tilted upwards, so the distance (of the center) to the edge is 150 µm instead of 109 µm). But the losses still amount to

possible, if this ripple is small in comparison to the lattice constant.

The calcite displacer has an aperture of 10 mm and a length of 27 mm. The clipping is smallest, when the beam enters 1.4 mm below the center of the calcite crystal. The free aperture at both end facets of the calcite displacer is only 3.6 mm when measured from the center of the beams. This is only 2.2 times larger than the vertical beam waist, but still larger than the aperture imposed by the edge of the objective lens.

The calcite displacer can be chosen with an aperture that is large enough to neglect the effect of clipping, but the working distance from the objective lens is too small to reduce the clipping losses (of the vertically polarized beam) below 4×10^{-3} . This is due to the finite Rayleigh length z_R of Gaussian beams. The waist of a Gaussian beam evolves as

$$w(z) = w_0 \sqrt{1 + \left(\frac{z}{z_R}\right)^2} \tag{3.5}$$

where ω_0 is the waist in the focus. The waist at the edge of the lens can not be reduced below 57 µm. This minimum is reached when the Rayleigh length equals the radius of the lens. The losses depend on relative aperture size FA, that is the ratio between the beam waist ω and the distance to the edge. The losses can be computed using $P_{Loss} = \Phi_{0,1/\sqrt{2}}(-FA)$ where $\Phi_{\mu,\sigma}$ is the cumulative Gaussian distribution.

The chosen vertical waist of 33 µm leads to a Rayleigh length of 4.1 mm, the waist at the edge is $w(z = 6\text{mm}) = 60\,\mu\text{m}$. The peak intensity is increased by 50% and the clipping by 20%. The clipping can be decreased with the angle Θ between the beams that is proportional to the length of the calcite displacer. Currently the beams are displaced by 42 µm at the edge.

Since the edge of the objective lens lies neither in the focal plane nor in the plane of the lens, we have to solve the wave equation to propagate the diffraction pattern. The peak to peak deviation of the differential light shift in the focal plane is smaller than 10% of the splitting between adjacent lattice sites.

We will now discuss aberrations that can also distort the isosurfaces of constant light shift.

Aberrations The wavefront quality of the beam needs to remain as high as possible, while traversing the optical system. To this end optical aberrations have to be kept low to ensure that the predictions based on Fourier optics remain valid. Aberrations describe the deviation of the beam profile from a reference which typically is a Gaussian. Using a distorted beam with aberration has two drawbacks. It reduces the peak intensity in the focal plane and it will distort the wavefronts close to the the focus causing ripple in the isoplanes of the detuning.

The wavefront quality was studied using a custom ray tracing software to estimate the stability against misalignment [11]. I found that the cylindrical telescope is most stable, if the flat surfaces of both lenses face towards calcite polarizer. In this case the higher order aberrations of the lenses cancel each other. The resulting wave front distortion in the focus are shown in figure 3.4. The components are tilted and only the position of the focal plane and the length of the telescope are tuned numerically to minimize the variance of the optical path length difference (OPD). These differences are computed relative to the principal ray at the center of the Gaussian beam. The OPD is computed for a discrete grid of rays and weighted by the amplitude of the electrical field.

1.4×10^{-3} of the intensity.

[11] I thank Andrea Alberti for providing me with the matlab toolbox.

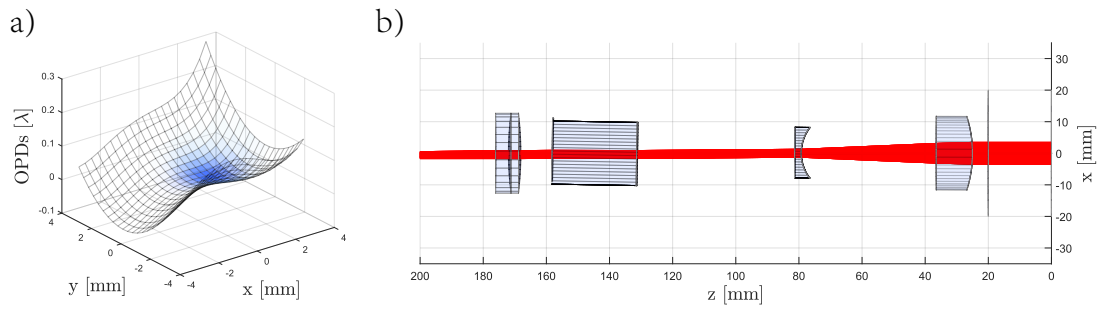

Figure 3.4: The wave front quality is investigated using ray tracing. a) Shows the optical path length difference (ODP) in the focal plane after optimizing both the focal distance and the length of the telescope. The blue shading indicates the relative intensity that serves as a weight. The OPD is computed relative to the principle ray (at the center of the beam). The rms of the OPD is 0.016 λ corresponding to a Strehl ratio of $S = 0.97$, which is close to the diffraction limit. (b) A view on the optical components from the top. The cylindrical lenses are tilted by 0.5° and the focusing lens is moved upwards by 1.4 mm which is half the displacement from the calcite displacer.

A common figure of merit for the beam quality is the Strehl ratio S that is defined as the peak radiance of the beam relative to the ideal beam without aberrations. It can be computed from the optical path length differences (OPD) using [108]

$$S = \left| \left\langle e^{i2\pi \frac{\mathrm{OPD}}{\lambda}} \right\rangle \right|^2 \approx e^{i2\pi \frac{\sigma_{OPD}}{\lambda}}. \tag{3.6}$$

The expression $\langle \cdot \rangle$ indicates the expectation value, that can be computed using the electric field amplitude as a weighting function. The approximation in eq. 3.6 is also called *Maréchal formula*, it gives a lower bound for the Strehl ratio and it is valid for small abberations [109]. The Strehl ratio for the system at hand is 0.97 which is very close to the diffraction limit. This reduces the gradient of detuning by 3%. All components with flat surfaces except the calcite polarizer are tilted to avoid interference between the main beam and back reflections. I verified optically that the reflected secondary beams do not overlap with the main beam in the focal plane.

3.2.2 Alignment

In the following I will describe the alignment procedure. When aligning the cage system one has to avoid clipping at the calcite polarizer, which is the smallest aperture in the beam path, and to make sure that the optical axis is parallel to the optical table on either side of the focusing lens. The second step is to align the beams relative to the atom cloud. The challenge is to overlap the center of focal plane with the center of the atom cloud, while simultaneously avoiding clipping on the edges of the objective lens.

Aligning the cage system The smallest aperture in the setup is the calcite displacer ($10 \times 10 mm$) and its far edge is 140 mm away from the fiber coupler.

Two points are critical when aligning the cage system. The beam must enter the calcite displacer half its displacement below its center and afterwards the two beams must hit the focusing lens symmetrically. The latter can be achieved by mounting the focusing lens on an x-y-translation stage. The former is achieved by mounting the fiber coupler on a custom adapter that not only connects the motorized piezo

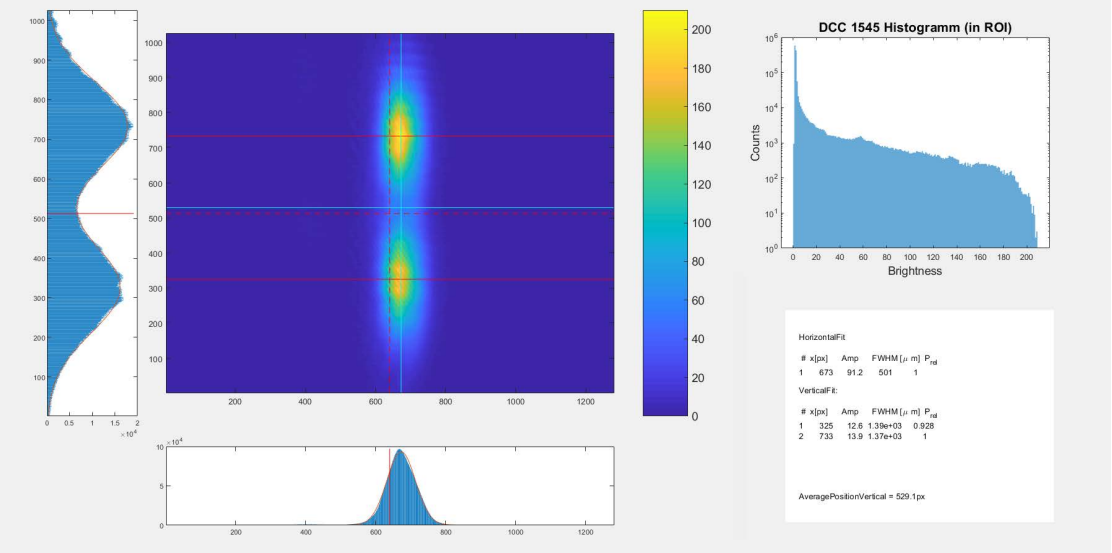

Figure 3.5: A custom beam profiling software implemented in Matlab. It allows to detect the vertical position of both beams (red lines) as well as their center (red dotted line). The center of the beam without the focussing lens is indicated by the light blue cross. The histogram of brightness is plotted logarithmically to allow fast and precise location of the focal plane.

holder with the cage system, but also sets the vertical position of the beam[12]. The beam should not be tilted vertically when entering the calcite to prevent clipping on its far edge. The two sides of the pick-up plate form a wedge that slightly tilts the direction of the transmitted beam. It is rotated such, that its wedge diffracts the beam vertically. The diffraction angle has to be compensated by tilting the fiber coupler. The cylindrical telescope changes the beam size horizontally to render it insensitive to vertical misalignment. The length of the cylindrical telescope can be coarsely aligned by using a shear plate at the position of the focusing telescope. The fine alignment should be done by minimizing the astigmatism, which is measured using a beam-profiling camera. The alignment can be greatly simplified, when measuring the vertical position of the beams and their tilt with a camera that is mounted on a rail. When aligning the focusing lens, the position of the optical axis is indirectly measured. I wrote a software that locates the position of an arbitrary number of peaks with sub-pixel resolution on the camera by fitting Gaussian distributions to the marginal distributions of the image (see figure 3.5). The repeatability and accuracy of the vertical position of the camera was checked using a knife edge. As a cross-check we make sure that the beams intersect at their focal planes. The focal plane can be located precisely by detecting the two points where the peak brightness has dropped by some fraction. This is made easy, by plotting the histogram of brightness semi logarithmically.

Aligning the beam We have to overlap the focal plane where the vertically and horizontally polarized beams cross with the atom cloud. Additionally, the optical axis must be parallel to the surface of the objective lens. We aim for an angle between the optical axis and the lattice planes that is smaller than 0.177°. In this case the isosurface with vanishing differential light shift will shift 10% of a lattice site per 20 µm along the optical axis.
The beams forming the polarization gradient are aligned in three steps. First we use near resonant light

[12] It is not advisable to use translating cage segments plates (such as Thorlabs CPX1) to adjust the vertical position of the calcite, because this would reduce the rigidity of the cage system.

that can push the magneto-optical trap out of its equilibrium position. This allows us to overlap the beams first with the magneto-optical trap and afterwards with the optical lattice. Secondly we optimize the push-out efficiency of atoms that are trapped in the lattice. This allows us to find the position of the crossing point of the two beams relative to the atom cloud. The final alignment is done using microwave spectroscopy.

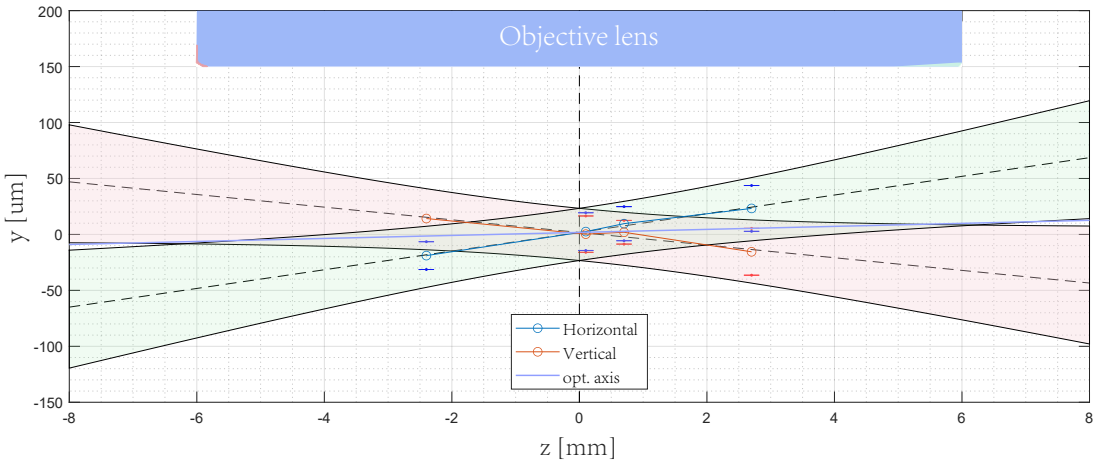

Figure 3.6: Alignment of the polarization gradient beams. The focal plane of the beams can be shifted by moving the focusing lens. The survival probability of the atoms is used to detect the height and the width of both beams. The error bars indicate the positions where the survival has dropped by 50%. The beams intersect at 0.8°, which can be used to infer the vertical scale and the tilt of the optical axis 0.077°.

We use the magneto-optical trap to determine the position of the two beams. Radiation pressure shifts the atom cloud slightly, when it is hit by either of the beams. The MOT is moved towards the position of the lattice, while checking and adjusting the overlap with the polarization gradient beams

We monitor the light scattered at the edges of the objective lens to infer the inclination of the optical axis of the beams. If the optical axis is tilted downwards, the vertically polarized beam will be clipped at the near edge (see figure 3.6). If it is tilted upwards the horizontally polarized beam will be partially reflected from the surface close to the far edge of the objective lens. This asymmetry limits how well we can align the optical axis because an unequal fraction of the clipped light is scattered into the side camera.

Next we overlap the focal plane of the two beams with the optical lattice. The position of the focal plane can be changed by moving the focusing lens along the optical axis. The vertical position of both beams is measured at different positions of the lens, by measuring the survival of atoms in the lattice. The result is depicted in figure 3.6. The errorbars indicate the positions where the survival of atoms has dropped by 50%. The vertical axis is rescaled, because we know that the angle between the two beams is $\Theta = \arctan(\Delta x/f) = 2.8°$. We infer the tilt of the optical axis to be 0.077°. The isosurface with vanishing differential light shift shifts by 10% of a lattice site per 40 µm along the optical axis[13].

[13] The tilt along the perpendicular axis depends on the rotation of the calcite displacer, which is checked using a knife edge and a camera. The tilt is below 0.1°.

Remote control The fiber coupler is attached to a high precision mount that is equipped with piezo driven setscrews [14]. The setscrews can be moved in increments of ca. 20 nm. This allows to control the vertical position of the beam in steps of 200 nm or 0.4 lattice sites. The cage system is mounted to a motorized five axis stage [15]. The setscrews are rotated in discrete steps by piezo actuators, operating as self locking inertia drives („Stick-Slip movement“). This means that they cause neither vibrations nor electrical noise while being inactive and that they remain in position, if the controller is turned off. This makes them ideally suited for applications where both quiet operation and long term stability are needed. The step size however depends on the force acting against the screw, therefore each axis has a step size that depends on the direction and on the distribution of weight on the platform. Any alignment task that requires multiple movements back and forth should therefore be done manually or using external feedback.

Tuning the differential phase The differential phase between the two beams has to be either 0 or π to ensure that the isoplane of vanishing light shift is in the center of the beams.

A movable metallic mirror[16] is mounted between the cage system and the magnetic shielding as shown in figure 3.3. An analyzer is used to convert the gradient of ellipticity into an intensity pattern that is recorded using a camera [17]. The differential phase is adjusted to 0 or π, if the intensity pattern is made up either by two symmetric peaks, or a peak with two symmetric sidelobes as shown in 3.7. The beam profile camera is also used to adjust the beam balance.

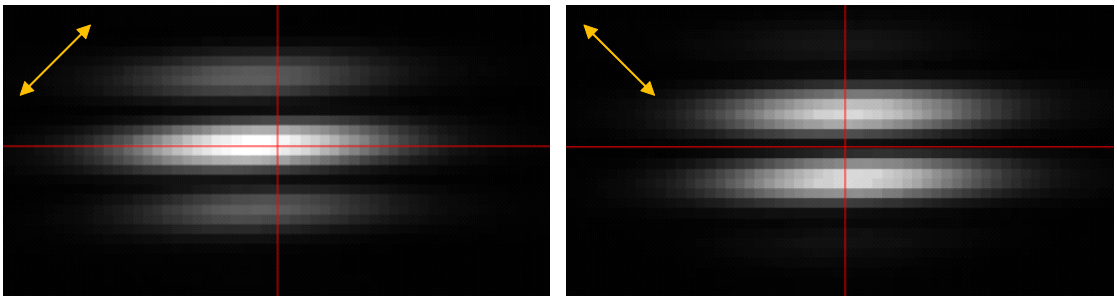

Figure 3.7: Intensity distribution in the focal plane, after an analyzer. The differential phase between the two beams can be measured using an analyzer at 45° or 135°. It can be tuned by either tilting the fiber coupler or by changing the wavelength of the laser. The displayed intensity patterns correspond to a differential phase between the beams of 0 or π. This measurement is used to ensure that the isoplane of vanishing light shift is in the center of the beams. The sign of the polarization gradient is measured spectroscopically. The high contrast indicates a good polarization purity. Each pixel has the size of 5.2 µm.

The differential phase between the two beams can be tuned either by changing the wavelength or by changing the angle under which the beam enters the calcite displacer. We keep the wavelength fixed to the „magic“ wavelength at which atoms in $|\uparrow\rangle = |F = 4, mF = 4\rangle$ are insensitive to the σ^--component of the light.

The remote control over the vertical tilt of the fiber coupler allows us to tune the differential phase between the beams to an integer multiple of π. The accompanying shift in vertical position in the plane

[14] Physik Instrumente PiezoMike N472, driven by E870

[15] New Focus 8082-M, driven by PicoMotor 8742

[16] The mirror is metallic to avoid differential phase shifts between the s- and the p-component of the light. The latter occurs in mirrors with dielectric coatings.

[17] Thorlabs, DCC1545

of the atoms can be compensated by tilting the setup as a whole.

3.3 Measuring atom distributions and light shifts in three dimensions

Microwave spectroscopy is used to measure the differential light shifts induced by the optical polarization gradient. The vertical distribution of light shifts ρ_δ depends both on the position distribution of the atoms ρ and the locally induced light shift ν.

$$\rho_\delta(\nu) = \frac{\mathrm{d}}{\mathrm{dz}} P(\delta \leq \nu) = \frac{\mathrm{d}}{\mathrm{dz}} \int\limits_{\delta^{-1}(\{-\infty,\nu\})} \rho(z)\mathrm{dz} \tag{3.7}$$

The expression $\delta^{-1}(A) := \{x \in \mathbb{R} | \delta(x) \in A\}$ denotes the preimage or inverse image of the set $A \subseteq \mathbb{R}$ and $F_\delta = P(\delta \leq \nu)$ is the cumulative distribution function of δ. If the measurement is restricted to a region where the light shifts are strictly monotonic, then equation 3.7 simplifies to

$$\rho_\delta(\nu) = \frac{\rho(\delta^{-1}(\nu)}{\frac{\mathrm{d}}{\mathrm{dz}}\delta(\delta^{-1}(\nu))} \overset{\delta(\nu)=k\nu}{=} \frac{1}{k}\ \rho\left(\frac{\nu}{k}\right) \tag{3.8}$$

The microwave spectrum $P_{|\uparrow\rangle}$ is broadened due to the finite width of the addressing pulse.

$$P_{|\uparrow\rangle} = (\Omega \otimes \rho_\delta) \tag{3.9}$$

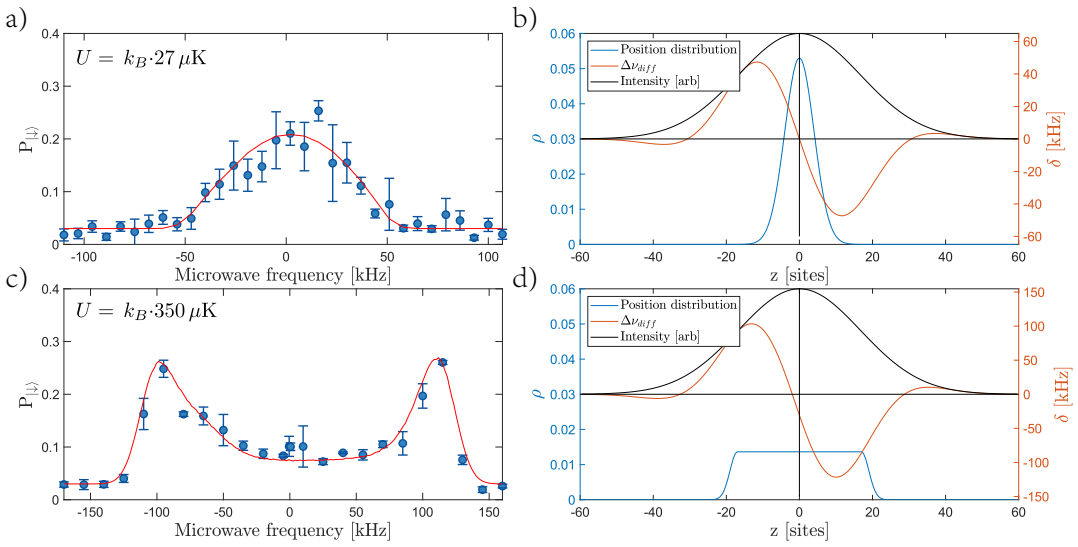

Figure 3.8: Vertical MW spectroscopy. a) Probing a thin sample. If the vertical dipole trap is shallow during fluorescence imaging, then the atomic cloud condenses in a thin volume. The spectrum is broadened, keeping a nearly Gaussian shape. The red curve is a simulated spectrum assuming a gaussian distribution of atoms (σ=4 µm). b) Distribution of light shifts and atom position. c) Probing a thick sample. The vertical hopping can be suppressed by increasing the depth of the vertical optical trap sufficiently. The side-lobes in the spectrum indicate, that the thickness of the atom cloud must be larger than the distance between the turning points of the differential light shift as shown in d).

The following experiments were performed with the microwave pulses that lead to microwave spectra

with Gaussian envelope and a full width half maximum (FWHM) of either 4.2 kHz or 9.3 kHz[18].
We can influence the horizontal shape of the atom cloud by tuning our loading procedure. The vertical dipole trap can be used as dimple to increase the atom density in the center of the field of view. When characterizing the global properties of the lattice (e.g. magnetic fields or variations of trapping frequencies), it is beneficial to spread the cloud across a large horizontal region. We can also change the vertical thickness of the atomic ensemble by tuning the strength of the vertical confinement during fluorescence imaging as shown in in figure 3.8. If the vertical confinement is weak, then the atoms will hop vertically between lattice sites until they condense in the center. Vertical hopping of atoms is suppressed, when the trap depth is 350 µK or deeper during fluorescence imaging. I have written a routine that uses Monte Carlo sampling to simulate spectra for given distributions $\rho = \rho(z)$ and $\delta = \delta(z)$.

If the atom cloud is thicker than half the modulation period of the polarization gradient, then two side-lobes appear in the spectrum as shown in figure 3.8(c). The separation of these side-lobes is a measure for the peak-to-peak modulation of the differential light shift, allowing us to infer the light shift per lattice side in the center of the beam. In the spectrum above the side-lobes are separated by 210 kHz, which corresponds to a gradient of 7.4 kHz site^{-1}. This is 35% smaller than theoretically predicted. This corresponds to a widening of the beam by 20% in each direction. I noted that the beam profile is distorted by the fiber coupler and assume this to reduce the Strehl ratio significantly.

Moving the beam vertically The periodic structure of the light shifts leads to ambiguities in the reconstruction if only one spectrum is taken. This ambiguity can be lifted by recording spectra with different vertical positions of the light field. Conceptually this resembles measuring a beam profile with a knife edge. The Result is shown in figure 3.9. The spectra where recorded using a thin atomic ensemble. We observe that the maxima the measured spectra follow the predicted shape of the light shift (see red curve in figure 3.9.

It is possible to use this measurement to extract the three dimensional distribution of the light shift and the atom cloud. This would be useful as an alignment tool. A preliminary analysis showed that the optical axis of the polarization gradient beams is displaced by 10 µm from the center of the vertical dipole trap. The total light shift falls of exponentially along the line perpendicular to the propagation direction in accordance with the finite horizontal waist of the beams. The total duration of the measurement was over 10 h and more than 4 million atoms were trapped. This illustrates the stability of the experimental apparatus.

3.4 Volume selection

I have done a proof of concept measurement where vertical microwave spectroscopy is performed on volume selected atoms. To this end the experimental sequence is extended to include a second phase in the shallow „science“ lattice and three fluorescence images are recorded as shown in figure 3.10. Volume selection is performed between the first and the second image, using a MW addressing pulse with 0 detuning. The spectral distribution of the remaining atoms is probed between images two and three. Without volume selection the spectrum shows side-lobes, that are separated by 210 kHz. This corresponds to a gradient of 7.8 kHz site^{-1} in the center. With volume selection the spectrum is narrowed

[18] The envelope of the intensity of the microwave radiations is programmed to be a Blackman-Harris window, because it has a finite support. The envelope of the addressing efficiency is however well approximated by a Gaussian fit model.

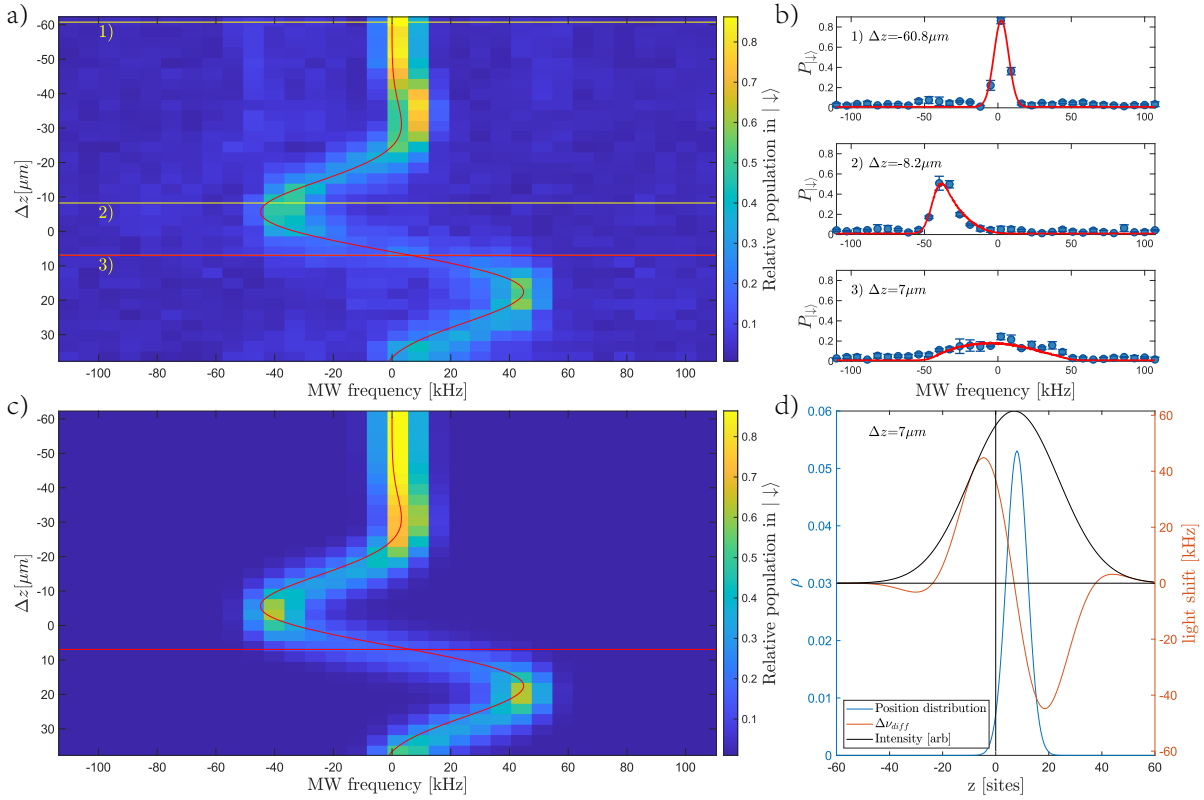

Figure 3.9: Measured and simulated spectra for different vertical position of the polarization gradient beams. a) Microwave spectra are recorded for different beam positions. The atomic ensemble is so thin, that the shape of the polarization gradient is resolved. The red curve indicates the differential light shift as function of the vertical position. b) Example spectra. Three microwave spectra are shown do visualize how the spectrum is shifted. The red lines are simulated spectra based on the same fit parameters. c) Simulated spectra. Both the atom distribution and the polarization gradient are parametrized. The corresponding spectra are computed using Monte-Carlo-Simulation. d) Distribution

and regains a Gaussian profile with a width of $\sigma = 13.5\pm1.2$ kHz. The spectrum is broadened by the finite width of the addressing pulse that has a Gaussian shape with width of $\sigma_{MW} = 8.3\pm0.3$ kHz. The residual linewidth is $\sigma_S = 10.7\pm1.5$ kHz which corresponds to a spatial width of $\sigma_z = 2.0\pm0.2$ sites. We can thus infer, that we have reduced the thickness of the atom cloud tenfold.

The imaging and cooling parameters need to be adjusted, since we observe horizontal hopping. The imaging parameters were chosen to maximize the survival in a small central region around the center of the vertical dipole trap. Without volume selection, the density of atoms is so high, that we do not resolve individual atoms and can not detect horizontal hopping as shown in figure 3.10(b). The depth of the vertical dipole trap during imaging is 0.28 mK=5.8 MHz which is larger than the linewidth of the D2 transition $\Gamma_{D2} = 2\pi\cdot5.23$ MHz. It will be challenging to optimize the imaging parameters for the entire field of view simultaneously, because the depth of the vertical dipole trap is modulated by 50% across the atom cloud that has a radius of 30 µm.

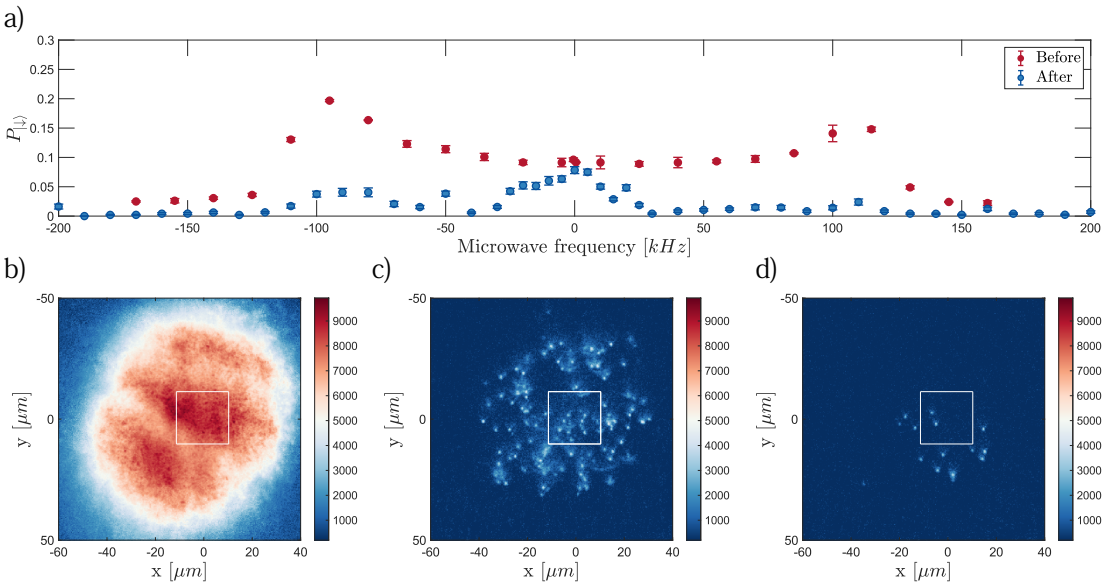

Figure 3.10: Volume selection. a) Vertical microwave spectra with and without volume selection. The residual linewidth is σ_S = 10.7±1.5 kHz which corresponds to a spatial width of σ_z = 2.0±0.2 sites. The images in (b) and (c) show typical atom distributions before and after volume selection. The image in (d) shows the atoms surviving atoms after volume selection and microwave spectroscopy.

3.5 Feasibility of plane selection

Now I will discuss whether the system is stable enough to achieve plane selection. The vibration of the optical polarization gradient relative to the lattice and the spin relaxation are measured. I also discuss how strong a gradient is needed to spectroscopically resolve adjacent planes in the presence of finite spin-dephasing times. I conclude by comparing this technique to other ways of preparing thin atomic samples.

3.5.1 Stability

Addressing atoms in a single layer of the optical trap requires the beams to move less than one lattice spacing d =532 nm. I measured both slow (thermal) drifts and high frequency jitter of the light field.

The thermal stability of the setup was characterized outside the main experiment. I recorded the beam profile in the focal plane with a CCD camera[19]. An analyzer was used to record not only the positions of beams but also their relative phase. The drift was tracked for three days using an image registration algorithm with sub pixel resolution [110]. The vertical position of the beam is strongly correlated with the temperature and it changes by 12.2 site K^{-1}. The temperatures on the experimental table are very stable. The fluctuations are dominated by residual ripple from the primary cooling circuit that has a period of about 12 min and an amplitude of 20 mK.
This corresponds to a vertical drift of 0.24 sites. One should note that we are likely to underestimate the drift, because the lattice might change its position as well. The vertical planes are parallel to the objective lens that is mounted to the vacuum chamber.

The polarization gradient is sensitive to the frequency noise of the light source as well. The sens-

[19] Thorlabs DCC1545

itivity was measured to be $\partial_\nu \varphi_0 = 2\pi/50$ rad/GHz. The TiSa laser used to generate this light has an linewidth of <300 kHz. It is locked to a temperature stabilized reference cavity which drifts less than 100 MHz d^{-1}[73]. This corresponds to a negligible position jitter of the point of zero detuning and a drift of 120 nm d^{-1}.

The jitter of the polarization gradient was measured using Hahn's spin echo sequence. This sequence extends the Ramsey interferometer described in chapter 2 by an additional π pulse exactly between the two $\pi/2$ pulses. This inverts the propagation direction of the spinors on the Bloch sphere and makes the final phase insensitive to inhomogeneities that are constant in time. This technique was originally invented in the field of nuclear magnetic resonance [56]. It has been used to study sources of decoherence for systems of neutral atoms [54, 111] and recently by my colleague Gautam Ramola in the experiment at hand [31].

The polarization gradient is increased twice during the spin-echo sequence as shown in figure 3.11(a). The contrast is measured as a function of the gradient of detuning. The intensity of the beams is not stabilized leading to a systematic imbalance of total power applied in both pulses. This leads to a strong decay in coherence. When the thermal effect is compensated and post selection is applied the contrast at 90% optical power is restored to 58±7 %. This corresponds to an rms detuning of 665 Hz for a gradient of 21.4 kHz site^{-1}.

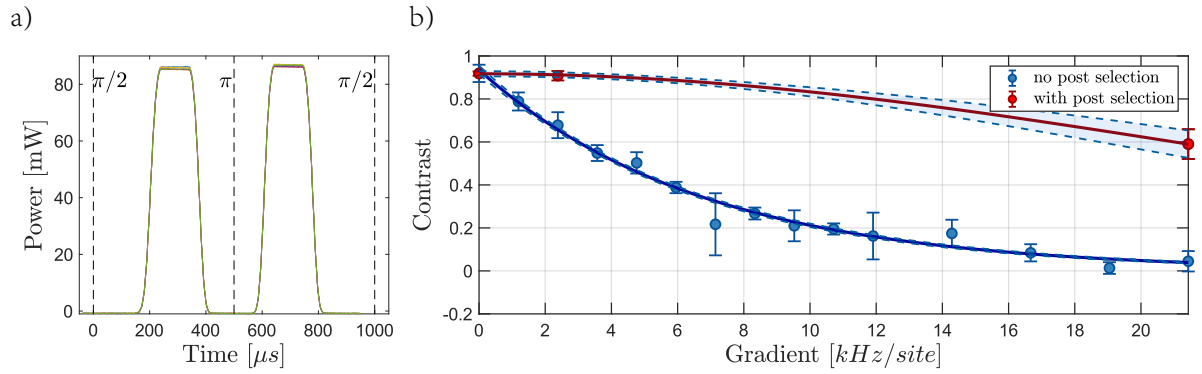

Figure 3.11: A spin echo measurement was performed with a total duration of 1 ms. The polarization gradient was turned on symmetrically for 100 µs before and after the rephasing pulse. The contrast is measured as a function of optical power. There is no intensity feedback for the optical power and the second pulse contains more optical power than the first. When we compensate the thermal effect and apply post selection the contrast at 90% optical power is restored to 58±7 %. This corresponds to an rms detuning of 665 Hz for a gradient of 21.4 kHz site^{-1}.

I conclude that the light field is stable enough to perform plane selection. It could be made more stable if the focusing lens is brought closer to the focal plane. In the experiment at hand the focal length can not be changed significantly because of the μ-metal shielding.

3.5.2 Spin relaxation time T_1

Any coherent manipulation of spins is limited by the spin relaxation or T_1-time, which describes the decay of the internal spin state into a random mixture [54]. Off-resonant scattering events where the atoms randomly absorb and re-emit photons of the optical dipole trap limit the T_1-time in our lattice. Using 60 mW of optical power to create an optical polarization gradient reduces the T_1-time from 330(70) ms to 174(70) ms as shown in figure 3.12.

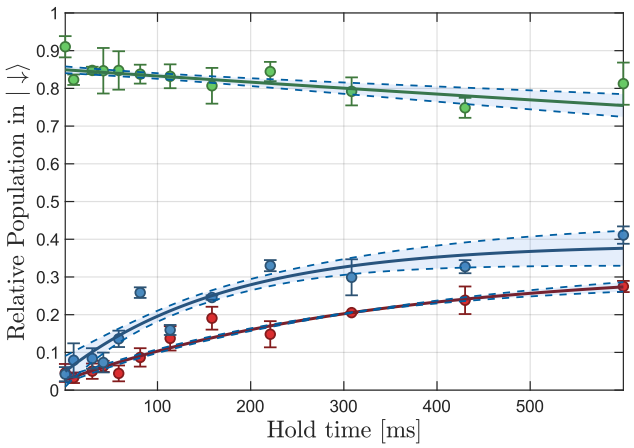

Figure 3.12: The spin relaxation time T_1 was measured. The spin relaxation time in the dipole trap is 330(70)ms (red curve) and it decreases to 174(70) ms in the presence The power of the gradient field was set to 60 mW (blue). The survival rate without spin selective push-out pulse is 4.1(5) s (green).

We can achieve a splitting of 40 kHz site^{-1} with an optical power of 120 mW and a T_1-time of 85 ms. I will show in the next section that this is sufficiently long to spectroscopically resolve individual planes with less than 2% of the atoms in adjacent planes remaining.

3.5.3 Robust adressing pulses

So far we have used microwave pulses with (nearly) Gaussian envelope to spectroscopically investigate the vertical distribution. They combine a large peak transfer efficiency with a small full width half maximum (FWHM). The microwave pulse used to address a single plane should have a flat-top frequency response to make it robust against small fluctuations. In the absence of decoherence the frequency response to a microwave pulse with fixed frequency is proportional to the Fourier transform of the instantaneous Rabi frequency. It would therefore in principle be possible to tailor driving pulses with arbitrary frequency responses.
In our lattice we observe a finite coherence time of 1 ms [31], which will reduce the peak addressing efficiency of slow and spectroscopically narrow pulses. In this section I will numerically investigate whether we can reach a peak efficiency of 90% or higher and a spectral resolution of .

The evolution of a two level system that is subject to an external driving field can be computed by solving the optical Bloch equations [50]. The optical Bloch equations can be extended by including both the spin relaxation time T_1 (also called longitudinal decoherence) and the spin dephasing time T_2 as damping terms [54]. It holds

$$\mathrm{i}\hbar\,\mathrm{d_t}\hat{\rho} = [\mathcal{H},\hat{\rho}] - \mathrm{i}\left(\frac{1}{\mathrm{T_1}} + \frac{1}{\mathrm{T_2}}\right)\sigma_x - \mathrm{i}\frac{1}{T_1}\hat{w}\,\sigma_z \tag{3.10}$$

where $\sigma^{x,y,z}$ are the Pauli matrices and $\hat{w} = \hat{\rho}_{gg} - \hat{\rho}_{ee}$ the inversion.
A flat-top frequency response of the atomic magnetic dipole moment can be achieved by tuning not only the Rabi frequency but also detuning [112]. This is generally referred to as adiabatic rapid passage [113] and has been demonstrated e.g. in 1996 with meta stable helium passing through beam [114]. The technique can be understood with the geometric picture of the Bloch sphere. We imagine a pulse

with fixed (and large) Rabi frequency where the microwave frequency is swept slowly across the atomic resonance. The atom is initially prepared at either pole. During the sweep the torque vector slowly rotates from one pole to the other dragging, the spin that rotates around it, behind.

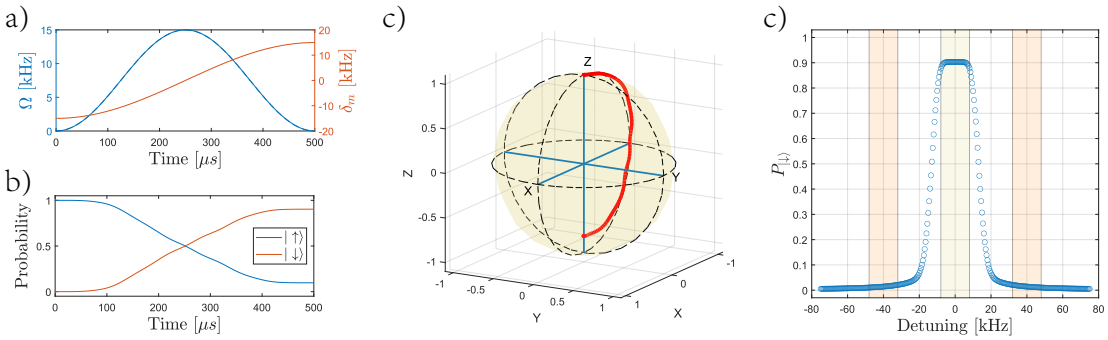

Figure 3.13: We can use the optical Bloch equations to simulate the evolution of the internal state. We assume a T_1 time of 150 ms, a T_2 time of 1 ms. Both the intensity and the frequency of the microwave pulse are modulated in a sinosoidal fashion (a). b) The population transfer as a function of time. c) The time evolution on the Bloch sphere and d) shows a simulated spectrum. The shaded areas indicate the adjacent lattice sites (+-20%) when I assume a splitting of 40 kHz. The addressing efficiency for atoms in the correct plane is 90% and 1.5% for the adjacent planes.

In our group we demonstrated position dependent spin flips [115] using microwave pulses with a shape suggested in [112]

$$\begin{aligned} \Omega(t) &= \Omega_m \sin^2\left(t\frac{\pi}{t_0}\right) \\ \delta(t) &= \delta_0 - \delta_m \cos^2\left(t\frac{\pi}{t_0}\right) \end{aligned} \tag{3.11}$$

where $\Omega_(m)$ is the (maximum) Rabi frequency (on resonance), δ the detuning, δ_0 and δ_m are the detuning at $t = 0$ and the maximum detuning.

In the experiment at hand the T_1 is limited by scattering of lattice photons to 330 ms. In the presence of strong polarization gradient this will be reduced to 85 ms. The spin dephasing or T_2 time has been measured to be better than 1.7 ms in free fall and to be up to 1 ms in the lattice [31]. The T_2 time has so far only been measured for thick samples without prior plane- or volume-selection. I therefore assume the spin dephasing time for atoms that are confined to a single lattice plane to be at least 1 ms. The numerical simulation shown in figure 3.13 shows we need to split the adjacent planes by 40 kHz. Then we can implement a pulse with a peak efficiency of 90%, a flat-top width of 20% of a lattice site and less than 2% of atoms surviving in adjacent planes. Both the peak addressing efficiency and the survival of adjacent planes are limited by the T_2-time. Increasing the T_1-time beyond 85 ms yields only marginal improvements of less than 0.1%.

3.5.4 Comparison with other techniques

Let us now compare the technique at hand with other ways of preparing thin atom ensembles. First I will compare plane selection with polarization gradients with the established technique of using magnetic field gradients. Then accordion lattices will be discussed. Finally I will discuss the feasibility of using a vertical super lattice between the vertical dipole trap and light at 1 032 nm.

Many experiments use position dependent Zeeman shifts to map positions onto different resonance frequencies [98–103]. It is common to use the coils generating the quadrupole field needed to create a magneto-optical trap. The isosurfaces of quadrupole fields generated by coils in anti-Helmholtz configur-

ation are ellipsoids and thus curved. To address single planes it is necessary to reduce the curvature by shifting the center of the quadrupole field with homogeneous bias fields. The distance between the atoms and the center must be chosen large enough to ensure the required flatness across the region of interest. Additionally, the center of the field and the atomic cloud must lie on a line that is perpendicular to the planes [98].
A typical value is to shift the center by Δz =0.4-0.6 mm to achieve a deviation of δ =50 nm or 10% of a lattice constant of 512 nm over a region of interest with radius 50 µm. There is a trade-off between the flatness of the isosurface and the required stability of the magnetic field. The flatness described above requires the magnetic field to fluctuate by less than $\delta z/\Delta z = 1 \cdot 10^{-5} = 10ppm$. These requirements are similar to the stability of the magnetic guiding field discussed in section 2.2. Commercially available power supplies offer a stability of up to $5ppm$[20], which should be sufficient for the experiment at hand. The high power consumption of the gradient coils will however lead to thermal expansion, that can displace the position of the magnetic field. The temperatures of the coils can be measured and the thermal expansion can be compensated [100].
The gradient coils of the DQSIM experiment were designed to run with currents up to 32 A generating magnetic field gradients up to 300 G cm^{-1}. This would correspond to a separation of 40 kHz site^{-1} and a power consumption of 1.2 kW. The optical polarization gradient would achieve the same splitting with 126 mW (or 82 mW, when using the theoretical value).
The advantages of using optical polarization gradients are short switching times, negligible heat dissipation close to the vacuum chamber and the vanishing curvature of the isosurface with vanishing light shift. Superior wavefront quality is needed to prevent aberrations to locally distort the isosurfaces. The presence of the light field also induces scattering thereby reducing the longitudinal decoherence time (T_1). This is a limitation especially for lighter alkaline atoms with their smaller fine structure splitting than cesium. Further investigation is needed to assess the feasibility of the polarization gradient technique for lighter alkalines such as Na^{23} and Li^6.

Another technique to confine the atom cloud to a single vertical layer of the optical dipole trap is the use of one of two types of „accordion lattices“. One relies on retro reflecting red detuned light on a surface under tunable angles [103, 106]. The lattice spacing is changed tenfold from 150 µm to 10 µm. This is not feasible for the experiment at hand, since the focal plane of the objective lens is located at 150 µm. We neither have the optical power, nor the optical access available to realize such an accordion. Another type of accordion lattice was recently used to create a 2d Bose gas[105][21]. A pair of polarizing beam splitters is used to create two parallel beams with the same linear polarization. A focusing lens is used to create a red detuned optical dipole trap with variable spacing. This technique requires the beam to interfere at an angle of 15° to realize a lattice constant of 2 µm with a wavelength of λ =512 nm. Confining the atoms in the anti node of repulsive potentials ([61, 103, 104]), also requires the use of tightly focused laser beams with too large a divergence angle to avoid clipping at the edge of our objective lens.

We can create a vertical super lattice by superimposing the vertical dipole trap (with λ=1 064 nm) with a second one at 1 032 nm. The coating of our objective lens is highly reflective at this wavelength and it can be generated using Yb:YAG-Lasers. The fourth antinode of the superlattice would lie in the focal plane at 150 µm. Parametric heating could be employed to remove all atoms except those in the focal plane where the local minimum of the second lattice would coincide with the local maximum of the first.

[20] High Finesse UCS/BCS series e.g. UCS15/25
[21] The concept has been studied optically in 2008 [116]

The spacing of the super lattice would be 33 µm which suffices if combined with some form of volume selection.

3.6 Outlook

Optically resolving individual planes So far we have assumed plane selection to be a prerequisite to performing many-particle interferometry. In the experiment at hand it suffices to perform volume selection, because we can extract the vertical position of the atoms from the fluorescence images as shown in figure 3.14. Not only do we see a clear difference between the images of atoms that are sharply imaged, but also we can distinguish atoms that are above the focal plane from those below. The images were taken using a numerical aperture of ca. 0.3 which corresponds to a depth of focus of $DOF = 4.5\,\mu\text{m}$. The asymmetry in the atom images is therefore seen at about two times the depth of focus. If we increase the numerical aperture to 0.92, then the depth of focus will be reduced to $DOF = 0.25\,\mu\text{m}$. This means, that we will be able to distinguish adjacent lattice planes, that are separated by $d = 0.532nm > 2 \cdot DOF_{NA=0.92}$.

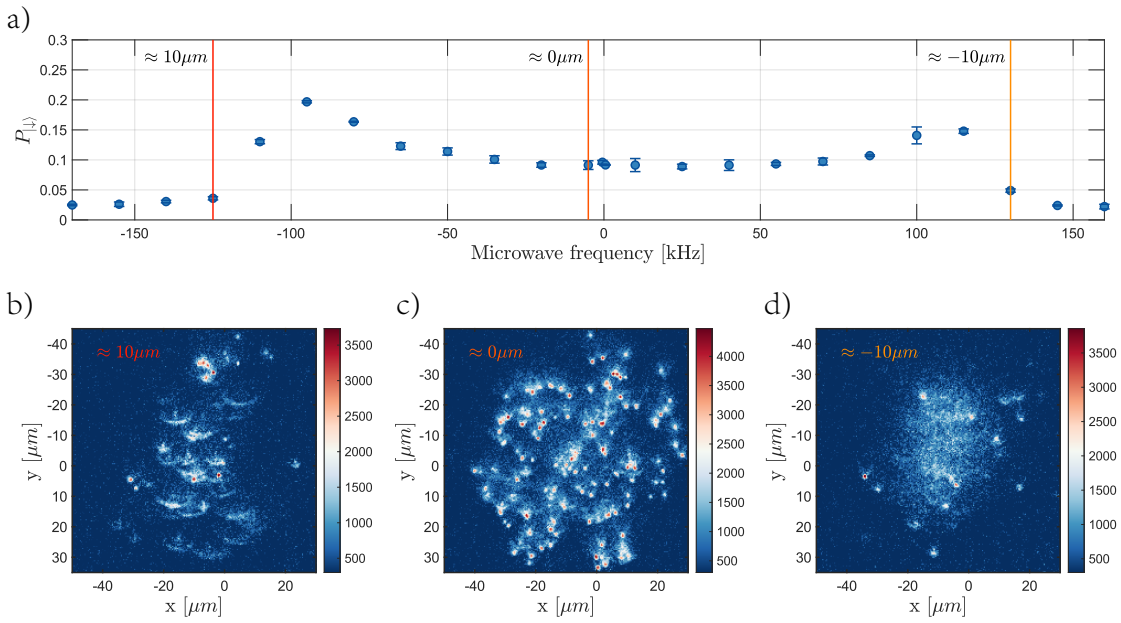

Figure 3.14: Evolution of the point spread function. a) Vertical microwave spectroscopy is performed with a thick atomic ensemble. The two side-lobes of the spectrum indicate that the atom cloud covers both extrema of the polarization gradient. b)-c) The point spread function evolves asymmetrically along the line of sight.

Being able to distinguish atoms above and below the focal plane is highly desirable, because it would allow us to directly detect and compensate vertical shifts of the polarization gradient. If the isoplane of vanishing light shift moves upwards, more atoms above the target plane would survive the attempt of plane selection and vice versa.

The atom images evolve asymmetrically along the imaging axis due to higher order aberrations in the imaging system [117]. The atoms can be considered point-like sources of light, because the position uncertainty of the wavepackage is much smaller than the resolution of the imaging system. Atoms can therefore be used to measure the point-spread function (PSF) of the imaging system. The latter is – by definition – the image of a point source. It has been shown that one can engineer the PSF using spatial light modulators in an intermediate plane of the imaging system [118]. This can be used to correct

existing aberrations and then to (re-)introduce aberrations that will cause a controlled, anti-symmetric evolution of the PSF along the line of sight.

Three dimensional microwave cooling Another possible application of the polarization gradient is resolved sideband cooling using microwave radiation. The gradient of differential light shifts gives rise to a spin-dependent force that separates the minima of the potentials trapping the two internal states

$$\Delta z = \frac{h\partial_z \delta}{m_{Cs}\omega_z^2}. \tag{3.12}$$

This displacement lifts the orthogonality of different vibrational eigenstates of the respective potentials and allows us to use microwave radiation to induce motional sideband transitions [91].

For volume selection we need to increase the trapping frequency in order to avoid driving motional sidebands. It is important to consider the finite waist of the vertical dipole trap of 50 μm. If we consider a circular region of 40 μm then the Franck Condon factor of the first order sideband will be smaller than 3% for a gradient of 10 kHz site^{-1}. For 40 kHz site^{-1} the Franck-Condon factor remains below 6% within a radius of 20 μm.

If the vertical trapping frequency is reduced to ω_z =20 kHz and a gradient of 55 kHz site^{-1} is applied, then the potential minima in the center of the vertical trap are shifted 19.8 nm apart. The spatial Lamb-Dicke parameter in the center of the trap would be $\eta = 0.23$ which is comparable with the conditions in our one dimensional experiment, where a cooling of >95% per direction using Raman transitions was achieved [61].

Spatial compression of an atomic ensemble The atom cloud extends vertically over more than 40 planes, and less than 2% of the atoms would remain after removing atoms from all but a single plane. We plan to compress the atom cloud using a release-retrap technique that was first demonstrated with cesium in 1998 by the group of David Weiss [9] and later with rubidium experiment of our own group [119]. Recently a BEC was created without evaporative cooling but by compressing a cloud of 2000 Rb87 atoms [10].

The idea is to turn off the vertical dipole trap adiabatically and use the horizontal dipole trap as an (anharmonic) pendulum. The atom cloud will undergo a "breathing" motion, and its size will periodically shrink and expand. The atom cloud will be compressed if the three-dimensional lattice is restored after one-quarter of the oscillation period. The atoms will, however, acquire vibrational energy, which can be removed by resolved sideband cooling.

We have performed a proof of concept measurement, where the atom cloud is compressed two-fold horizontally in a single compression cycle [79]. The atom cloud is so large that the anharmonicity of the dipole trap limits the compression ratio of the first compression single. A Monte-Carlo simulation showed that only two cycles of compression are necessary to reach the limit imposed by our cooling efficiency of 90%. In the first one, we optimize the number of atoms in the harmonic region. One option is to minimizing the 90% quantile of the distance, which is the radius of a circle that containing 90% of the atoms. In the 2nd iteration, we would optimize the peak density in the center. We also investigated the limitations of the release-retrap technique quantum mechanically [79]. Tunnelling and momentum uncertainty (at release) limit the final width of the cloud to 1.6 lattice sites. If we reduce the width of the atom cloud to nearly a single lattice site, then light-assisted collisions will limit the filling factor of the

lattice. We would, however, still be able to trap over a thousand atoms in one plane across.

The density of atoms can be further improved by sorting the atoms. We need state-dependent transport, which we recently demonstrated [31], and the ability to position-dependently manipulate the internal state of the atoms. The latter can be realized using Raman lasers with suitable intensity patterns. These patterns can be generated using a spatial light modulator in conjunction with the high numerical aperture of our objective lens. We have characterized a spatial light modulator and studied both holographic, and methods of direct imaging [120, 121]. I have summarized my contribution to this development in appendix C.

Low entropy states with unity filling factor have been realized in our one-dimensional system and can be efficiently implemented in two dimensions [122]. In the latter case, one would sort atoms not individually but transport all atoms in matching sections simultaneously. On average, 12 iterations are needed to increase the filling factor in a 31×31 square with 961 lattice sites from 40% to unity [122].

The creation of low entropy states opens the path to study many-particle phenomena, such as simulating quantum spin liquids [123, 124] and highly entangled cluster states [30].

CHAPTER 4

Measuring the Wigner function

There are three independent ways to formulate the laws of quantum mechanics. The most commonly used is the Hilbert space formalism that captures the pictures formulated by Schrödinger and Heisenberg. The second evolves around Feynman's path integrals. The third is to formulate quantum mechanics in phase space using the Wigner function [125].

In this chapter I will propose a novel scheme to directly measure the Wigner function of neutral atoms trapped in an optical dipole potential. To my knowledge this has not been attempted before. So far direct measurements of the Wigner function are proposed for ions and microwave cavities [126], with the latter being experimentally realized [20, 127]. It can be shown, that the Wigner function is proportional to the expectation value of the displaced parity operator [33]. In our proposed experiment, the displacement operation is realized by controlling the lattice position in time. The state dependent trapping potential is used to measure the parity of the atomic wave function using Ramsey interferometry.
After introducing the Wigner function and its properties in section 4.1, I will discuss how to measure the Wigner function at the origin 4.2. Section 4.3 is dedicated to measuring arbitrary points in phase space. I will discuss how the local periodicity and the finite extend of the dipole trap affects the measurement fidelity. Finally a conclusion will be drawn in section 4.4 where I relate the results to the broader context of state reconstruction.

The Wigner function and its properties The Wigner function was first introduced by E.Wigner as an auxiliary function [128]

$$\mathcal{W}(\mathbf{x},\mathbf{p}) = \frac{1}{2\pi}\int \mathbf{dy}\, \psi^*(\mathbf{x}-\frac{\hbar}{2}\mathbf{y})\psi^*(\mathbf{x}+\frac{\hbar}{2}\mathbf{y})\mathbf{e}^{-\mathbf{i}\,\mathbf{py}}. \tag{4.1}$$

Here ψ is the wave function as used in the Schrödinger picture. It was later shown, that the Wigner function is a representation of the density matrix in phase space under Weyl's correspondence principle between operators and complex kernel functions [129]. Shortly thereafter the quantum mechanical equivalent to Lioville's theorem was found [130]

$$\partial_t \mathcal{W} = \frac{H\star\mathcal{W}-\mathcal{W}\star H}{\mathbf{i}\hbar} := \{\{H,\mathcal{W}\}\}. \tag{4.2}$$

Here $\{\{\cdot\}\}$ denotes the Moyal brackets and $\star := \mathbf{e}^{\frac{\mathbf{i}\hbar}{2}(\overleftarrow{\partial_x}\overrightarrow{\partial_p}-\overleftarrow{\partial_p}\overrightarrow{\partial_x})}$ is called the „star"-product. This shows that the dynamics of a single quantum particle resemble the evolution of a statistical ensemble of classical

particles [130]. The Wigner function of a particle trapped in a harmonic potential undergoes a rigid rotation around the origin of the trap. The transition from quantum mechanics to classical physics is easily done in this formalism in the limit $h \to 0$ of vanishing Planck's constant. In this case the Moyal brackets smoothly transform into the Lioville brackets.

The equivalence and independence of the phase space formulation of quantum mechanics of a single non-relativistic particle was shown in [125]. There are many representations of the density matrix in phase space such as the Glauber-Sudarshan-P distribution [131] and the Husimi-Q distribution [132]. These representations are given as real valued functions on either the complex plane or two dimensional real space. They are mathematically equivalent but only the Wigner function fulfills the condition that its marginal distributions recover the probability densities in x and p [133]. It holds

$$\begin{aligned} \langle \hat{x}|\hat{\rho}|\hat{x}\rangle &= \int_{-\infty}^{\infty} \mathcal{W}(x,p)\mathrm{d}p \\ \langle \hat{p}|\hat{\rho}|\hat{p}\rangle &= \int_{-\infty}^{\infty} \mathcal{W}(x,p)\mathrm{d}x. \end{aligned} \tag{4.3}$$

More detailed discussions can be found in both review articles [125, 133–135] and text books (e.g. [136]). A concise introduction with emphasis on explicit calculations is given in [137], while a mathematically rigorous introduction to the phase space formulation of quantum mechanics can be found in [133]. Extending quantum mechanics in phase space to systems with spins and relativistic effects is still a field of ongoing research [135, 138–140].

The simulations presented throughout this chapter employ a numerical solver (written by A. Alberti) that was developed and used for previous publications [76, 141, 142]. It solves the evolution of a two-level atom under the influence of a time dependent trapping potential. Here I restrict the simulation of the evolution to the interrogation time between the two $\pi/2$-pulses of the Ramsey interferometer and neglect the imperfections of both the initial state preparation and the microwave pulses. The model is one dimensional and I assume the atoms to be cooled into the ground state along the orthogonal directions. I will discuss the two dimensional case in section 4.3.

4.1 The Wigner function as an observable

So far we have discussed properties of the Wigner function as a whole. The Wigner function can be used to express quantum mechanical expectation values as classical phase-space averages [128]

$$|\langle\psi|\varphi\rangle|^2 = 2\pi\hbar \int_{\mathbb{R}} \mathrm{dx} \int_{\mathbb{R}} \mathrm{dp} \mathrm{W}_{\psi}(\mathrm{x},\mathrm{p})\mathrm{W}_{\varphi}(\mathrm{x},\mathrm{p}). \tag{4.4}$$

It is for this reason that it is also referred to as a quasi-probability distribution. The original definition of the Wigner distribution as an auxiliary function does not provide a physical meaning to its values at individual points in phase space [128]. Neither does the alternative definition as the Weyl transform of the density operator [137].

An alternative approach based on series expansions of displacement operators was invented by Cahill and Glauber [143, 144]. They reintroduced the Wigner function as the expectation value of an observable, which was subsequently identified as the displaced parity operator [33]. The Wigner function $\mathcal{W}(x,p)$ is thus proportional to the expectation value of the parity operator about the phase-space point (x,p)

$$\mathcal{W}(x,p) = \frac{2}{h} \langle\psi| \Pi_{x,p} |\psi\rangle . \tag{4.5}$$

The displaced parity operator $\Pi_{x,p}$ is given as $\Pi_{x,p} := D(x,p)\Pi D(x,p)^{-1}$ where Π denotes the parity operator and $D(x,p)$ is the Glauber displacement operator that shifts the wave package by (x,p)[1].

The Wigner function can thus be directly measured, if we implement both the displacement and the parity operator. Implementing the former can be done by shifting the lattice instead of the atom. A displacement in space corresponds to a sudden position jump and a displacement in momentum space to setting the lattice in motion with a constant velocity. The parity can be measured with a sequence that maps all even vibrational levels on $|\uparrow\rangle$ and the uneven levels on $|\downarrow\rangle$.

In the next section I describe how we can exploit the state dependent potential to measure the parity of the wavefunction, which is equivalent to measuring the Wigner function at the origin.

4.2 Measuring the Wigner function at the origin

The Wigner distribution describes the parity of the wave function with respect to different positions in phase space. In this section I will describe how to use Ramsey interferometry to measure the parity of the atomic wavefunction and thus the Wigner function at the origin.

In a Ramsey interferometer an atom collects a phase φ between the two $\pi/2$ pulses that is proportional to the average differential light light δ during the interrogation time τ. We have recently demonstrated that the trap depth [31] can be measured by inducing vectorial differential light shifts δ between the long-lived states $|\uparrow\rangle = |F = 4, m_F = 4\rangle$ and $|\downarrow\rangle = |F = 3, m_F = 3\rangle$. The vectorial component of the differential light shift is proportional to the ellipticity and the average trap depth

$$\delta(\vec{r}, \epsilon) = (\eta_s + \eta_v \epsilon) U(\vec{r})/(2\pi\hbar). \tag{4.6}$$

One can use the linear dependence between the ellipticity and the vectorial component of the differential light shift, to measure the local trap depth $U(\vec{r})$. This is called ‚Ramsey imaging'. We exploit the phonon-dependent contribution to the light shift to measure the parity. The differential trap depth ΔU must be varied in time, that the differential phase acquired by the first two vibrational levels differs by π

$$\Delta\Phi(1) = \Phi(n=0) - \Phi(n=1) = \int_0^\tau \mathrm{dt}\Delta\omega(\mathrm{t}) \stackrel{!}{=} \pi. \tag{4.7}$$

In the harmonic approximation the eigenenergies $E(n)$ form an equidistant ladder

$$E(n) = U + \hbar\omega(n + \frac{1}{2}). \tag{4.8}$$

Here n denotes the vibrational level or phonon number. The corresponding eigenstates are also referred to as Fock states. The differential light shift $\delta_n = (E_\uparrow(n) - E_\downarrow(n))/h$ depends affine linearly on the differential trap frequency $\Delta\omega = \omega_\uparrow - \omega_\downarrow$

$$h\delta_n = U_\uparrow(n) - U_\downarrow(n) = (\eta_s + \eta_v\epsilon)U + \hbar\Delta\omega(n + \frac{1}{2}) \tag{4.9}$$

This means that if the differential trap depth is modulated in such a way that equation 4.7 is fulfilled, then it holds $\Delta\Phi(n) = \Phi(0) - \Phi(n) = n\,\pi$. We can use the second $\pi/2$ pulse of the Ramsey interferometer to project all even Fock states onto one spin state and all odd spin state onto the other. We conclude that in the harmonic approximation we can measure the parity of arbitrary states with a single measurement. In

[1] An equivalent Result was found a year earlier by Grossman [145]

an optical lattice however only a limited number of bound states exists [90] and the energy spacing is not constant. The deviation of the lattice potential from the harmonic approximation is called anharmonicity. I will now discuss the reconstruction error arising from the anharmonicity of the lattice potential.

The lattice potential For simplicity we will restrict this analysis to the case of one dimensional optical dipole traps formed by counter propagating laser beams

$$U(z) = -U_0 \cos^2\left(\frac{2\pi}{\lambda_{DT}} z\right). \tag{4.10}$$

The eigenstates describing localized atoms in individual lattice wells are given by the Mathieu's functions [90] and their energy levels obey

$$E_n = -U_0 + \hbar\omega\left(\frac{1}{2} + n\right) - E_{rec} n + O((E_{rec} n)^2). \tag{4.11}$$

The atomic oscillation frequency, or trapping frequency ω can be computed from the trap depth

$$\omega = 2\pi \sqrt{2U_0 / \left(m_{Cs} \lambda_{DT}^2\right)}. \tag{4.12}$$

The spacing between the eigenenergies is not constant, but the deviation from the energy levels of the

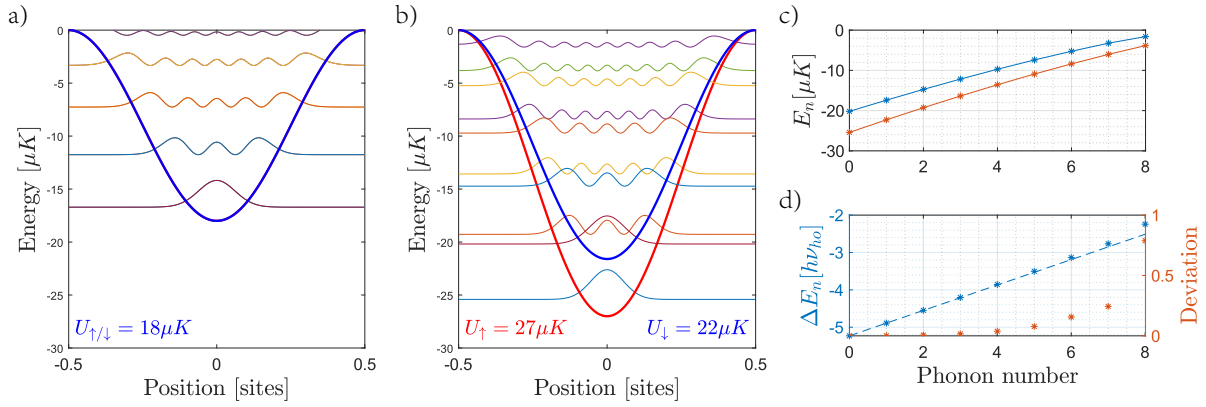

Figure 4.1: (a) The eigenenergies in the lattice potential. (b) The lattice depth is state dependently lowered. (c) The eigenenergies in the unbalanced lattice. The slope of the eigenenergies depends not only on the trapping frequency ω but also on the recoil energy E_{rec}. (d) The differential light shift ΔE_n is in first order insensitive to the Phonon number n. The relative deviation from the harmonic approximation is below 10% for the lowest five vibrational levels. The energies are expressed in units relative to the trapping frequencies in the harmonic oscillator ν_{ho}.

.

harmonic approximation depends only in second order on the trap depth. From figure 4.1,d) we see that the differential energy $\Delta E(n)$ of the lowest five Fock states deviates less than 10% from the differential energy of the harmonic approximation. This is remarkable since only 14 bound eigenstates exists at the trap depth of 18 μK.

Tuning the parity operator We can use a thermal ensemble of atoms to tune the duration for which the lattice is imbalanced. If the imbalance is fixed, then a thermal ensemble of atoms will undergo a

periodic modulation of the Ramsey contrast. The spinors will re-phase at integer multiples of $2\pi/\Delta\omega$. Likewise at odd multiples of $\tau_P = \pi/\Delta\omega$ even states will have re-phased with the ground state and odd states will have acquired a relative phase of π.

So far we have considered a static imbalance between the two potentials, leading to a fixed differential

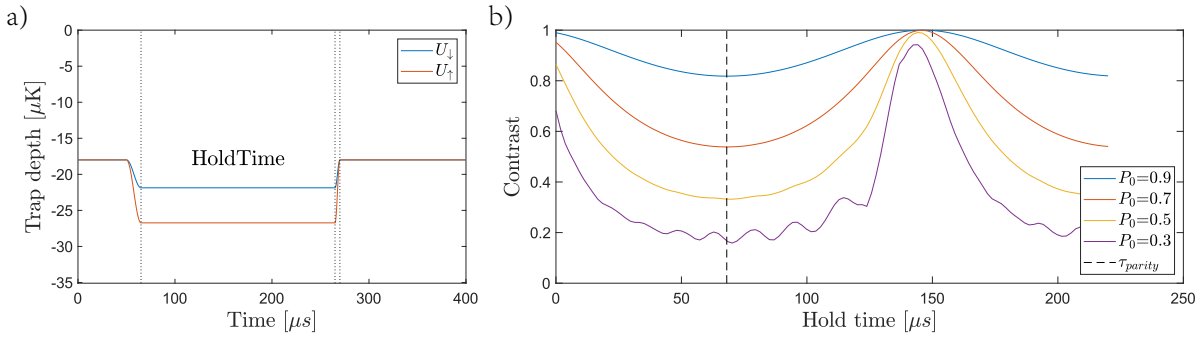

Figure 4.2: We can perform Ramsey interferometry with fixed probe time of e.g. 400 μs and varying „hold time“ of the imbalance. On the left we see how the trap depth is varied and on the right we see the periodic revivals of the contrast of the Ramsey fringes for different ground state populations P_0 and assuming a thermal distribution. The contrast is normalized to compensate the decoherence that occurs without imbalancing the lattice. The distribution of atoms is limited to the five lowest vibrational levels. From this plot we learn that we implement the parity operator with a hold time of $t_{hold} = 65.4\mu s$.

trapping frequency. Now we investigate how the (differential) trap depth needs to be changed dynamically. An example ramp of the potentials is shown in figure 4.2(a). The initial trap depth is 18 µK, which corresponds to a trap frequency of $\omega = 2\pi\,55$ kHz. The trap frequency matches the larger of the two trapping frequencies that is currently used in the DQSIM experiment. The trap depth is increased sinusoidally within 15 µs and it is rebalanced after an adjustable hold time. The ramp duration is chosen large enough to make the ramp adiabatic. The wave functions of the atoms are thus compressed into a smaller, more harmonic region, which improves the measurement fidelity. The trap depth is modulated between the two $\pi/2$ time of a Ramsey interferometer with an interrogation time to 400 µs. We vary the „hold time“ during which the lattice retains a fixed imbalance and record Ramsey fringes. If we prepare thermal ensembles of atoms then the contrast will drop and undergo periodic revivals as shown in figure 4.2(b). The hotter the atom cloud the stronger the loss in contrast. We observe that both the contrast and the period of the revival decreases as the ensemble gets hotter. This can be attributed to the anharmonicity of trap, which is limiting the fidelity of the parity measurement.

State preparation Different Fock states can be prepared by driving higher order sidebands after cooling the atomic ensemble into the motional ground state [91]. Being able to displace the state dependent potentials against each other allows us to couple different vibrational levels via microwave radiation [92]. We regularly displace the two lattices by 17 nm, which is about half the spatial uncertainty of the ground state, to are used to drive first order sideband transitions as part of resolved microwave sideband cooling (see section 2.5). Sideband transitions beyond the tenth order have been demonstrated in our one dimensional lattice experiment [91].

Measuring the Wigner function The Wigner function at the origin can be measured using the aforementioned potential ramps with a hold time of $\tau_{hold} = 65.5$ µs, that minimizes the Ramsey contrast of a thermal ensemble. Figure 4.3(b) shows the phase evolution of the ten lowest Fock states. The differential

phase has a state independent contribution that stems from the differential trap depth $\Delta U = U_\uparrow - U_\downarrow$ and a state dependent one that stems from the differential eigenenergies. The Wigner function can be measured by tuning the phase φ of the second $\pi/2$-pulse to $\varphi = -\Phi(0)$ and projecting the internal state on $|\uparrow\rangle$]. The lowest five Fock states can be measured with a deviation of less than 0.05 as shown in figure 4.3(c). For small deviations the measurement error grows only in forth order with the phonon number, because we probe points close to the north- and south pole of the Bloch sphere. Beyond the seventh Fock state the measurement error rises sharply and the sign of the Wigner function is no longer measured reliably. This is a promising result, given the fact that only 14 bound states exist for the chosen initial trap depth.

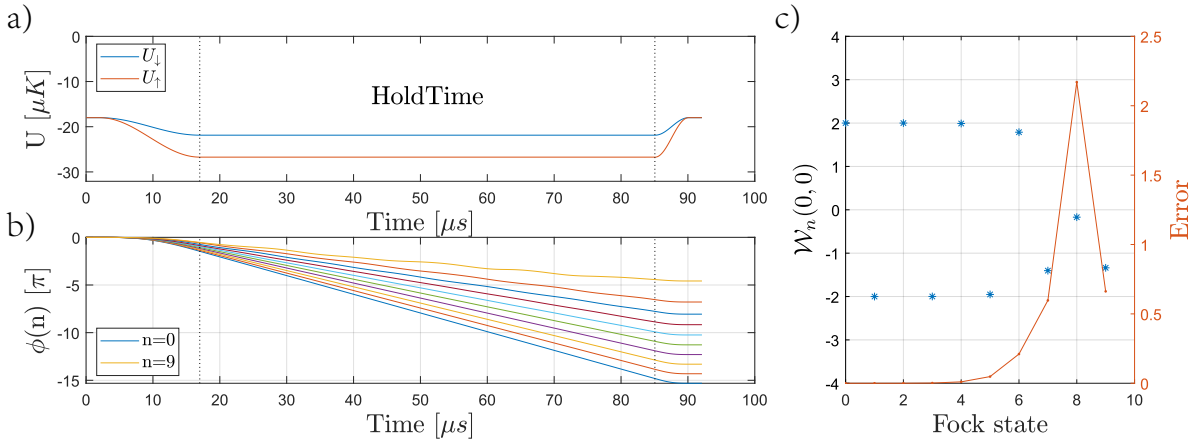

Figure 4.3: Measuring the Wigner function at the origin. a) The state dependent potentials are lowered adiabatically to induce a differential trapping frequency. After an adjustable hold time the trap is rebalanced again. b) Shows the time evolution of the differential phase between the two qubit states. We see that the lowest nine vibrational levels undergo an adiabatic evolution. The atoms acquire not only a phonon dependent differential phase, but also a phonon independent one, that is 15 times larger and stems from the differential trap depth $\Delta U = U_\uparrow - U_\downarrow$. c) Measured Wigner function (blue) and deviation from the predicted value (red).

I conclude this subsection with describing how the measurement can be visualized in phase space. The state of the atom is described by its Wigner function. The first $\pi/2$-pulse creates two copies of this distribution that are both subsequently displaced in phase-space. The change in trap depth will squeeze both distributions, but to a different amount. They will hence acquire a differential rotation speed. The trap is rebalanced in such a way that the two copies will have acquired a differential phase of either 0 or π depending on their parity. The second $\pi/2$ pulse is used to measure the overlap.
Using the phase space representation of the vibrational state makes it easy to understand the difference between the lattice potential and the harmonic approximation. We recall that the dynamics of a single quantum particle resemble the evolution of a statistical ensemble of classical particles. In a harmonic potential the Wigner function undergoes a rigid rotation. This renders the measurement insensitive to the implementation of the parity operator. It does not matter whether the atoms are squeezed or whether they are adiabatically compressed. It is also irrelevant whether the imbalance of the potentials is made stronger and shorter or weaker and longer.
This is in stark contrast to the anharmonic lattice potential where the curvature of the trap depends on the displacement from the origin. This gives rise to position dependent angular velocities that cause the Wigner function to disperse. Thus, it is preferable to compress the atom adiabatically into the harmonic region by increasing the trap depth slowly and as much as possible given the available laser power. It is also preferable to unbalance the lattice as late and as little as possible. This way the dispersion of both Wigner distributions is mostly common mode.

The periodic structure of the lattice potential fundamentally limits the area in phase space that can be explored. The restoring force of the lattice changes sign at displacement of half the lattice constant. The finite depth of the trap limits the displacement along the momentum axis. This will be discussed in the following.

4.3 State Reconstruction

The motional state of the atom can be reconstructed by measuring the Wigner function not only at the origin also for non-vanishing displacements in phase space. In this section, I discuss how to implement the displacement operator and the reconstruction of vibrational states.

Implementing the displacement operators The experiment at hand is ideally suited to displace atoms in phase space. As mentioned earlier we can shift the lattice potential to displace both the position and the momentum of the atoms. Our polarization synthesizer allows us to control the position of the both state dependent potentials [75]. A sudden position-jump of the lattice corresponds to a displacement in space and linear phase ramp to a shift of the momentum. The sudden position jumps must be fast relative to the oscillation period of the atom, which is given as the inverse of the trap frequency $1/\nu_{trap} = 1/55\,\mathrm{kHz} = 18.2\,\mu\mathrm{s}$. The feedback bandwidth of our FPGA based digital control of the position is in the order of 100 kHz but we can use additive feed forward control to change the lattice position within 300 ns [78].

Probing the Wigner function for non-vanishing displacements I performed a simulation to investigate how well the first five Fock states can be reconstructed for non-vanishing displacements in phase space. The results look very promising and are shown in figures 4.4 and 4.5. In figure 4.4 the calculated and the reconstructed Wigner function for n=0 and n=4 are shown side by side. The displacements in phase-space are normalized using the spatial and the momentum uncertainty of the wave function of the ground state in the harmonic approximation

$$\begin{aligned} x_0 &= \sqrt{\hbar/2m_{Cs}\omega} \\ p_0 &= \sqrt{\hbar m_{Cs}\omega/2} = \hbar/(2x_0)\,. \end{aligned} \tag{4.13}$$

The Wigner function of both the ground state and the forth excited state can be measured almost perfectly as long as the displacement is smaller than three times the ground state uncertainty. For n=4 the measured Wigner function does not approach zero for larger displacements. This can be attributed to the anharmonicity of the lattice potential. As a cross check, I repeated the simulation for a harmonic potential as well. In the harmonic approximation the reconstruction fidelity is only limited by discretization noise. Figure 4.4 also shows the two states after a displacement of $\Delta x = 2\Delta x_0$. The gray dashed line indicates the harmonic approximation, we observe that a displacement of $\Delta x = 4\Delta x_0$ corresponds to nearly a quarter of a lattice constant and at this displacement that a significant fraction of the state n=4 is shifted into the adjacent lattice site.

We can normalize the displacements to the lattice constant to highlight how the anharmonicity of the lattice potential and the finite extent of each potential well limits the reconstruction fidelity for non-vanishing displacements in phase space (see figure 4.5). We observe that the measurement fidelity

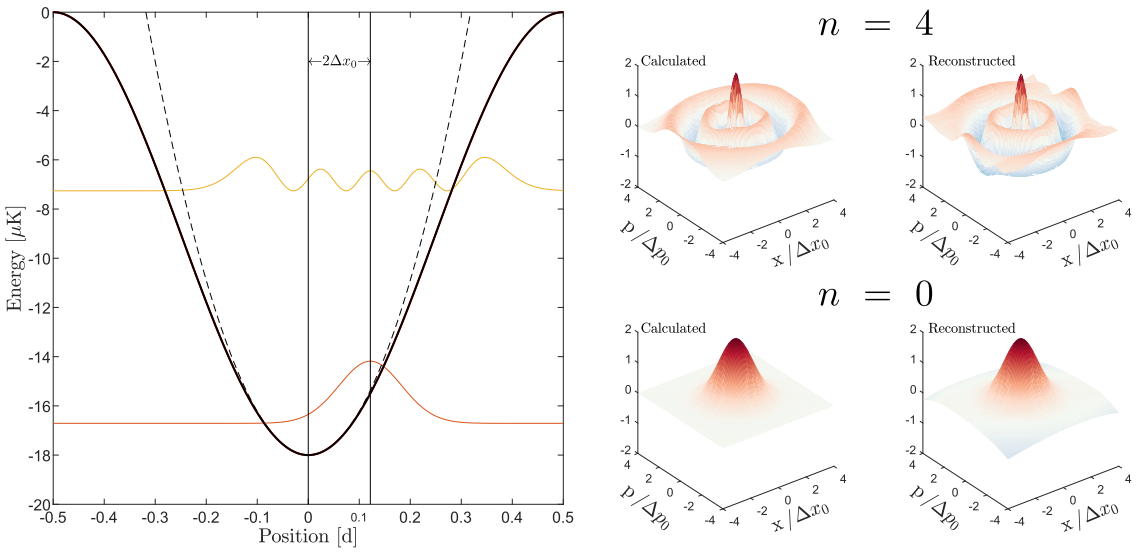

Figure 4.4: Measuring the Wigner function for $n = 0$ and $n = 4$. (left) The wavefunction of the displaced Fock states are shown. The lattice potential (solid black curve) and the harmonic approximation (dashed black line) are shown. The size of the spatial uncertainty of the ground state Δx_0 is indicated by the two vertical lines. (right) Comparison between the calculated Wigner function and the (simulated) measurement.

depends on both the displacement in phase space and the size of the wave function. The larger the Fock state the smaller the region in phase space within which its Wigner function can be accurately measured. Let us now consider how the modulation bandwidth of the lattice position affect the measurement fidelity.

The effect of finite system bandwidth So far I have assumed the phase ramps to be modulated within the bandwidth possible with feed forward control. With feed-forward control we can adjust the position within 300 ns, as discussed in section 2.4.3. As a cross check we can initialize the wave package in a displaced state. The results agree within the errors arising from the finite discretization. When the spatial displacement operator is carried out slowly (e.g. within 2 μs), then the atom gets accelerated. This is equivalent to transferring momentum and the reconstructed Wigner function is deformed as shown in figure 4.6. It is elongated along one angle bisector where the transferred momenta from the slow displacement ramp and the linear transport ramp partially compensate each other and reduced along the other where they add. We conclude that additive phase feed forward control of the position is required to reconstruct the Wigner function.

Changing the initial trap depth Intuitively we assume that the measurement fidelity improves, if we increase the trap depth. In a deeper trap the atoms exhibit a smaller spatial uncertainty, which reduces the absolute value of the displacements needed. However, the momentum uncertainty of each Fock state is increased, making it necessary to displace them by larger momenta. The atoms will be transported faster, and travel a longer distance during the parity operation. This makes the measurement susceptible to the finite extent of the dipole trap. Typical transport distances are 5 μm, which is negligible if the experiment is carried out in a lattice that is formed by two counter propagating beams. The trap depth does not change significantly, because the Rayleigh length is over 1 mm [146]. The extent of the two dimensional lattice in the DQSIM experiment is however limited by the horizontal waist w =75 μm of the horizontal beams. The finite extent of the trap can be accounted for by modulating the trap depth

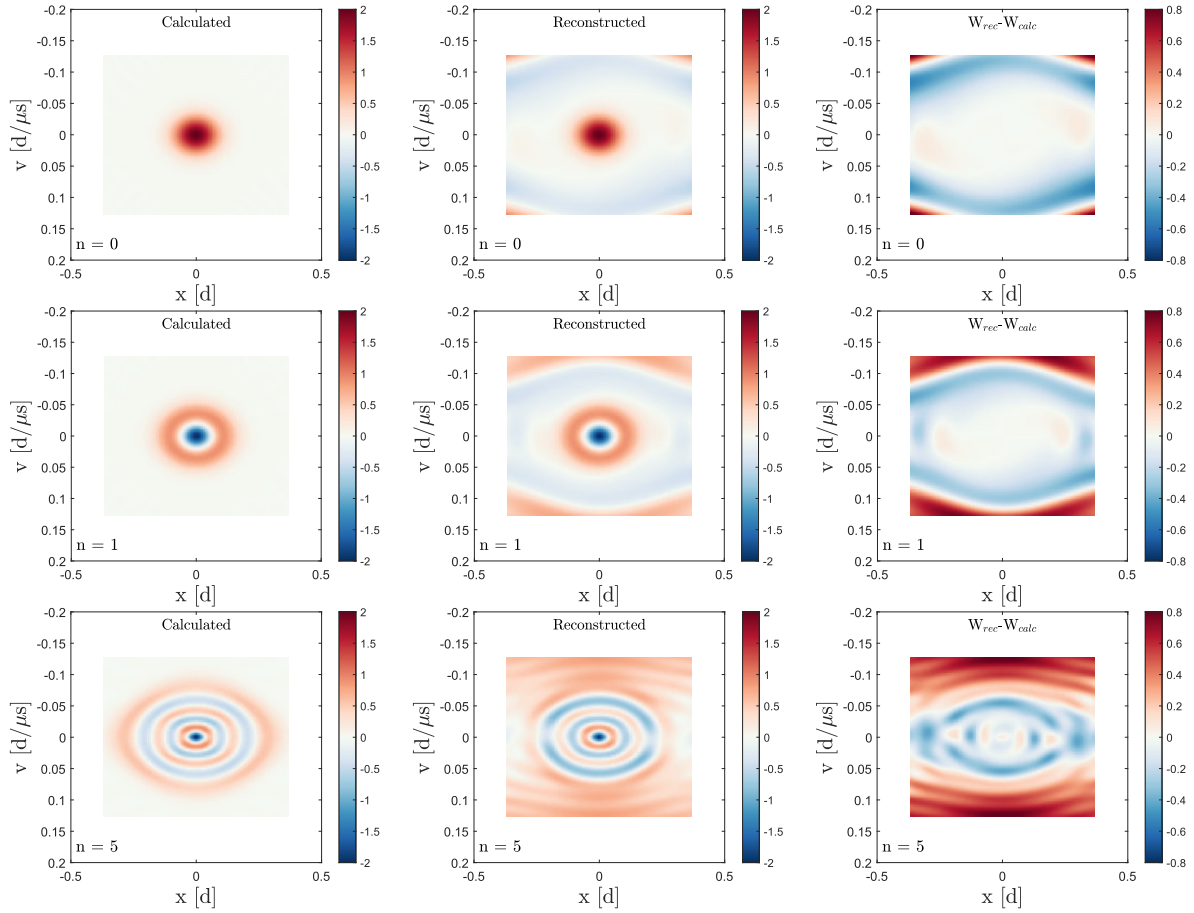

Figure 4.5: Calculated and reconstructed Wigner function. The displacements are normalized to the lattice constant d to highlight how the anharmonicity of the lattice potential and the finite extent of each potential well limits the reconstruction fidelity for non-vanishing displacements in phase space. The area within which the Wigner function is measured accurately shrinks as the phonon number increases.

during the (simulated) transport. I did not find any significant deviation for a transport distance of 5 µm. It should be noted that the transport distance can be reduced by introducing a larger imbalance between two state dependent potentials.

The sensitivity of the measurement to variations of the trap depth depends on the ratio between the two contributions to the differential phase

$$R := \frac{\Delta U}{\hbar \Delta\omega} = 2\pi \sqrt{\frac{2 \cdot U_0 \mathscr{A}}{m_{Cs} \lambda^2}} \left(\sqrt{1+\epsilon'} + \sqrt{1-\epsilon'} \right) \approx 15. \tag{4.14}$$

Here we use the parametrization $U_{\uparrow/\downarrow} = U_0 \mathscr{A}(1 \pm \epsilon')$ where $U_0 \mathscr{A}$ is the average trap depth, $\mathscr{A}$ is the relative change of trap depth and

$$\epsilon' = \frac{U_\uparrow - U_\downarrow}{U_\uparrow + U_\downarrow} \tag{4.15}$$

is the related to the differential trap depth ΔU via $\Delta U = -2U_0 \mathscr{A}\, \epsilon'$. The measurement becomes more sensitive to spatial variations of the total trap depth, if the initial trap depth U_0 is increased. We can

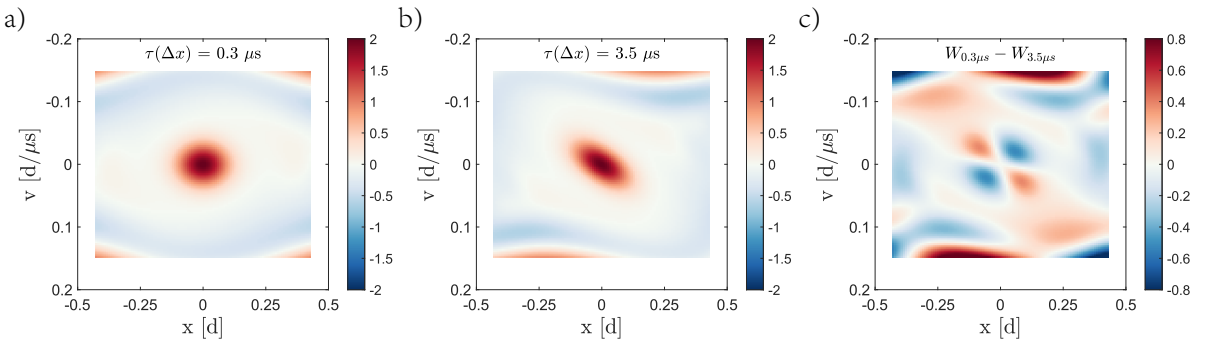

Figure 4.6: The reconstruction fidelity depends on system bandwidth. If we compare the Wigner function with feed forward control of the lattice position (a) and without (b). The shifting the lattice position slowly causes a rotation-dilation of the measured Wigner function that can be attributed to a non-vanishing momentum transfer.

reduce spatial variations by performing plane selection and restricting the measurement to a small area in the center of the trap. On the hand we increase the measurement fidelity by increasing the initial trap depth U_0 or the relative change of depth $\mathscr{A}$ because the atomic wave function gets compressed into the harmonic region of the trap. But only within the limitations imposed by the finite extent of the dipole trap.

Two dimensional Wigner function So far we have considered the one dimensional systems. We assumed that the atoms share the same quantum numbers along the remaining two directions. This can be done if the atoms are cooled into the motional ground state. We also assume that the we only change the trapping potential along one dimension. This is the case if the trap is comprised of a one dimensional state dependent potential and the confinement along the transverse directions is provided by a repulsive hollow beam potential. This type of trap is very homogeneous since its spatial extent is not limited by the waist of a transverse beam, but by its Rayleigh length of >1 mm.

In the DQSIM experiment both horizontal trapping frequencies are changed simultaneously. The question arises, whether we can still measure the parity. In a two dimensional system we distinguish between the parity with respect to to one line and the parity with respect to one point. The latter case corresponds to the parity of the two dimensional wave function.
The lattice potential is created from the interference of three beams. Two are counter propagating and one has an orthogonal direction. The lattice structure is a simple square grid with elliptic unit cells. If all three beam have the same intensity, then the unit cell is elliptic and the eccentricity can be computed from the two trapping frequencies

$$e = \frac{\omega'_y}{\omega'_x}. \tag{4.16}$$

Here y' denotes the direction along the counter-propagating beams and x' along the orthogonal one. The trapping frequencies have been measured using microwave spectroscopy [31] and the result is shown in figure 4.7. We observe that the eccentricity depends on the balance between the three beams. If all three beams have equal intensity – as is the case in the center of the trap – then the eccentricity is $e = \sqrt{3}$. The differential phase ψ_{n_x,n_y,n_z} that is acquired during the Ramsey interrogation time will depend on both vibrational quantum numbers. In the harmonic approximation we can compute the phonon-dependent contribution to be

$$\begin{aligned} \phi_{n_x,n_y,n_z}(t) &= \sum_{j\in\{x,y,z\}} \left(\tfrac{1}{2}+n_j\right)\cdot\int_0^t \mathrm{d}\tau\,\Delta\omega_j(\tau) \quad +\phi_{\mathrm{R}}(t) \\ &= \left[\left(\tfrac{1}{2}+n_x\right)+\sqrt{3}\left(\tfrac{1}{2}+n_y\right)\right]\cdot\int_0^t \mathrm{d}\tau\,\Delta\omega_x(\tau) \quad +\phi_{\mathrm{R}}(t). \end{aligned} \tag{4.17}$$

It follows that equation 4.7 can not be fulfilled for both axes simultaneously, hence the eccentricity of our unit cell prevents us from measuring the parity along x and y simultaneously.

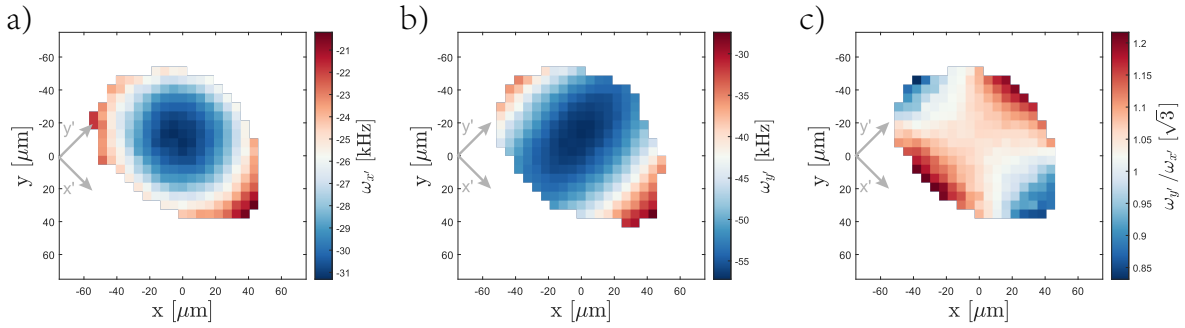

Figure 4.7: Spatial distribution of horizontal trapping frequencies ω and their ratio. The trapping frequency is more homogeneous along the direction of the counter propagating beams y'. The eccentricity of the potential wells ϵ is equal to the ratio of the trapping frequencies. Figures (a) and (b) are adapted from [31].

We can also tune the eccentricity e of the unit cell by changing the ratio of power in our counter propagating beams and the orthogonal one. As we reduce the power in the perpendicular beam the eccentricity will increase as the lattice transforms into a set of stripes. As we increase the power of H-beam 2 the eccentricity will approach one. It is in principle possible to measure the two dimensional parity if one trapping frequency is an odd integer multiple of the other.
A one-dimensional measurement of the Wigner function should be attempted first along the direction of the two counter propagating beams, since the trapping frequency is more homogeneous. The modulation of both the total trap depth and the trapping frequency limits our ability to the Wigner function in very deep lattices, because larger displacements in momentum space will increase the transport speed, hence the transport distance. We can improve the reconstruction fidelity either by reducing the transport distance during the parity measurement or by by expanding the lattice beams and increasing the total optical power. The former can be achieved by increasing the imbalance of the state dependent potential during the parity measurement. This increases the differential trapping frequency $\Delta\omega$ and reduces the duration of the parity measurement. The latter is possible because our TiSa laser system can deliver four times more power than we are currently using (See section 2.3.2).

4.4 Conclusion

I have presented and numerically investigated a novel scheme to reconstruct the vibrational state of neutral atoms in an optical lattice by directly measuring the Wigner distribution. Further, I showed that feedforward control of the lattice position is needed to realize a displacement operation without transferring momentum to the atom. A one dimensional lattice formed by two counter-propagating beam is the ideal platform to directly measure the Wigner function. It should however be possible to measure the Wigner function in the two-dimensional lattice of the DQSIM laboratory.

The proposed scheme bears close resemblance to a technique proposed by Lutterbach and Davidovich [126]. They proposed to use Ramsey interferometry to directly measure the Wigner function of ions

(by driving first order motional sidebands) and photons (by letting Rydberg atoms experience a light shift). This scheme was experimentally realized for microwave cavities in the group of Serge Haroche to measure the Wigner function of the first two Fock states [20, 127].

Our methods differs not only by the choice of platform but also we employ the atom as its own meter, instead of using an auxiliary particle. The measurement fidelity is limited by non-linearities that arise from the anharmonicity of the lattice potential, the finite size of each potential well and the finite extent of the dipole trap. Non-linear interactions between the Rydberg atoms and the cavity modes limit the fidelity when directly measuring the Wigner function of higher order Fock states in cavities [147]. Tomographic methods were employed to compensate this and to reconstruct the Wigner function for Fock states up to $n = 4$.

The simulation presented in this chapter suggest, that the proposed physical implementation of the parity operator is robust enough to measure the Wigner function for the lowest five Fock states directly.

CHAPTER 5

Conclusion and outlook

This thesis presents my contribution to the discrete-time quantum simulator (DQSIM) experiment. Neutral atoms are trapped in a three-dimensional optical lattice below a high numerical objective lens that is capable of resolving the spatial distribution with single site precision [8]. The experiment is designed to enable two-dimensional state-dependent transport of atoms [5], with the goal of realizing two-dimensional discrete-time quantum walks [6] and multi-particle entanglement [7].

In chapter 2, I described the experimental setup in general and the improvements I implemented in detail. The aforementioned discrete-time quantum walks must be performed within the coherence time of atoms in the optical lattice. I was able to improve the coherence time of free-falling atoms beyond 1 ms by designing and installing a current-stealing circuit as described in section 2.2. The fluctuations of the magnetic guiding field were reduced to the level of 1 ppm, which suggest that spin dephasing times of several tens of ms are possible once we have reduced other sources of decoherence, such as the vertical extent of the atomic ensemble.

Additional decoherence mechanism occur in optical lattices, where we measure coherence times of up to 1 ms. In our case, both circular polarization components are controlled and stabilized independently. For this reason, the intensity noise of each component induces fluctuations of the polarization ellipticity, which lead to time-varying differential light shifts. The input noise of the digital feedback controller is converted into intensity noise. Without pre-amplification, the low-frequency drifts of the input bias voltage limit the coherence time to 2 ms. I reduced this effect 20-fold by improving the design of our custom low-noise amplified photodiodes. Moreover, the intensity noise of the optical lattice beams is reduced to the shot-noise level for frequencies above 1 kHz.

We use two polarization synthesizers to control the position and depth of our spin-dependent optical lattice. Digital hardware containing FPGAs is used to integrate multiple feedback loops in a compact device. This hardware is, however, not only noisier but also slower than state-of-the-art analog controllers. We compensate the input noise with sufficient amplification and have implemented feedforward control to increase the modulation bandwidth to the limit imposed by the finite response time of the AOM.

Moreover, the computing power of the FPGA is utilized to realize additional features. We can freeze the intensity and the phase feedback, allowing us to release and recapture atoms into free fall. The non-linear response of the system is being compensated, allowing us to increase the dynamic range of the intensity control. We are only beginning to unlock the full range of processing capabilities of the FPGA. The internal data acquisition channels can be used to record step-responses. This will allow us to (auto) tune the feedback control without additional hardware.

To measure multi-particle interference, we have to confine the atomic ensemble to a single layer along

the imaging axis. In chapter 3, I presented a novel way to perform plane selection with light shifts that induce an artificial magnetic field. The switching times are much shorter, and negligible heat is dissipated compared to the established technique of using Zeeman shifts. I have demonstrated the preparation of thin volumes. With further careful adjustment of the experimental parameters, this technique will enable the selection of single planes.

In chapter 4, I propose a novel scheme to probe the Wigner function. This is a type of state-reconstruction as the Wigner function represents the density operator in phase space. The Wigner function can directly measured because it is proportional to the expectation value of the displaced parity operator. This measurement profits from the capabilities of our digital control system. Measuring the parity operator requires us to tune the lattice depth dynamically over a large range. Displacing the atoms purely in position space without transferring momentum requires fast modulation of the lattice position. Precise control over the vibrational degree of freedom is a prerequisite to preparing arbitrary states of motion, such as Fock states. I demonstrated Raman sideband cooling along the vertical direction using the D1 transition of cesium. This complements the microwave-mediated sideband-cooling that we use to cool horizontally.

Imaging lattice planes In the future, we plan to determine the vertical positions of the atoms not only spectroscopically but also optically. This is possible because the objective lens has a NA of 0.92, leading to a depth of focus, which is only half of one lattice site. The point-spread function can be engineered to evolve asymmetrically along the imaging axis [118], which will allow us to infer the vertical distribution of atoms from single images. Being able to distinguish atoms above and below the focal plane is highly desirable. We will exclude off-plane atoms from the analysis and directly detect and compensate for vertical shifts of the polarization gradient. If it moves upwards, more atoms above the target plane will survive the attempt of plane selection and vice versa if it moves downwards.

We also plan to increase the density of atoms in the center of the dipole trap. Before plane selection, the atom cloud extends over more than 40 vertical lattice sites, which leaves only a few percent of the atoms remaining afterwards. The atom cloud will be compressed using the release-retrap technique [9, 10, 119], as discussed in section 3.6. A theoretical investigation has shown that it should be possible to shrink the width of the ensemble to a few lattice sites, at which point the loading will be limited again by light-induced collisions.

Local spin rotations The experiments that have been discussed so far study single particles and employ global spin rotations. In the future, we plan to use the high resolution of our objective lens to implement local spin rotations with single-site resolution. We can achieve this by projecting Raman lasers with suitable intensity patterns through the objective lens onto the atoms. These patterns can be generated using a spatial light modulator in conjunction with the high numerical aperture of our objective lens. We have characterized a spatial light modulator and studied both holographic, and methods of direct imaging [120, 121]. I have summarized my contribution to this development in appendix C. Addressing the spin with single-site resolution will open the path to a plethora of new experiments, which I showcase with three examples.

Firstly, we can use position-dependent addressing of internal spins in combination with state-dependent transport to implement quantum logic gates [32]. We have demonstrated the interference between two bosonic atoms in our one-dimensional state-dependent optical lattice [29]. This creates entanglement between different particles and thus serves as a fundamental building block for quantum computing. Roos et al. [7] proposed a direct measurement of the exchange particle between two indistinguishable particles. A two-atom Ramsey-like interferometer is used to entangle a pair of distant atoms that will acquire a

phase of 0 if they are Bosons and a phase of π if they are Fermions. In a two-dimensional system, the atoms can swap positions without ever meeting.

Secondly, we can create multi-particle entanglement using low-entropy states. Low entropy states with unity filling factor have been realized in our one-dimensional system and can be efficiently implemented in two dimensions [122]. The creation of low entropy states opens the path to study many-particle phenomena, such as simulating quantum spin liquids [123, 124] and highly entangled cluster states [30], and quantum correlations in many-body systems [85, 148].

Finally, Sajid et al. [11] proposed an experiment to simulate artificial magnetic fields. While one-dimensional systems can be used to simulate and study artificial electrical fields [28], simulating magnetic fields requires at least two dimensions.

I believe, that the results and techniques presented in this thesis enable exciting further research in the DQSIM experiment.

Bibliography

[1] A. de Touzalin, C. Marcus, F. Heijman, I. Cirac, R. Murray and T. Calarco, "Quantum Manifesto", May (2016) 1 (cit. on pp. v, 1).

[2] A. Celi, A. Sanpera, V. Ahufinger and M. Lewenstein, "Quantum optics and frontiers of physics: The third quantum revolution", Physica Scripta 92.1 (2017) 1, ISSN: 14024896, arXiv: 1601.04616 (cit. on pp. v, 1).

[3] J. P. Dowling and G. J. Milburn, "Quantum technology: The second quantum revolution", Philosophical Transactions of the Royal Society A: Mathematical, Physical and Engineering Sciences 361.1809 (2003) 1655, ISSN: 1364503X, arXiv: 0206091 [quant-ph] (cit. on pp. v, 1).

[4] M. A. Nielsen and I. L. Chuang, *Quantum Computation and Quantum Information*, vol. 52, 6, Cambridge University Press, 2010 702, ISBN: 9781107002173 (cit. on pp. v, 1, 16, 35).

[5] Stefan Brakhane, "The Quantum Walk Microscope", Dissertation: Bonn, 2016 (cit. on pp. v, 3, 13, 17, 18, 20, 35, 38, 69, 88).

[6] T. Groh, S. Brakhane, W. Alt, D. Meschede, J. K. Asbóth and A. Alberti, "Robustness of topologically protected edge states in quantum walk experiments with neutral atoms", Physical Review A 94.1 (2016) 1, ISSN: 24699934, arXiv: 1605.03633 (cit. on pp. v, 1, 17, 19, 69, 92).

[7] C. F. Roos, A. Alberti, D. Meschede, P. Hauke and H. Häffner, "Revealing Quantum Statistics with a Pair of Distant Atoms", Physical Review Letters 119.16 (2017) 1, ISSN: 10797114, arXiv: 1706.04231 (cit. on pp. v, 1, 69, 70).

[8] C. Robens, S. Brakhane, W. Alt, F. Kleißler, D. Meschede, G. Moon, G. Ramola and A. Alberti, "High numerical aperture (NA = 092) objective lens for imaging and addressing of cold atoms", Optics Letters 42.6 (2017) 1043, ISSN: 0146-9592, arXiv: 1611.02159 (cit. on pp. v, 1, 8, 18, 19, 27, 69).

[9] M. T. De Pue, C. Mc Cormick, S. L. Winoto, S. Oliver and D. S. Weiss, "Unity occupation of sites in a 3D optical lattice", Physical Review Letters 82.11 (1999) 2262, ISSN: 10797114 (cit. on pp. v, 55, 70).

[10] J. Hu, A. Urvoy, Z. Vendeiro, V. Crépel, W. Chen and V. Vuletić, "Creation of a Bose-condensed gas of 87Rb by laser cooling", Science 358.6366 (2017) 1078, ISSN: 10959203, arXiv: arXiv:1705.03421v1 (cit. on pp. v, 55, 70).

[11] M. Sajid, J. K. Asbóth, D. Meschede, R. F. Werner and A. Alberti, "Creating anomalous Floquet Chern insulators with magnetic quantum walks", Physical Review B 99.21 (2019) 1, ISSN: 24699969, arXiv: 1808.08923 (cit. on pp. v, 1, 71).

[12] C. Roos, T. Zeiger, H. Rohde, H. C. Nägerl, J. Eschner, D. Leibfried, F. Schmidt-Kaler and R. Blatt, "Quantum state engineering on an optical transition and decoherence in a paul trap", Physical Review Letters 83.23 (1999) 4713, ISSN: 10797114, arXiv: 9909038 [quant-ph] (cit. on pp. v, 27).

[13] E. Schrödinger, "Are there quantum jumps? Part II", British Journal for the Philosophy of Science 3.12 (1953) 348, ISSN: 00070882 (cit. on p. 1).

[14] A. L. Schawlow and C. H. Townes, "Infrared and optical masers", Physical Review 112.6 (1958) 1940, ISSN: 0031899X (cit. on p. 1).

[15] T. Maiman, "Stimulated Optical Radiation in Ruby", Nature 187.4736 (1960) 493 (cit. on p. 1).

[16] W. Becker, "Eine neue Molekularpumpe", VakuumTechnik 7 (1958) 149 (cit. on p. 1).

[17] K. Jousten, *Handbuch Vakuumtechnik*, 12th ed., Springer Reference Technik, 2018 1138, ISBN: 9783658133856 (cit. on p. 1).

[18] W. Paul, O. Osberghaus and E. Fischer, *Ein Ionenkäfig*, VS Verlag für Sozialwissenschaften, 1958, ISBN: 9783663035008 (cit. on p. 1).

[19] D. Meschede, H. Walther and G. Müller, "One-atom maser", Physical Review Letters 54.6 (1985) 551, ISSN: 00319007 (cit. on p. 1).

[20] G. Nogues, A. Rauschenbeutel, S. Osnaghi, P. Bertet, M. Brune, J. M. Raimond, S. Haroche, L. G. Lutterbach and L. Davidovich, "Measurement of a negative value for the Wigner function of radiation", Physical Review A - Atomic, Molecular, and Optical Physics 62.5 (2000) 054101, ISSN: 10502947 (cit. on pp. 1, 57, 68).

[21] S. Chu, J. E. Bjorkholm, A. Ashkin and A. Cable, "Experimental Observation of Optically Trapped Atoms", Phys. Rev. Lett. 57.3 (1986) 314 (cit. on p. 1).

[22] N. Gisin and R. Thew, "Quantum communication", Nature Photonics 1.3 (2007) 165 (cit. on p. 1).

[23] S. Pirandola, U. L. Andersen, L. Banchi, M. Berta, D. Bunandar, R. Colbeck, D. Englund, T. Gehring, C. Lupo, C. Ottaviani, J. L. Pereira, M. Razavi, J. Shamsul Shaari, M. Tomamichel, V. C. Usenko, G. Vallone, P. Villoresi and P. Wallden, "Advances in quantum cryptography", Advances in Optics and Photonics 12.4 (2020) 1012, ISSN: 1943-8206, arXiv: 1906.01645 (cit. on p. 1).

[24] I. H. Deutsch, G. K. Brennen and P. S. Jessen, "Quantum computing with neutral atoms in an optical lattice", *Fortschritte der Physik*, vol. 48, 9-11, 2000 155, ISBN: 3527403213 (cit. on p. 1).

[25] R. Blatt and C. F. Roos, "Quantum simulations with trapped ions", Nature Physics 8.4 (2012) 277, ISSN: 17452473 (cit. on p. 1).

[26] T. Udem, R. Holzwarth and T. W. Hänsch, "Optical frequency metrology", Nature 416.6877 (2002) 233, ISSN: 00280836 (cit. on p. 1).

[27] C. L. Degen, F. Reinhard and P. Cappellaro, "Quantum sensing", Reviews of Modern Physics 89.3 (2017) 1, ISSN: 15390756, arXiv: 1611.02427 (cit. on p. 1).

[28] M. Genske, W. Alt, A. Steffen, A. H. Werner, R. F. Werner, D. Meschede and A. Alberti, "Electric quantum walks with individual atoms", Physical Review Letters 110.19 (2013) 1, ISSN: 00319007, arXiv: 1302.2094 (cit. on pp. 1, 71).

[29] C. Robens, S. Brakhane, D. Meschede and A. Alberti, "Quantum Walks with Neutral Atoms: Quantum Interference Effects of One and Two Particles", arXiv (2016) 1, arXiv: 1511.03569 (cit. on pp. 1, 21, 70).

[30] O. Mandel, M. Greiner, A. Widera, T. Rom, T. W. Hänsch and I. Bloch, "Controlled collisions for multi-particle entanglement of optically trapped atoms", Nature 425.6961 (2003) 937, ISSN: 00280836, arXiv: 0308080 [arXiv:quant-ph] (cit. on pp. 1, 56, 71).

[31] G. Ramola, "Ramsey Imaging of Optical Dipole Traps", Dissertation: Universität Bonn, 2021, arXiv: 2106.05871 (cit. on pp. 1, 3, 4, 7, 11, 16, 18, 19, 21–23, 27, 29, 31, 40, 50–52, 56, 59, 66, 67).

[32] J. Kempe, "Quantum random walks An introductory overview", Contemporary Physics 44.4 (2003) 307, ISSN: 00107514, arXiv: 0303081 [quant-ph] (cit. on pp. 1, 70).

[33] A. Royer, "Wigner function as the expectation value of a parity operator", 15.2 (1977) 15 (cit. on pp. 2, 57, 58).

[34] M. Martinez-Dorantes, W. Alt, J. Gallego, S. Ghosh, L. Ratschbacher and D. Meschede, "State-dependent fluorescence of neutral atoms in optical potentials", Physical Review A 97.2 (2018) 1, ISSN: 24699934, arXiv: 1710.07964 (cit. on p. 4).

[35] J. E. Bjorkholm, "Collision-limited lifetimes of atom traps", Physical Review A 38.3 (1988) 1599, ISSN: 10502947 (cit. on p. 4).

[36] T. Klostermann, C. R. Cabrera, H. von Raven, J. F. Wienand, C. Schweizer, I. Bloch and M. Aidelsburger, "Fast long-distance transport of cold cesium atoms", arXiv (2021), arXiv: 2109.03804 (cit. on p. 4).

[37] S. Brakhane and A. Alberti, "Technical Note: Stress-Induced Birefringence in Vacuum Systems", (2016) 6 (cit. on pp. 5, 19).

[38] S. Brakhane, W. Alt, D. Meschede, C. Robens, G. Moon and A. Alberti, "Note: Ultra-low birefringence dodecagonal vacuum glass cell", Review of Scientific Instruments 86.12 (2015) 1, ISSN: 10897623, arXiv: 1512.02396 (cit. on p. 4).

[39] A. Steffen, W. Alt, M. Genske, D. Meschede, C. Robens and A. Alberti, "Note: In situ measurement of vacuum window birefringence by atomic spectroscopy", Review of Scientific Instruments 84.12 (2013) 1, ISSN: 00346748, arXiv: 1308.4959 (cit. on pp. 4, 18, 37).

[40] E. L. Raab, M. Prentiss, A. Cable, S. Chu and D. E. Pritchard, "Trapping of Neutral Sodium Atoms with Radiation Pressure", Physical Review Letters 59.23 (1987) 2631, ISSN: 00319007 (cit. on p. 5).

[41] A. L. Schawlow and T. W. Hänsch, "Cooling of gases by laser radiation", Optics Communications 13.1 (1975) 68 (cit. on p. 5).

[42] D. J. Wineland, R. E. Drullinger and F. L. Walls,
"Radiation-pressure cooling of bound resonant absorbers",
Physical Review Letters 40.25 (1978) 1639, ISSN: 00319007 (cit. on p. 5).

[43] H. J. Metcalf and P. van der Straten, "Laser cooling and trapping of atoms",
J. Opt. Soc. Am. B 20 (2003) 887, ISSN: 0098-907X (cit. on p. 5).

[44] S. Chu, L. Hollberg, J. E. Bjorkholm, A. Cable and A. Ashkin,
"Three-dimensional viscous confinement and cooling of atoms by resonance radiation pressure",
Physical Review Letters 55.1 (1985) 48, ISSN: 00319007 (cit. on p. 6).

[45] P. D. Lett, R. N. Watts, C. I. Westbrook, W. D. Phillips, P. L. Gould and H. J. Metcalf,
"Observation of atoms laser cooled below the doppler limit",
Physical Review Letters 61.2 (1988) 169, ISSN: 00319007 (cit. on p. 6).

[46] J. Dalibard and C. Cohen-Tannoudji,
"Laser cooling below the Doppler limit by polarization gradients: simple theoretical models",
Journal of the Optical Society of America B 6.11 (1989) 2023, ISSN: 0740-3224
(cit. on pp. 6, 36).

[47] D. S. Weiss, E. Riis, Y. Shevy, P. J. Ungar and S. Chu,
"Optical molasses and multilevel atoms: experiment",
Journal of the Optical Society of America B 6.11 (1989) 2072, ISSN: 0740-3224 (cit. on p. 6).

[48] C. N. Cohen-Tannoudji and W. D. Phillips, "New mechanisms for laser cooling",
Physics Today 43.10 (1990) 33, ISSN: 19450699 (cit. on pp. 6, 7).

[49] C. Salomo, J. Dalibard, W. D. Phillip, A. Clairon and S. Guellat,
"Laser cooling of cesium atoms below 3uk", Epl 12.8 (1990) 683, ISSN: 12864854 (cit. on p. 6).

[50] P. v. d. S. Harold J. Metcalf, *Laser cooling and trapping*, vol. 2nd, Springer, 2001 344,
ISBN: 0387988920 (cit. on pp. 8, 51).

[51] R. P. Feynman, F. L. Vernon and R. W. Hellwarth,
"Geometrical Representation of the Schrödinger Equation for Solving Maser Problems",
Journal of Applied Physics 28.1 (1957) 49, ISSN: 00218979 (cit. on p. 8).

[52] N. F. Ramsey, "A molecular beam resonance method with separated oscillating fields",
Physical Review 78.6 (1950) 695, ISSN: 0031899X (cit. on p. 9).

[53] Ł. Cywiński, R. M. Lutchyn, C. P. Nave and S. Das Sarma,
"How to enhance dephasing time in superconducting qubits",
Physical Review B - Condensed Matter and Materials Physics 77.17 (2008) 1, ISSN: 10980121,
arXiv: 0712.2225 (cit. on p. 9).

[54] S. Kuhr, W. Alt, D. Schrader, I. Dotsenko, Y. Miroshnychenko, A. Rauschenbeutel and
D. Meschede, "Analysis of dephasing mechanisms in a standing-wave dipole trap",
Physical Review A - Atomic, Molecular, and Optical Physics 72.2 (2005) 1, ISSN: 10502947,
arXiv: 0410037 [quant-ph] (cit. on pp. 9, 10, 18, 27, 36, 50, 51).

[55] D. Leibfried, R. Blatt, C. Monroe and D. Wineland, "Quantum dynamics of single trapped ions",
Reviews of Modern Physics 75.1 (2003) 281, ISSN: 00346861 (cit. on pp. 9, 31).

[56] E. L. Hahn, "Spin echoes", Physical Review 80.4 (1950) 580, ISSN: 0031899X
(cit. on pp. 10, 50).

[57] A. Alberti, W. Alt, R. Werner and D. Meschede, “Decoherence models for discrete-time quantum walks and their application to neutral atom experiments”, New Journal of Physics 16 (2014) 1, ISSN: 13672630, arXiv: 1409.6145 (cit. on pp. 10, 23).

[58] A. Blendl, “Study Of Decoherence E ff ects In Cold Atom Optical Lattices”, Master: Universität Bonn, 2019 (cit. on pp. 11, 14, 88).

[59] P. Horowitz and W. Hill, *The Art of Electronics*, 3rd ed., Cambridge University Press, 2015, ISBN: 978-0-521-80926-9 (cit. on p. 12).

[60] B. Merkel, K. Thirumalai, J. E. Tarlton, V. M. Schäfer, C. J. Ballance, T. P. Harty and D. M. Lucas, “Magnetic field stabilization system for atomic physics experiments”, Review of Scientific Instruments 90.4 (2019) 1, ISSN: 10897623, arXiv: 1808.03310 (cit. on pp. 12, 16).

[61] C. Robens, “Testing the quantumness of Atom Trajectories”, Dissertation: Universität Bonn, 2017 (cit. on pp. 15, 20, 21, 31, 34, 35, 53, 55).

[62] T. Ruster, C. T. Schmiegelow, H. Kaufmann, C. Warschburger, F. Schmidt-Kaler and U. G. Poschinger, “A long-lived Zeeman trapped-ion qubit”, Applied Physics B: Lasers and Optics 122.10 (2016) 1, ISSN: 09462171, arXiv: 1606.07220 (cit. on p. 16).

[63] F. Primdahl, “The fluxgate magnetometer”, Journal of Physics E: Scientific Instruments 12.4 (1979) (cit. on p. 16).

[64] P. Ripka, “Review of fluxgate sensors”, Sensors and Actuators: A. Physical 33.3 (1992) 129, ISSN: 09244247 (cit. on p. 16).

[65] R. Grimm, M. Weidemüller and Y. B. Ovchinnikov, *Optical Dipole Traps*, vol. 42, C, 2000 95, ISBN: 0120038420, arXiv: 9902072 [physics] (cit. on pp. 16, 17).

[66] W. Happer and B. S. Mathur, “Effective Operator Formalism in Optical Pumping”, Phys. Rev. 163.1 (1967) 12 (cit. on p. 17).

[67] P. S. Jessen and I. H. Deutsch, “Optical Lattices”, Advances in Atomic, Molecular and Optical Physics 37.C (1996) 95, ISSN: 1049250X (cit. on p. 17).

[68] F. Le Kien, P. Schneeweiss and A. Rauschenbeutel, “Dynamical polarizability of atoms in arbitrary light fields: General theory and application to cesium”, European Physical Journal D 67.5 (2013), ISSN: 14346060, arXiv: 1211.2673 (cit. on pp. 17, 18).

[69] W. Alt, “Optical control of single neutral atoms”, Dissertation: Bonn, 2004 132 (cit. on p. 18).

[70] G. Ramola, R. Winkelmann, K. Chandrashekara, W. Alt, X. Peng, D. Meschede and A. Alberti, “Ramsey imaging of optical traps”, Phys. Rev. Appl. 16 (2021) 24, arXiv: 2106.05871 (cit. on pp. 18, 34).

[71] P. Moulton, “Spectroscopic and laser characteristics of Ti:Al2O3”, J. Opt. Soc. Am. B 3.1 (1986) 125 (cit. on p. 19).

[72] P. Albers, E. Stark and G. Huber, “Continuous-wave laser operation and quantum efficiency of titanium-doped sapphire”, J. Opt. Soc. Am. B 3.1 (1986) 134, ISSN: 0740-3224 (cit. on p. 19).

[73] K. Chandrashekara,
"A High-Power Ti:Sa Laser System for Atomic Quantum Walks Experiments",
Master: Universität Bonn, 2020 75 (cit. on pp. 20, 50).

[74] X. Baillard, A. Gauguet, S. Bize, P. Lemonde, P. Laurent, A. Clairon and P. Rosenbusch,
"Interference-filter-stabilized external-cavity diode lasers",
Optics Communications 266.2 (2006) 609, ISSN: 00304018, arXiv: 0605046 [physics]
(cit. on pp. 20, 27).

[75] C. Robens, S. Brakhane, W. Alt, D. Meschede, J. Zopes and A. Alberti,
"Fast, High-Precision Optical Polarization Synthesizer for Ultracold-Atom Experiments",
Physical Review Applied 9.3 (2018) 34016, ISSN: 23317019, arXiv: 1611.07952
(cit. on pp. 21, 23, 25, 63).

[76] M. R. Lam, N. Peter, T. Groh, W. Alt, C. Robens, D. Meschede, A. Negretti, S. Montangero,
T. Calarco and A. Alberti,
"Demonstration of Quantum Brachistochrones between Distant States of an Atom",
Physical Review X 11.1 (2021) 11035, ISSN: 21603308, arXiv: 2009.02231 (cit. on pp. 21, 58).

[77] P. Du, "Optical Intensity Control Based on Digital and Analog Systems",
Master: Universität Bonn, 2018 (cit. on pp. 21, 25).

[78] M. Werninghaus,
"Controlling atom transport in a two-dimensional state-dependent optical lattice",
Master: Bonn, 2017 (cit. on pp. 22, 25, 63).

[79] M. Omar, "Atom cloud compression in a 3D optical lattice and laser intensity stabilisation using an in-house developed photodiode amplifier", Master: Universität Bonn, 2019
(cit. on pp. 23, 55, 87).

[80] D. F. Walls, "Squeezed states of light", Nature 306.5939 (1983) 141, ISSN: 00280836
(cit. on p. 24).

[81] S. Machida, Y. Yamamoto and Y. Itaya,
"Observation of amplitude squeezing in a constant-current–driven semiconductor laser",
Phys. Rev. Lett 58.10 (1987) 1000 (cit. on p. 24).

[82] S. F. Pereira, M. Xiao, H. J. Kimble and J. L. Hall,
"Generation of squeezed light by intracavity frequency doubling", Phys. Rev. A 38.9 (1988) 4931
(cit. on p. 24).

[83] K. J. Astrom and R. M. Murray, *Feedback systems, An introduction for Scientists and Engineers*,
illustrate, vol. 54, Princeton University Press, 2008 43, ISBN: 9780691135762 (cit. on p. 25).

[84] M. Greiner, O. Mandel, T. Rom, A. Altmeyer, A. Widera, T. W. Hänsch and I. Bloch,
"Quantum phase transition from a superfluid to a Mott insulator in an ultracold gas of atoms",
Nature 415 (2002) 39, ISSN: 09214526 (cit. on p. 27).

[85] R. Islam, R. Ma, P. M. Preiss, M. Eric Tai, A. Lukin, M. Rispoli and M. Greiner,
"Measuring entanglement entropy in a quantum many-body system", Nature 528.7580 (2015) 77,
ISSN: 14764687 (cit. on pp. 27, 71).

[86] L. Cacciapuoti, M. De Angelis, M. Fattori, G. Lamporesi, T. Petelski, M. Prevedelli, J. Stuhler
and G. M. Tino,
"Analog+digital phase and frequency detector for phase locking of diode lasers",
Review of Scientific Instruments 76.5 (2005), ISSN: 00346748 (cit. on p. 27).

[87] S. Hild, "Resolved Raman sideband cooling in a doughnut-shaped optical trap", Master: Universität Bonn, 2011 (cit. on p. 27).

[88] E. Brion, L. H. Pedersen and K. Mølmer, "Adiabatic elimination in a lambda system", Journal of Physics A: Mathematical and Theoretical 40.5 (2007) 1033, ISSN: 17518113, arXiv: 0610056 [quant-ph] (cit. on p. 28).

[89] D. A. Steck, *Quantum and Atom Optics*, 2019 (cit. on p. 28).

[90] W. Kohn, "Analytic properties of Bloch waves and Wannier functions", Physical Review 115.4 (1959) 809, ISSN: 0031899X (cit. on pp. 29, 60).

[91] L. Förster, M. Karski, J. M. Choi, A. Steffen, W. Alt, D. Meschede, A. Widera, E. Montano, J. H. Lee, W. Rakreungdet and P. S. Jessen, "Microwave control of atomic motion in optical lattices", Physical Review Letters 103.23 (2009) 1, ISSN: 00319007, arXiv: 0909.0678 (cit. on pp. 29, 55, 61).

[92] N. Belmechri, L. Förster, W. Alt, A. Widera, D. Meschede and A. Alberti, "Microwave control of atomic motional states in a spin-dependent optical lattice", Journal of Physics B: Atomic, Molecular and Optical Physics 46.10 (2013), ISSN: 09534075, arXiv: 1302.6208 (cit. on pp. 29, 61).

[93] P. F. Bernath, *Spectra of Atoms and Molecules*, Oxford University Press, 1995 405, ISBN: 0-19-507598-6 (cit. on p. 29).

[94] F. Mintert and C. Wunderlich, "Ion-trap quantum logic using long-wavelength radiation", Physical Review Letters 87.25 (2001) 257904–1–257904, ISSN: 10797114, arXiv: 0104041 [quant-ph] (cit. on p. 29).

[95] Q. A. Turchette, Kielpinski, B. E. King, D. Leibfried, D. M. Meekhof, C. J. Myatt, M. A. Rowe, C. A. Sackett, C. S. Wood, W. M. Itano, C. Monroe and D. J. Wineland, "Heating of trapped ions from the quantum ground state", Physical Review A - Atomic, Molecular, and Optical Physics 61.6 (2000) 8, ISSN: 10941622, arXiv: 0002040 [quant-ph] (cit. on p. 31).

[96] L. Förster, "Microwave control of atomic motion in a spin dependent optical lattice", Dissertation: Universität Bonn, 2010 1 (cit. on p. 32).

[97] J. Uckert, "Fast Raman transitions for Ramsey interferometry", Master: Universität Bonn, 2019 (cit. on p. 32).

[98] M. Karski, L. Förster, J. M. Choi, A. Steffen, N. Belmechri, W. Alt, D. Meschede and A. Widera, "Imprinting patterns of neutral atoms in an optical lattice using magnetic resonance techniques", New Journal of Physics 12 (2010) 1, ISSN: 13672630, arXiv: 0912.2517 (cit. on pp. 35, 38, 52, 53).

[99] S. P. Rath, T. Yefsah, K. J. Günter, M. Cheneau, R. Desbuquois, M. Holzmann, W. Krauth and J. Dalibard, "Equilibrium state of a trapped two-dimensional Bose gas", Physical Review A - Atomic, Molecular, and Optical Physics 82.1 (2010) 2, ISSN: 10502947, arXiv: 1003.4545 (cit. on pp. 35, 52).

[100] C. Weitenberg, "Single-Atom resolved imaging and manipulation of an atomic Mott insulator", PhD thesis, 2011 1 (cit. on pp. 35, 52, 53).

[101] E. Cocchi, L. A. Miller, J. H. Drewes, M. Koschorreck, D. Pertot, F. Brennecke and M. Köhl, "Equation of State of the Two-Dimensional Hubbard Model", Physical Review Letters 116.17 (2016) 1, ISSN: 10797114, arXiv: 1512.03431 (cit. on pp. 35, 52).

[102] G. J. Edge, R. Anderson, D. Jervis, D. C. McKay, R. Day, S. Trotzky and J. H. Thywissen, "Imaging and addressing of individual fermionic atoms in an optical lattice", Physical Review A - Atomic, Molecular, and Optical Physics 92.6 (2015) 1, ISSN: 10941622, arXiv: 1510.04744 (cit. on pp. 35, 52).

[103] A. Omran, M. Boll, T. A. Hilker, K. Kleinlein, G. Salomon, I. Bloch and C. Gross, "Microscopic Observation of Pauli Blocking in Degenerate Fermionic Lattice Gases", Physical Review Letters 115.26 (2015) 1, ISSN: 10797114, arXiv: 1510.04599 (cit. on pp. 35, 52, 53).

[104] N. L. Smith, W. H. Heathcote, G. Hechenblaikner, E. Nugent and C. J. Foot, "Quasi-2D confinement of a BEC in a combined optical and magnetic potential", Journal of Physics B: Atomic, Molecular and Optical Physics 38.3 (2005) 223, ISSN: 09534075, arXiv: 0410101 [cond-mat] (cit. on pp. 35, 53).

[105] J. L. Ville, T. Bienaimé, R. Saint-Jalm, L. Corman, M. Aidelsburger, L. Chomaz, K. Kleinlein, D. Perconte, S. Nascimbène, J. Dalibard and J. Beugnon, "Loading and compression of a single two-dimensional Bose gas in an optical accordion", Physical Review A 95.1 (2017) 1, ISSN: 24699934, arXiv: 1611.07681 (cit. on pp. 35, 53).

[106] A. Peng, "Quantum Gas Microscope With Optical Lattice", Dissertation: Havard University, 2010 1 (cit. on pp. 35, 53).

[107] D. Rychtarik, B. Engeser, H. C. Nägerl and R. Grimm, "Two-dimensional Bose-Einstein condensate in an optical surface trap", Physical Review Letters 92.17 (2004) 1, ISSN: 00319007, arXiv: 0309536 [cond-mat] (cit. on p. 35).

[108] T. S. Ross, *Laser beam quality metrics*, SPIE, 2013 2006, ISBN: 978-0-8194-9297-5 (cit. on p. 42).

[109] V. N. Mahajan, "Strehl Ratio for Primary Aberrations in Terms of Their Aberration Variance.", Journal of the Optical Society of America 73.6 (1983) 860, ISSN: 00303941 (cit. on p. 42).

[110] M. Guizar-Sicairos, S. T. Thurman and J. R. Fienup, "Efficient subpixel image registration algorithms", Optics Letters 33.2 (2008) 156, ISSN: 0146-9592, arXiv: 78 [0146-9592] (cit. on p. 49).

[111] M. F. Andersen, A. Kaplan and N. Davidson, "Echo Spectroscopy and Quantum Stability of Trapped Atoms", Physical Review Letters 90.2 (2003) 4, ISSN: 10797114, arXiv: 0208052 [quant-ph] (cit. on p. 50).

[112] S. Guérin, S. Thomas and H. R. Jauslin, "Optimization of population transfer by adiabatic passage", Physical Review A - Atomic, Molecular, and Optical Physics 65.2 (2002) 12, ISSN: 10941622 (cit. on pp. 51, 52).

[113] L. Allen and J. H. Eberly, *Optical resonance and two-level atoms*, 1975 (cit. on p. 51).

[114] C. R. Ekstrom, C. Kurtsiefer, D. Voigt, O. Dross, T. Pfau and J. Mlynek,
"Coherent excitation of a He beam observed in atomic momentum distributions",
Optics Communications 123.4-6 (1996) 505, ISSN: 00304018 (cit. on p. 51).

[115] M. Khudaverdyan, W. Alt, I. Dotsenko, L. Förster, S. Kuhr, D. Meschede, Y. Miroshnychenko, D. Schrader and A. Rauschenbeutel,
"Adiabatic quantum state manipulation of single trapped atoms",
Physical Review A - Atomic, Molecular, and Optical Physics 71.3 (2005) 2, ISSN: 10502947, arXiv: 0411120 [quant-ph] (cit. on p. 52).

[116] T. C. Li, H. Kelkar, D. Medellin and M. G. Raizen,
"Real-time control of the periodicity of a standing wave: an optical accordion",
Optics Express 16.8 (2008) 5465, ISSN: 1094-4087 (cit. on p. 53).

[117] Y. Y. Schechner, R. Piestun and J. Shamir,
"Wave propagation with rotating intensity distributions", Physical Review E - Statistical Physics, Plasmas, Fluids, and Related Interdisciplinary Topics 54.1 (1996) R50, ISSN: 1063651X
(cit. on p. 54).

[118] S. R. P. Pavani, M. A. Thompson, J. S. Biteen, S. J. Lord, N. Liu, R. J. Twieg, R. Piestun and W. E. Moerner, "Three-dimensional, single-molecule fluorescence imaging beyond the diffraction limit by using a double-helix point spread function", Proceedings of the National Academy of Sciences of the United States of America 106.9 (2009) 2995, ISSN: 00278424
(cit. on pp. 54, 70, 91).

[119] M. M. Dorantes,
"Fast non-destructive internal state detection of neutral atoms in optical potentials",
Dissertation: Bonn, 2016 (cit. on pp. 55, 70).

[120] W. Zhou-hanf,
"Robust Holographic Generation of Arbitrary Light Patterns : Method and Implementation",
Master: Universität Bonn, 2018 (cit. on pp. 56, 70, 92).

[121] T. Legrand,
"Vergleich der Holografie und der direkten Abbildung mit dem räumlichen Lichtmodulator",
Bachelor: Bonn, 2019 (cit. on pp. 56, 70, 92).

[122] C. Robens, J. Zopes, W. Alt, S. Brakhane, D. Meschede and A. Alberti,
"Low-Entropy States of Neutral Atoms in Polarization-Synthesized Optical Lattices",
Physical Review Letters 118.6 (2017) 1, ISSN: 10797114, arXiv: 1608.02410
(cit. on pp. 56, 71).

[123] A. J. Leggett,
"Quantum Liquids: Bose Condensation and Cooper Pairing in Condensed-Matter Systems",
Physics Today 60.8 (2007) 57, ISSN: 0031-9228 (cit. on pp. 56, 71).

[124] T. Esslinger, "Fermi-hubbard physics with atoms in an optical lattice",
Annual Review of Condensed Matter Physics 1 (2010) 129, ISSN: 19475454 (cit. on pp. 56, 71).

[125] C. K. Zachos, D. B. Fairlie and T. L. Curtright,
Quantum Mechanics in Phase Space (Zachos, Fairlie, Cur),
World Scientific Publishing Co. Pte. Ltd., 2005, ISBN: 981 -238-384-0 (cit. on pp. 57, 58).

[126] L. G. Lutterbach and L. Davidovich, "Scheme for Direct Measurement of the Two-mode Wigner Function in Cavity QED and Ion Traps", Physical Review Letters 78.13 (1997) 2547, ISSN: 00049506 (cit. on pp. 57, 67).

[127] P. Bertet, A. Auffeves, P. Maioli, S. Osnaghi, T. Meunier, M. Brune, J. M. Raimond and S. Haroche, "Direct Measurement of the Wigner Function of a One-Photon Fock State in a Cavity", Physical Review Letters 89.20 (2002) 20, ISSN: 10797114 (cit. on pp. 57, 68).

[128] E. Wigner, "On the quantum correction for thermodynamic equilibrium", Physical Review 40.5 (1932) 749, ISSN: 0031899X (cit. on pp. 57, 58).

[129] H. J. Groenewold, "On the principles of elementary quantum mechanics", Physica 12.7 (1946) 405, ISSN: 00318914 (cit. on p. 57).

[130] J. E. Moyal, "Quantum mechanics as a statistical theory", Mathematical Proceedings of the Cambridge Philosophical Society 45.1 (1949) 99, ISSN: 14698064 (cit. on pp. 57, 58).

[131] E. C. G. Sudarshan, "Equivalence of Semiclassical and Quantum Mechanical Descriptions of Statistical Light Beams", 10.7 (1963) 277 (cit. on p. 58).

[132] K. Husimi, "Some formal properties of the density matrix", Proc. Phys. Math. Soc. Jpn. 22 (1940) 264 (cit. on p. 58).

[133] M. Gadella, "Moyal Formulation of Quantum Mechanics", Fortschritte der Physik/Progress of Physics 43.3 (1995) 229, ISSN: 15213978 (cit. on p. 58).

[134] M. Hillery, R. F. O'Connell, M. O. Scully and E. P. Wigner, "Distribution functions in physics: Fundamentals", Physics Reports 106.3 (1984) 121, ISSN: 03701573 (cit. on p. 58).

[135] J. Weinbub and D. K. Ferry, "Recent advances in Wigner function approaches", Applied Physics Reviews 5.4 (2018), ISSN: 19319401 (cit. on p. 58).

[136] W. P. Schleich, *Quantum Optics in Phase Space*, 2001, ISBN: 352729435X (cit. on p. 58).

[137] W. B. Case, "Wigner functions and Weyl transforms for pedestrians", June (2008) 937 (cit. on p. 58).

[138] D. Harland, M. J. Everitt, K. Nemoto, T. Tilma and T. P. Spiller, "Towards a complete and continuous Wigner function for an ensemble of spins or qubits", Physical Review A - Atomic, Molecular, and Optical Physics 86.6 (2012), ISSN: 10502947 (cit. on p. 58).

[139] S. Varró and J. Javanainen, "Gauge-invariant relativistic Wigner functions", Journal of Optics B: Quantum and Semiclassical Optics 5.3 (2003) 402, ISSN: 14644266 (cit. on p. 58).

[140] P. Morgan, "A relativistic variant of the Wigner function", Physics Letters, Section A: General, Atomic and Solid State Physics 321.4 (2004) 216, ISSN: 03759601, arXiv: 0304171 [quant-ph] (cit. on p. 58).

[141] N. Peter, "Optimal quantum control of atomic wave packets in optical lattices", Dissertation: Universität Bonn, 2018 (cit. on p. 58).

[142] M. Rivera-Lam, "Probing the quantum speed limit of atomic matter waves in optical lattices", Dissertation: Universität Bonn, 2021 99 (cit. on p. 58).

[143] K. E. Cahill and R. J. Glauber, "Ordered expansions in boson amplitude operators", Physical Review 177.5 (1969) 1857, ISSN: 0031899X (cit. on p. 58).

[144] K. E. Cahill and R. J. Glauber, "Density operators and quasiprobability distributions", Physical Review 177.5 (1969) 1882, ISSN: 0031899X (cit. on p. 58).

[145] A. Grossmann, "Parity operator and quantization of δ-functions", Communications in Mathematical Physics 48.3 (1976) 191, ISSN: 00103616 (cit. on p. 59).

[146] M. Karski, "State-selective transport of single neutral atoms", Dissertation: Universität Bonn, 2010 1 (cit. on p. 64).

[147] S. Deléglise, I. Dotsenko, C. Sayrin, J. Bernu, M. Brune, J. M. Raimond and S. Haroche, "Reconstruction of non-classical cavity field states with snapshots of their decoherence", Nature 455.7212 (2008) 510, ISSN: 14764687 (cit. on p. 68).

[148] A. M. Kaufman, B. J. Lester, C. M. Reynolds, M. L. Wall, M. Foss-Feig, K. R. Hazzard, A. M. Rey and C. A. Regal, "Two-particle quantum interference in tunnel-coupled optical tweezers", Science 345.6194 (2014) 306, ISSN: 10959203 (cit. on p. 71).

[149] A. Knieps, "A Spatial Light Modulator for Steering Quantum Walks with Single-Site Precision", Master: Universität Bonn, 2017 (cit. on p. 91).

[150] J. C. G. Fernández, "Strong Coupling between Small Atomic Ensembles and an Open Fiber Cavity", Dissertation: Universität Bonn, 2017 164 (cit. on p. 91).

[151] W. T. Meyer, *IEEE standard for waveform recorders*, vol. 1, 1995 357, ISBN: 1559374888 (cit. on p. 91).

[152] R. O. Schmidt, "Multiple emitter location and signal parameter estimation", IEEE Transactions on antennas and propagation 3 (1986) 190 (cit. on p. 91).

[153] M. Sajid, "Magnetic Quantum Walks of Neutral Atoms in Optical Lattices", Dissertation: Universität Bonn, 2018 (cit. on p. 92).

APPENDIX A

Computation for the Polarization Gradient

In this section I derive the equation 3.3, which gives an explicit expression for the differential light shift from the light shift.

The light shift is given by

$$\begin{pmatrix} U_\uparrow \\ U_\downarrow \end{pmatrix} = c_0 \begin{pmatrix} 1 & 0 & 1/2 \\ 1/8 & 7/8 & 1/2 \end{pmatrix} \begin{pmatrix} I_{\sigma^+} \\ I_{\sigma^-} \\ I_\pi \end{pmatrix} \quad \text{with} \quad c_0 = -k_B \times 2.717\mathrm{pK}/(W/m^2) \tag{A.1}$$

for a wavelength of 866 nm as shown in section 2.3. The differential light shift depends on the σ^+ and σ^--components

$$\Delta\nu = \frac{7}{8} c_0 (I_{\sigma^+} - I_{\sigma^-}). \tag{A.2}$$

Now we want to compute the light shift as a function of the electric field strength of the vertically and horizontally polarized beam and their relative (or differential) phase.

Z.Z.: $\Delta\nu = \frac{7}{8} c_0 c \epsilon E_V E_H \sin(\varphi)$

Dazu: Purely polarized can be described using the Jones calculus. The Jones vectors read

$$\begin{aligned} \underline{e}_V &= \begin{pmatrix} 1 \\ 0 \end{pmatrix} \qquad \underline{e}_{\sigma^+} = \tfrac{1}{\sqrt{2}} \begin{pmatrix} 1 \\ -\mathrm{i} \end{pmatrix} \\ \underline{e}_H &= \begin{pmatrix} 0 \\ 1 \end{pmatrix} \qquad \underline{e}_{\sigma^-} = \tfrac{1}{\sqrt{2}} \begin{pmatrix} 1 \\ \mathrm{i} \end{pmatrix} \end{aligned} \tag{A.3}$$

We want to compute the light shift induced by a an electric field where we superpose a vertically polarized beam $\underline{E}_V = E_V \underline{e}_V$ and a horizontally polarized beam $\underline{E}_H = \mathrm{e}^{\mathrm{i}\varphi} \mathrm{E_H} \underline{\mathrm{e}}_\mathrm{H}$.

$$\begin{aligned} \underline{E} &= \underline{E}_V + \underline{E}_H \\ &= E_V \underline{e}_V + E_H \mathrm{e}^{\mathrm{i}\varphi} \underline{e}_H \\ &= \tfrac{1}{\sqrt{2}} \left(E_V + \mathrm{i}\mathrm{e}^{\mathrm{i}\varphi} E_H \right) \underline{e}_{\sigma^+} + \tfrac{1}{\sqrt{2}} \left(E_V - \mathrm{i}\mathrm{e}^{\mathrm{i}\varphi} E_H \right) \underline{e}_{\sigma^-} \\ &= \underbrace{\frac{1}{\sqrt{2}} \left(E_V + \mathrm{e}^{\mathrm{i}(\varphi + \frac{\pi}{2})} E_H \right)}_{:= E_{\sigma^+}} \underline{e}_{\sigma^+} + \underbrace{\frac{1}{\sqrt{2}} \left(E_V - \mathrm{e}^{\mathrm{i}(\varphi + \frac{\pi}{2})} E_H \right)}_{:= E_{\sigma^-}} \underline{e}_{\sigma^-} \end{aligned} \tag{A.4}$$

With $I = \frac{1}{2}c\epsilon_0$ and the orthogonality of the σ^+ and σ^- polarizations it follows

$$\begin{aligned} I_{\sigma^+} &= \tfrac{1}{2}c\epsilon_0 \, \tfrac{1}{2}\left(E_V^2 + E_H^2 - E_V E_H \sin(\varphi)\right) \\ I_{\sigma^-} &= \tfrac{1}{2}c\epsilon_0 \, \tfrac{1}{2}\left(E_V^2 + E_H^2 + E_V E_H \sin(\varphi)\right) \end{aligned} \tag{A.5}$$

APPENDIX B

Electronics

During my time in Bonn I developed and extended several electronic circuits, which I document in the following.

B.1 Amplified difference photodiode

We have developed a fast low noise, amplified difference photodiode. I improved the original design from Muhib Omar [79] by adding the monitoring output for the first stage, improving the resistance to EMI and characterizing the input for the external reference voltage. Mr Kalb from our electronics workshop is responsible for the updated PCB layout. At the time of writing, six copies were built, all of which have consistent noise- and amplification performance.

B.2 Current Stealing Circuit

I have developed a current stealing circuit to stabilize our guiding field. It is described in section 2.2, and I will give additional details here.

The circuit acts as a second stage of stabilization. A tunable current source delivers a current that is ca. 10% larger than required. This excess is bypassed using a shunt, that is installed in parallel to the load. I chose a field-effect transistor (IRF540) as a variable resistor because the gate is galvanically insulated from the channel (between source and drain). They draw (virtually) no current from the gate once loaded, and they offer high drain-to-source breakdown voltages (IRF540 V_{DSS} =100 V). The latter is necessary when high currents are required. The MOSFET is chosen to be of N-type to ensure that the voltage between the shunt resistor and the gate does not exceed the amplifier's dynamic range. For this reason, we connect the source of the MOSFET to the ground. This is important when the voltage across the load exceeds 15 V which is the case if we were to stabilize, e.g. our gradient coils (R=1.2 Ω) at the currents needed for plane selection (I≥10 A). I have chosen a depletion-mode MOSFET that insulates for zero or negative gate bias. (Gate bias is the voltage between gate and source.) If turned off, the current stealing box becomes a low pass filter.

The set-point of the current feedback is derived from a precision voltage reference[1]. The output noise of the voltage reference is reduced using a stacked foil capacitor (EPCOS/TDK B32560J1105K000 1 µF, 100 V, 7.5 mm). The bypass-capacitance is provided using stacked foil capacitors [2]. They are not wound,

[1] Analog Devices, AD587
[2] EPCOS/TDK B32560J1225K000 1 µF, 100 V, 7.5 mm

but stacked which leads to low parasitic inductance hence large bandwidths (between 500 kHz for 33 µF and 2.2 MHz for 1 µF).

Isolation coils For Currents below 10 A coils with closed ferrite cores and commercially available [3]. They are compact (30mm*25mm*21mm) and offer impedances of hundreds of µH and self-resonance frequencies above 1 MHz. A typical application that requires currents beyond 10 A is plane selection. If we were to stabilize the quadrupole field in our setup, we would drive currents up to 30 A through an inductive load of 12 mH and a self-resonance frequency of 60 kHz [5]. Coils with iron-powder cores and rated currents up to 50 A and 50 mH are commercially available [4]. The material has a larger saturation flux but limits the bandwidth of the coils to ca. 100 kHz.
The system response is further linearized by installing a bypass-capacitor parallel to the coil. This reduces the impedance of the load attached downstream of the Kelvin probe, thereby preventing the impedance of the coils to cause a phase-delay of the current through the Kelvin probe. The bypass capacitor acts as a lead-lag filter as shown in figure 2.7(a). Resistors have to be installed to dampen resonances between the compensation coil and the bypass capacitor and between the power supply and the load.

Feedforward control We can control the setpoint of the feedback externally if the experiment has insufficient magnetic shielding or the self-heating of the circuit leads We have demonstrated that the modulation bandwidth is sufficient to suppress not only slow, quasi-static drifts but also ambient magnetic fields at the line frequency and its harmonics [58].

A unity gain, differential amplifier (AMP03) is used to provide a differential input. The voltage can be added to the internal setpoint using resistors. Both the differential input and the differential amplifier computing the error signal have a finite input- and output impedance, that we need to consider when computing the gain of the external input.

The differential amplifiers have a bandwidth of 3 MHz. The noise of the external input can be low pass filtered at the expense of modulation speed by appropriately choosing the capacitors (C16, C18 and C20). The modulation bandwidth of the feedback is limited, however, by the current bypass capacitors that are used to linearize the response of the shunt resistor. They act as a low pass filter with typical corner frequencies of a few kHz. The transfer function of the system can, however, be measured and compensated. This has been done successfully in our one-dimensional, state-dependent transport experiment by our master student Andreas Blendl [58].

[3] WE-HCF SMT-Hochstrominduktivität "74437529203221" 220 µH, f_{res} =2.8 MHz, I_{sat} =5.3 A, Material: MnZn
[4] Hammond heavy current chassis mount "195J30" 10 mH, f_{res} =2.8 MHz, I_{sat} =30 A, Material: MnZn

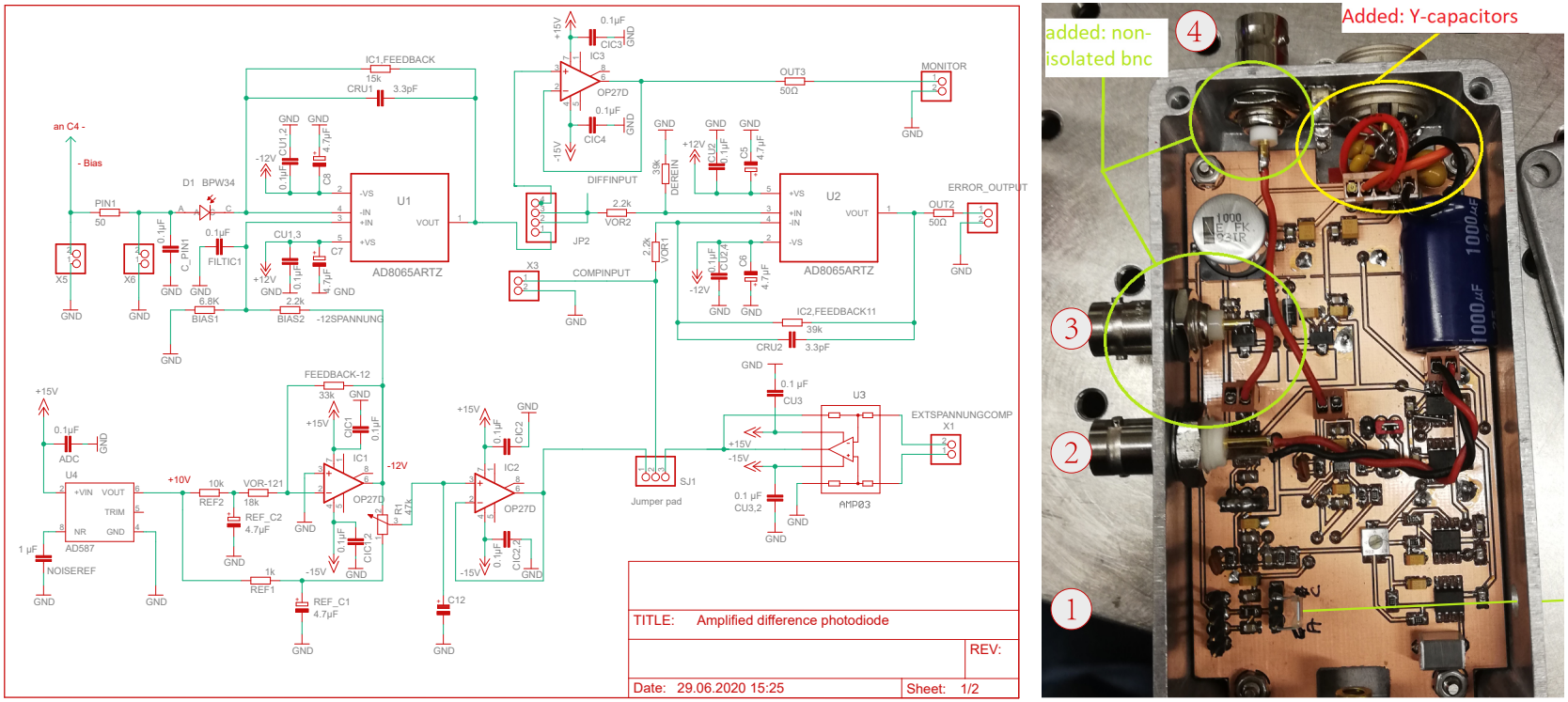

Figure B.1: Amplified difference photodiode. Left: A schematic drawing of the circuit. Right: Image of the device. (1) The photodiode (BPW34) is placed as far away from the opening as possible to allow for compact optical setups while blocking stray light. Wherever possible, SMD components are used to reduce parasitic capacitance and shrink the layout. Special low noise resistors have to be chosen (See text). (2) An external reference voltage can be connected to a unity-gain differential amplifier. Alternatively, one can use the internal reference voltage generated by a potentiometer. We can monitor the first stage (3) and the second stage (4) simultaneously. The use of non-isolating BNC connectors reduces the sensitivity to electromagnetically induces interference (EMI). The resistance against EMI is improved by placing the Y-capacitors that block electronic noise directly at the DIN-5 connector for the supply and bias voltage. The board is connected to the ground only through the standoffs.

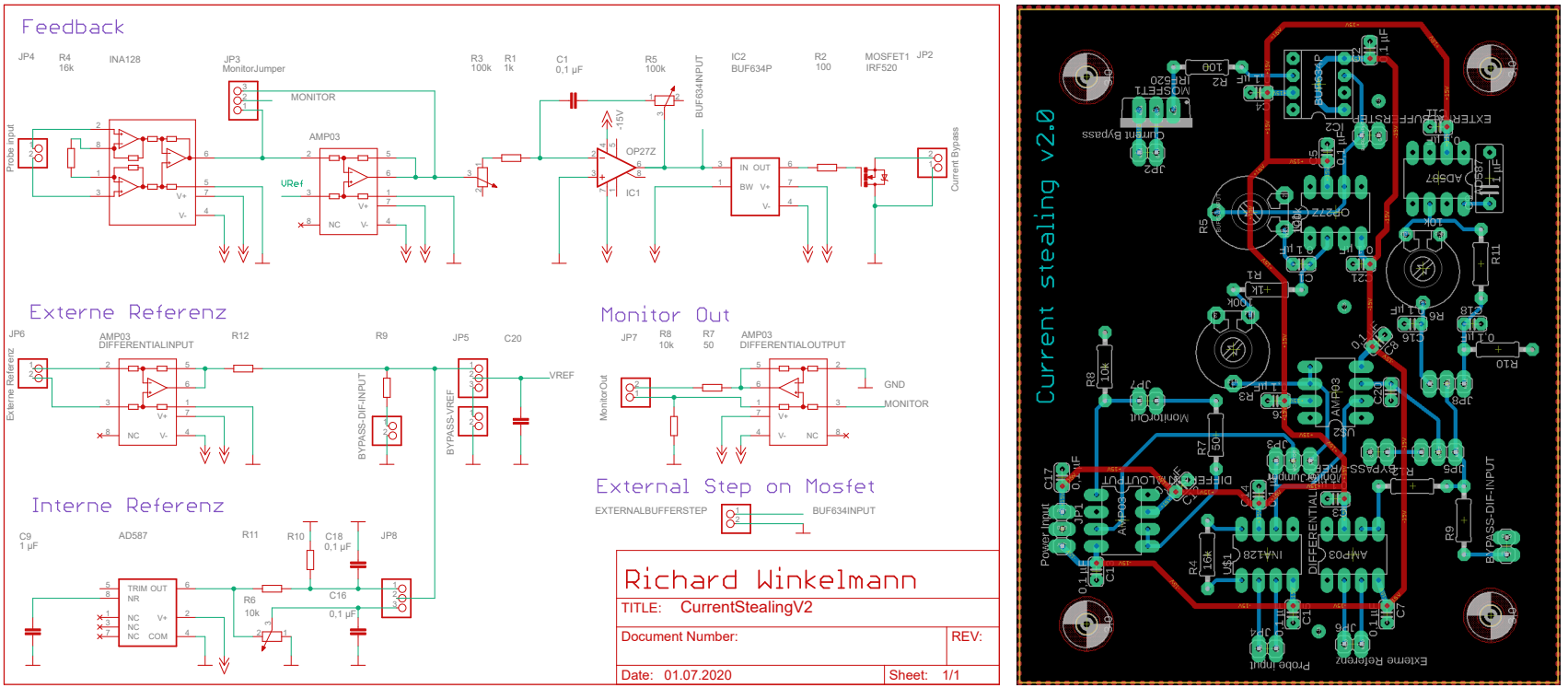

Figure B.2: Schematic drawing and board layout of current-stealing circuit. The current stealing circuit features four sections. The first comprises the feedback generated from a PI controller. A fast, low noise instrumentation amplifier (INA 128) is used to measure the voltage drop across the shunt resistor (of 0.1 Ω). A unity gain, difference amplifier is used to compute the error signal, which is fed into a PI-controller. Feedback on the current is given via an N-Type MOSFET which is driven by a buffer amplifier (BUF634). A high precision voltage reference (AD587, 10 V)is employed. We can choose between a potentiometer and fixed resistors to internally generate a setpoint. The setpoint can be modulated externally with a differential input. The external voltage is added using (passive network of) resistors (see text). We can monitor either the shunt-voltage or the error signal with a differential output.

APPENDIX C

Wavefront control at the level of $\lambda/78$

In our group we are currently implementing algorithms to engineer helicoidal point spread functions [118]. I will briefly describe my contribution to the characterization of the employed spatial light modulator (SLM) and how it could alternatively be used to implement magnetic quantum walks.

We are using a twisted-nematic phase-only spatial light modulator[1]. A custom software control the SLM with Matlab was written by Alexander Knieps who also measured its phase noise performance [149].

I have characterized the phase front distortion of our spatial light modulator using phase shift interferometry. A Michaelson interferometer is used to measure optical surfaces. One arm of the interferometer is the device under test (DUT) and the other is has mirror that can be moved using a piezo. It is called phase shift interferometry because the displacement of the mirror induces a wavelength dependent differential phase between both beams. Lenses in 4f configurations are used to sharply image the DUT onto a ccd camera. The resulting interference pattern can thus be spatially resolved and each pixel is used to record an interference fringe that follows a sinusoidal modulation

$$I_{x,y}(x) = A_{x,y} + B_{x,y}cos\left(\frac{2\pi x}{\lambda} + \varphi_{x,y}\right). \tag{C.1}$$

Phase shift interferometry is an established technique and has been used in our group before to measure the surface of fiber cavity mirrors [150]. Performing a least-square fit to extract the phase offset for each pixel is time-consuming. Additionally, least-square estimators yield biased results when optimizing sinusoidal models with four parameters.

The reconstruction of the surface was made faster and more precise by first measuring the phase shift per step that is common among all pixels. The remaining problem is linear since it can be rewritten in the form

$$I_{x,y}(x) = \tilde{A}_{x,y}\sin\left(\frac{2\pi x}{\lambda} + \varphi_{x,y}\right) + \tilde{B}_{x,y}\cos\left(\frac{2\pi x}{\lambda} + \varphi_{x,y}\right) + \tilde{C}_{x,y}. \tag{C.2}$$

Minimizing this least-square problem can be done by matrix inversion [151]. I tested several methods to estimate phase shift per step using synthetic data. I found that the best results are obtained with the multiple signal classification (MUSIC) algorithm [152]. The time required to extract the surface from one fringe was reduced from more than ten minutes to less than one second.

[1] Santec, LCoS SLM-100

This work has been continued by Weiqi Zhou-Hanf [120] who was able to compensate the wave front distortion and achieve a flatness of $\lambda/78$. Additionally, the non-linearity of the phase response of each pixel was measured and compensated by means of a lookup-table. A comparison between holography and direct imaging was performed to investigate which method would be suited best to imprint linear phase gradients onto the atom cloud [121]. We found that direct imaging techniques are both easier to implement and yield better results for the intensity patterns, that we plan to imprint onto the lattice.

In the future, we plan to use the spatial light modulator to create intensity patterns that are subsequently projected onto the lattice through the high-NA objective lens. This can be used to induce AC-Stark shifts that change the atomic resonance frequency locally. Possible applications include studying non-trivial topological phases [6] and realizing magnetic quantum walks [153].

Acknowledgements

One adventure ends, another begins. By handing in my dissertation, five exciting years in the DQSIM laboratory come to a close. During these five years, I enjoyed working with and learning from highly motivated and skilled colleagues.

First of all, I would like to thank my supervisor Prof. Dr. Dieter Meschede, for allowing me to be part of his outstanding and inspiring team. Furthermore, I thank him for the guidance and motivation he has given me throughout my PhD thesis. I also want to express my gratitude to Prof. Dr. Sebastian Hofferberth for being the second referee of my thesis. A special thank goes to Dr. Andrea Alberti, whose immense knowledge of physics and his continuous enthusiasm to discover the unknown has given me a great source of incentive and motivation. I am grateful for the opportunity to work and learn in your laboratory and I am looking forward to the one-million-step quantum simulator. My warm-hearted thank goes to Dr. Wolfgang Alt, whose vast experience, deep insight and patience were invaluable for me. He always had a solution for an uprising problem, even when it wasn't physics related. Here also a special thanks for all the delicious chocolate you have shared over the past years and for always having an open ear.

I enjoyed working with a highly motivated and gripping team that I would like to thank sincerely. I thank my colleague Gautam Ramola who started this endeavour around the same time as me and is a role model of endurance and determination. I wish you good luck in your future steps. I thank Stefan Brakhane, Geol Moon for introducing me to the DQSIM experiment, which they meticulously built. I also thank Peng Xu, who propelled our experiment further while simultaneously managing his team in Wuhan. I am still sated from the fare-well meal we enjoyed. My thanks to our master students Max Werninghaus, Peng Du, Muhib Omar, Karthik Chandrasekhara, Weiqi Zhou and Tangi Legrand for their contributions to the DQSIM experiment. I wish them all the best and success during their PhD projects.

I thank Carsten Robens for guiding me at the beginning of my PhD when everything was new. I hope you still enjoy fencing. Working in the IaP became delightful by our other group members. As one says in German: "Geteiltes Leid ist halbes Leid". Manolo, Eduardo, Sajid, Carlos, Thorsten, Jan, Tobias, Natalie, Michael, José, Miguel, Maxi, Alexander, Lukas, Pooja... Many thanks for the careful proofreading of my thesis to Eduardo, Lukas, David, Gautam, Manolo, Tangi and Hannes.

I am indebted to the non-scientific staff of the institute. I thank Tina Naggert, Fien Latumahina, Annelise Miglo and Dr. Dietmar Haubrich for smoothly handling the administrative work. Also, I would like to thank the members of our mechanical and electrical workshop. Mr Graf and Mr Langen were responsible for manufacturing various mechanical components and even water installation. I thank Mr Brähler and Mr Kalb for their advice on electrical circuits, soldering and PCB printing.

Without the continuous and unconditional support of my parents and my siblings, this PhD would have been impossible. I would like to thank Christoph Phillipi for his support. I am looking forward to seeing you as a free man. Thanks to my godmother, Prof. Dr. Irmelin Probst, for her guidance and advice. I still remember titrating and counting lever cells. Finally, I thank my fiancé Sandra, who stood by my side for the past five years while enduring the long-distance relationship and sharing with me all the highs and lows.

Declaration of Authorship

I hereby certify that the work presented here was accomplished by myself and without the use of illegitimate means of support, and that no sources and tools were used other than those cited.

Place, date	Falk-Richard Winkelmann